

MODELING AND DESIGN OF MULTI-PORT DC/DC CONVERTERS

by

ZHIJUN QIAN

B.S. Zhejiang University, 2005

M.S. Zhejiang University, 2007

A dissertation submitted in partial fulfillment of the requirements
for the degree of Doctor of Philosophy
in the Department of Electrical Engineering and Computer Science
in the College of Engineering and Computer Science
at the University of Central Florida
Orlando, Florida

Spring Term
2010

Major Professor: Issa Batarseh

© 2010 ZHIJUN QIAN

To my wife

ABSTRACT

In this dissertation, a new satellite platform power architecture based on paralleled three-port DC/DC converters is proposed to reduce the total satellite power system mass. Moreover, a four-port DC/DC converter is proposed for renewable energy applications where several renewable sources are employed. Compared to the traditional two-port converter, three-port or four-port converters are classified as multi-port converters. Multi-port converters have less component count and less conversion stage than the traditional power processing solution which adopts several independent two-port converters. Due to their advantages multi-port converters recently have attracted much attention in academia, resulting in many topologies for various applications. But all proposed topologies have at least one of the following disadvantages: 1) no bidirectional port; 2) lack of proper isolation; 3) too many active and passive components; 4) no soft-switching. In addition, most existing research focuses on the topology investigation, but lacks study on the multi-port converter's control aspects, which are actually very challenging since it is a multi-input multi-output control system and has so many cross-coupled control loops.

A three-port converter is proposed and used for space applications. The topology features bidirectional capability, low component count and soft-switching for all active switches, and has one output port to meet certain isolating requirements. For the system level control strategy, the multi-functional central controller has to achieve maximal power harvesting for the solar panel, the battery charge control for the battery, and output voltage regulation for the dc bus. In order to design these various controllers, a good dynamic model of the control object should be obtained first. Therefore, a modeling procedure based on a traditional state-space averaging method is

proposed to characterize the dynamic behavior of such a multi-port converter. The proposed modeling method is clear and easy to follow, and can be extended for other multi-port converters.

In order to boost the power level of the multi-port converter system and allow redundancy, the three-port converters are paralleled together. The current sharing control for the multi-port converters has rarely been reported. A so called “dual loop” current sharing control structure is identified to be suitable for the paralleled multi-port converters, since its current loop and the voltage loop can be considered and designed independently, which simplifies the multi-port converter’s loop analysis. The design criteria for that dual loop structure are also studied to achieve good current sharing dynamics while guaranteeing the system stability.

The renewable energy applications are continuously demanding the low cost solution, so that the renewable energy might have a more competitive dollar per kilowatt figure than the traditional fossil fuel power generation. For this reason, the multi-port converter is a good candidate for such applications due to the low component count and low cost. Especially when several renewable sources are combined to increase the power delivering certainty, the multi-port solution is more beneficial since it can replace more separate converters. A four-port converter is proposed to interface two different renewable sources, such as the wind turbine and the solar panel, one bidirectional battery device, and the galvanically isolated load. The four-port converter is based on the traditional half-bridge topology making it easy for the practicing power electronics engineer to follow the circuit design. Moreover, this topology can be extended into n input ports which allow more input renewable sources.

Finally, the work is summarized and concluded, and references are listed.

ACKNOWLEDGMENTS

I would like to express my sincere appreciation to my advisor, Professor Issa Batarseh, for his efforts to plant the seeds of this work, his constant assistance and support, and whose personality, leadership experience and critical thinking provided an exemplary example for me to follow.

I would also like to thank Dr. Oasam Abdel-Rahman for his training and advising and the members of the ApECOR team: John Elmes, Rene Kersten, Keith Mansfield and Michael Pepper, for their support. In addition, I would like to express my appreciation to my colleagues at the Power Electronics Laboratory.

Special thanks are also extended to my dissertation approval committee members, Professor Issa Batarseh, Professor John Z. Shen, Professor Wasfy Mikhael, Professor Thomas X. Wu, Professor Louis Chow and Dr. Hussam J. Al-Atrash. I am grateful to the University of Central Florida faculty and staff for their cooperation and would like to thank Ms. Theresa Collins for her invaluable editing work on my dissertation.

Finally, I would like to express my undying love and gratitude to my mother, Yu Liping, my father, Qian Huixing, and last but not least, my lovely wife, Hu Ting, and her family, whose love, encouragement and support have been the root of my success.

This work is supported partially by several agencies and companies including NASA, Advanced Power Electronics Corporation, and the University of Central Florida.

TABLE OF CONTENTS

LIST OF FIGURES	xi
LIST OF TABLES	xix
CHAPTER 1: INTRODUCTION	1
1.1. Background for Satellite Applications	1
1.2. Background for Renewable Energy Applications	7
1.3. Outline of Dissertation	11
CHAPTER 2: LITERATURE REVIEW	15
2.1. Multi-input Converters	16
2.2. Multi-port Converters	20
2.3. Summary	24
CHAPTER 3: AN INTEGRATED THREE-PORT DC/DC CONVERTER: CIRCUIT ANALYSIS, MODELING AND CONTROL	27
3.1. General Description	27
3.2. Circuit and Topology	27
3.2.1. Circuit Operation Principles	28
3.2.2. ZVS Analysis	36
3.2.3. DC Analysis	37
3.3. Modeling and Control	38
3.3.1. Mode Definition	38
3.3.2. Control Structure	41

3.3.3. Autonomous Mode Transitions	43
3.3.4. Converter Modeling and Controller Design	48
3.4. Experimental Results.....	62
CHAPTER 4: PARALLEL OPERATION OF MULTIPLE THREE-PORT	
CONVERTERS	77
4.1. General Description.....	77
4.2. Current Sharing for Two Paralleled Converters.....	77
4.2.1. Output Port Current Sharing for Two Paralleled Converters	78
4.2.2. Modeling of Dual-loop Current Sharing Structure.....	81
4.2.3. Battery Port Current Sharing for Two Paralleled Converters.....	88
4.2.4. Input Port Current Sharing for Two Paralleled Converters	94
4.3. Experiments for Two Three-port Converters	97
4.4. Multi-channel Paralleled Three-port Converters.....	103
4.4.1. Output Port Hybrid Current Sharing Method	107
4.4.2. Synchronization Among Different Channels.....	112
4.5. Experiments for Multiple Three-port Converters.....	115
CHAPTER 5: AN INTEGRATED FOUR-PORT DC/DC CONVERTER.....	
5.1. General Description.....	120
5.2. Topology	121
5.2.1. Driving Scheme	123
5.2.2. Circuit Operation Principles	125

5.2.3. Steady State Analysis	134
5.2.4. ZVS Analysis.....	134
5.2.5. Circuit Design Considerations.....	136
5.2.6. Semiconductor Stresses	137
5.2.7. Transformer Turns Ratio	138
5.3. Modeling and Control	139
5.3.1. Various Modes of Operation	139
5.3.2. Control Structure	142
5.3.3. Converter Modeling.....	143
5.3.4. Decoupling Method	146
5.4. Experimental Results.....	147
5.5. Extension into Multi-port Converter	155
CHAPTER 6: CONCLUSIONS AND FUTURE WORK.....	157
6.1. Major Contributions	157
6.2. Future Work	159
REFERENCES	161

LIST OF FIGURES

Fig. 1. 1: Typical terminal characteristics of a solar array, (a) irradiance variations, (b) temperature variations.....	4
Fig. 1. 2: Multiple converter solutions for the satellite platform power system.....	6
Fig. 1. 3: Satellite power system includes platform power system sourcing by solar panels and batteries, and user power system sinking by various types of user loads.	6
Fig. 1. 4: The wind turbine characteristics of power V_s , rotor speed.....	10
Fig. 1. 5: The wind turbine P-V characteristics.	11
Fig. 2. 1: Multi-input buck-boost converter.....	16
Fig. 2. 2: Multi-input flyback converter.....	17
Fig. 2. 3: Multi-input flyback converter with a multi-winding transformer	18
Fig. 2. 4: Two-input current-fed full-bridge dc/dc converter.....	19
Fig. 2. 5: Three-port full-bridge dc/dc converter	21
Fig. 2. 6: Three-port half-bridge dc/dc converter	22
Fig. 2. 7: Triple-half-bridge bidirectional dc/dc converter	23
Fig. 2. 8: Reduced part, triple-half-bridge bidirectional dc/dc converter	24
Fig 3. 1: Three-port modified half-bridge converter topology, which can achieve ZVS for all three main switches (S1, S2, S3) and adopt synchronous rectification for the secondary side to minimize conduction loss.....	28
Fig 3. 2: Steady state waveforms of the three-port half-bridge converter	30

Fig 3. 3: Operation stages of the three-port half-bridge converter	35
Fig 3. 4: Different operational modes in satellite's one orbit cycle. Three-port converter can achieve MPPT, battery charge control and load regulation depending on available solar power, battery state of charge and load profile. In stage I, battery acts as the exclusive source during eclipse period. In stage II&III, solar power is maximized to decrease battery state of discharge in stage II for initial insolation period and then to increase battery state of charge in stage III for increased insolation period. In stage IV, battery charge control is applied to prevent battery over-charging and extend battery service life.	41
Fig 3. 5: Three-port converter's control architecture to achieve MPPT for solar port, battery charge control for battery port and meanwhile always maintaining voltage regulation for output port. OVR is to control d_1 , and the rest of control loops (BVR, BCR and IVR) are competing the minimum value to control d_2	42
Fig 3. 6: (a) Conventional mode transition algorithm flow chart which is inclined to cause oscillation; (b) Oscillation between Mode 1 and Mode 2 because of instant switching of duty cycle value	45
Fig 3. 7: (a) the proposed minimum function competitive method to allow smooth transition of modes; (b) Mode 1 to Mode 2 transition with no oscillation; (c) Mode 2 to Mode 1 transition with no oscillation.	47
Fig 3. 8: Basic waveforms of the three-port converter. v_{pri} and i_{Lo} represent transformer primary side voltage and output inductor current, respectively.	49

Fig 3. 9: (a) Model comparison due to duty cycle step, (b) Averaged model and circuit model comparison for Battery-regulation Mode.....	54
Fig 3. 10: Small signal model of Battery-regulation Mode, control inputs and outputs are decoupled to enable separate controller design. V_{oref} and V_{bref} are the references for output voltage and battery voltage, respectively. H_{OVR} and H_{BVR} are the compensators need to be designed.	55
Fig 3. 11: Simulated bode plots for Battery-regulation Mode, (a) $V_o(s)/d_1(s)$; (b) $V_b(s)/d_2(s)$. Dashed line denotes open loop plant transfer function before applying the compensator, solid line denotes close loop transfer function after applying the compensator. BVR loop bandwidth is set to be one tenth of that of OVR.	58
Fig 3. 12: Averaged model and circuit model comparison for Battery-balanced Mode.....	60
Fig 3. 13: Small signal model of Battery-balanced Mode, control inputs and outputs are decoupled to enable separate controller design. V_{oref} and V_{inref} are the references for output voltage and input voltage, respectively. H_{OVR} and H_{IVR} are the compensators need to be designed.	60
Fig 3. 14: Simulated bode plots of $V_{in}(s)/d_2(s)$. Dashed line denotes open loop plant transfer function before applying the compensator, solid line denotes close loop transfer function after applying the compensator.	62
Fig 3. 15: Prototype photo of three-port converter which consists of one controller board and one power board.	63
Fig 3. 16: Loading output port when the battery current is zero.....	64
Fig 3. 17: Loading battery port when the output current is zero.....	64

Fig 3. 18: ZVS for S1	65
Fig 3. 19: ZVS for S2.....	65
Fig 3. 20: ZVS for S3.....	66
Fig 3. 21: The efficiency when the power is transferred from solar port to output port.....	67
Fig 3. 22: The efficiency when the power is transferred from solar port to battery port.....	67
Fig 3. 23: The efficiency when the power is transferred from battery port to output port	68
Fig 3. 24: Autonomous mode transition, (a) Mode 1 to Mode 2; (b) Mode 2 to Mode 1	70
Fig 3. 25: Simulated and measured bode plots, (a) V_o / d_1 , (b) V_b / d_2 , (c) V_{in} / d_2	72
Fig 3. 26: (a) Battery-regulation Mode load step response, (b) Battery-balanced Mode load step response.	74
Fig 3. 27: Different mode operations based on available solar power, battery state of charge and load profile, left column shows four stages in satellite's one orbit cycle; for the right column, top one shows input solar panel voltage and current, middle one represents battery voltage and current, bottom one shows output port load level while its voltage is maintaining regulated all the time.	76
Fig.4. 1: Paralleled three-port converter system interfacing solar panel, battery pack and bus.	78
Fig.4. 2: Dual loop CS control structure	79
Fig.4. 3: Outer voltage loop and inner CS loop control structure.....	80
Fig.4. 4: Inner voltage loop and outer CS loop control structure	80

Fig.4. 5: Loop analysis of output port with two paralleled converters, G_{id} and G_{vd} are already obtained from section II (battery port control loop diagram is similar with output port).....	84
Fig.4. 6: Calculated bode plots of output port control loops	85
Fig.4. 7: Bode plots of CS loop gain T_{cs} , stable and unstable	86
Fig.4. 8: Transient response to load steps from 40% to 100%, (a) stable CS loop gain T_{cs} ; (b) unstable CS loop gain T_{cs}'	87
Fig.4. 9: Battery two stage charging profile	89
Fig.4. 10: Solar array irradiance changes, then battery charging power changes accordingly	89
Fig.4. 11: Load level changes, then battery charging power changes accordingly	90
Fig.4. 12: Battery output model with droop resistances	91
Fig.4. 13: Effect of different droop rate on CS error (a) undesirable (b) acceptable (c) good, zero error at 50% (d) good, zero error at 100%	93
Fig.4. 14: Battery charging algorithm with CS.....	94
Fig.4. 15: Input port current sharing diagram.....	95
Fig.4. 16: Perturb&Observe MPPT algorithm with CS.....	96
Fig.4. 17: Prototype photo of two paralleled converters sharing with one DSP controller board, each power stage is rated at 200W, input port and battery port has the same ground while output port is isolated.	97
Fig.4. 18: Test setup with two paralleled three-port converters	98
Fig.4. 19: Steady state waveforms for output inductor current and switching node voltage.....	99

Fig.4. 20: Current sharing performance before and after CS function enabled.....	99
Fig.4. 21: Current sharing performance before and after CS function enabled.....	100
Fig.4. 22: Output port load sweep (0.5-14A).....	100
Fig.4. 23: Battery port load sweep (0.5-11A).....	101
Fig.4. 24: Battery load transient (1-5.5A).....	101
Fig.4. 25: Measured bode plots of output port (T_v and T_{sys} agree with each other)	102
Fig.4. 26: Measured bode plots of battery port, droop CS does not affect BVR loop.....	103
Fig.4. 27: Multi-channel converter structure	104
Fig.4. 28: CS results with different approaches: (a) no current sharing, (b) active current sharing, (c) droop current sharing.	106
Fig.4. 29: Output port hybrid CS structure	107
Fig.4. 30: Thevenin equivalent circuit	107
Fig.4. 31: Output impedance with (a) hybrid CS and (b) droop CS method.	110
Fig.4. 32: CS simulation results; (a) hybrid CS method, (b) droop CS method.	111
Fig.4. 33: Implementation of synchronization with no wires: (a) circuit block diagram; (b) waveforms	113
Fig.4. 34: Signal synchronization, (a) without synchronization; (b) with synchronization.....	114
Fig.4. 35: Prototype photo of two converter channels	115
Fig.4. 36: Output port CS performance: (a) droop CS; (b) hybrid CS with better transients.	116
Fig.4. 37: One channel fails while the other channel is not affected.	117
Fig.4. 38: Input Port CS with MPPT	118

Fig.4. 39: Autonomous mode transitions: (a) both with MPPT; (b) transit from both with MPPT to one with MPPT ; (c) transit from one with MPPT to both without MPPT.	119
Fig. 5. 1: Four-port converter concept	121
Fig. 5. 2: The four-port half-bridge converter topology, which can achieve ZVS for all four main switches (S1, S2, S3 and S4) and adopts synchronous rectification for the secondary side to minimize conduction loss.	122
Fig. 5. 3: The proposed modulation scheme: (a) PWM modulation circuits; (b) driving signal key waveforms.....	124
Fig. 5. 4: Steady state waveforms of the four-port half-bridge converter.....	127
Fig. 5. 5: Operation stages of the four-port half-bridge converter.....	133
Fig. 5. 6: A possible control structure to achieve MPPT for the PV panel and the wind turbine, meanwhile maintaining output voltage regulation. OVR, SVR and WVR loops are to control d_1 , d_2 and d_3 , respectively.	142
Fig. 5. 7: Small signal model diagram, control inputs and outputs are decoupled to enable separate controller design. The far right signals are routed to the far left ones in this diagram. V_{sref} , V_{wref} and V_{oref} are the references for solar, wind and output voltages, respectively. H_{SVR} , H_{WVR} and H_{OVR} are the compensators need to be designed.	145
Fig. 5. 8: Steady state waveforms: (a) Loading the output port when the battery current is zero; (b) Loading the battery port when the output current is zero.....	149

Fig. 5. 9: V_{gs} and V_{sw} of the switch S1	150
Fig. 5. 10: V_{gs} and V_{sw} of the switch S2	150
Fig. 5. 11: Solar port, wind port, output port voltages under different load/source conditions.	152
Fig. 5. 12: Efficiency under different load/source conditions	152
Fig. 5. 13: Transient response of solar, wind and output voltages when the load is perturbed by a step change between 10% and 90% rated output current.....	154
Fig. 5. 14: OVR loop bode plots: (a) prediction; (b) experiment.	154
Fig. 5. 15: SVR loop bode plots: (a) prediction; (b) experiment.	155
Fig. 5. 16: WVR loop bode plots: (a) prediction; (b) experiment.....	155
Fig. 5. 17: Extension of the proposed multi-port DC/DC converter.....	156

LIST OF TABLES

Table 2.1 Comparison of Conventional Structure and Integrated Structure.....	15
Table 3.1 Values of Circuit Parameters	63
Table 5.1 Operational Stages of the Four-port Converter.....	140
Table 5.2 Different Load/Source Current Level Conditions	151

CHAPTER 1: INTRODUCTION

This chapter introduces the background information for the proposed multi-port converter to be used in satellite applications and renewable energy applications.

1.1. Background for Satellite Applications

The ever-increasing cost of launching a spacecraft into space, approximately \$100,000/kg, is a major driving force behind the efforts to minimize the volume and weight of its power system. Take the international space station as an example, the cost of the solar arrays per kilowatt is over \$3M/kW, assuming a mass of the solar array wing of 1000 kg and a beginning-of-life power of 32 kW[3]. In other words, the cost is heavily determined by the mass. Moreover, it is generally accepted that the satellite platform power system constitutes about 25% of its total dry mass, and reaches a figure of 35% when the user power system is included[1]. Therefore, mass is one of the most important design constraints for the space power system.

The satellite platform power system consists of solar arrays, batteries and an interface power conditioning unit (PCU). The PCU then connects the solar arrays and batteries to a distribution bus, normally 28V in low earth orbital (LEO) applications. The distribution bus then delivers the power to the user power system which includes various user loads such as propulsion, altitude control and data handling, etc.

The solar arrays generate the electrical power during periods of solar insolation throughout the operational life of the satellite, and deliver the sufficient power to supply normal satellite bus, which payloads the power demands. As mentioned above, the solar array is extremely heavy and expensive; therefore, one major issue is to efficiently convert this solar energy into a type of electrical energy that can be used by various loads.

Normally, there are two steps in the solar energy conversion.

The first step is to convert solar energy into an uncontrolled electrical power; its efficiency and mass is strongly dependent on the solar array materials and the efficiency improvement is relying on the development of material engineering, therefore it is beyond the scope of the power electronics research.

The second step is to use a power electronics circuit or interface to convert the uncontrolled power into a controlled and usable electrical power which can drive a distribution bus. The second conversion step relies on power electronics engineers to come up with smart solutions to achieve the power management control, with low mass and high efficiency.

The terminal voltage-current relationship of a PV cell can be described by the following equation.

$$I = I_{photo} - I_o \cdot (\exp[q / A \cdot K \cdot T \cdot (V + I \cdot R_{series})] - 1) - V / R_{shunt} \quad Eq. 1.1$$

Where I_{photo} : the photo current generated due to insolation

I_o : the reverse saturation current of semiconductor material

R_{series} : the series ohmic resistance of the cell

R_{shunt} : the leakage current

K : the boltzman's constant

T : the absolute operating temperature

q : the charge of a single electron

A : the ideality factor of the p-n junction.

Figure 1.1 shows the typical nonlinear terminal characteristics of a solar array at different operating conditions. For certain irradiance levels and temperatures, each PV curve has a point that can deliver the maximal power. This point is defined as the maximum power point. However, this point continuously moves following the variations in irradiance, temperature, and other operating conditions. Therefore, a power electronics interface needs to be installed to change the PV's load characteristics and to force the PV panel to follow this point which can maximize the solar power harvesting.

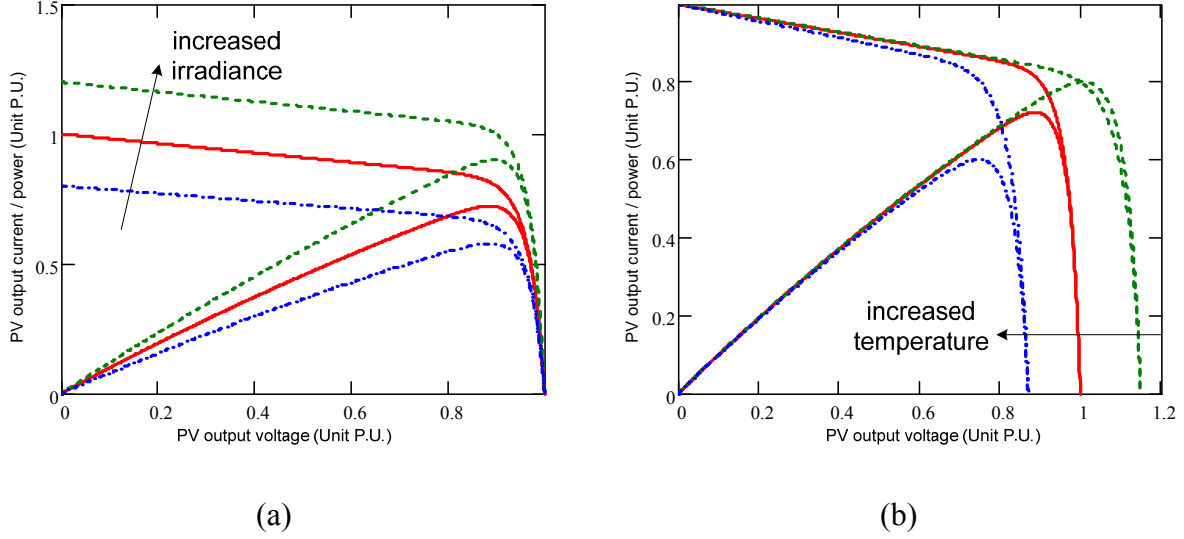


Fig. 1. 1: Typical terminal characteristics of a solar array, (a) irradiance variations, (b) temperature variations.

Considering the satellite PCU, for the PV arrays, Maximum Power Point Tracking (MPPT) is very desirable in missions where the sun intensity varies drastically. Since for a given power budget requirement, MPPT will allow a smaller solar array to manage the same amount of load, therefore has the potential to lower overall mass of the power system. Another thing is that rather than an unregulated bus, a regulated bus will permit more efficient design of payload converters with less mass and volume by its impact on the filtering and derating of power components, thus may also save overall mass. Therefore, MPPT and bus regulation can potentially reduce the total satellite power system mass.

On the other hand, the battery will provide electrical energy to the satellite during pre-launch operations, the launch phase, eclipse periods, and during periods of peak power demand that exceeds solar array output capability. The battery needs to be protected from both over-charging and over-discharging in order to extend its service lifespan. So battery protection is always necessary for the satellite power system.

However, in the traditional satellite power system architectures as shown in Figure 1.2, normally several independent converters are used to achieve MPPT for the solar panel, battery charging/discharging control and bus regulation at the expense of increased conversion steps and control complexity. The added complexity, together with increased losses, size, weight, and cost, as well as decreased reliability, has impeded wide-spread adoption of such architectures for the satellite PCU. The potentially profitable MPPT technology has often been difficult to justify given the mass of MPPT regulator and control complexity overhead. Therefore, as in Figure 1.3, a single conversion stage is proposed in this dissertation to efficiently achieve MPPT and battery regulation while always maintaining a regulated distribution bus. The multi-functional utilization of power processing components and integration of control tasks reduces the size, weight, cost, and complexity, making the three-port converter a good candidate for the satellite platform power system.

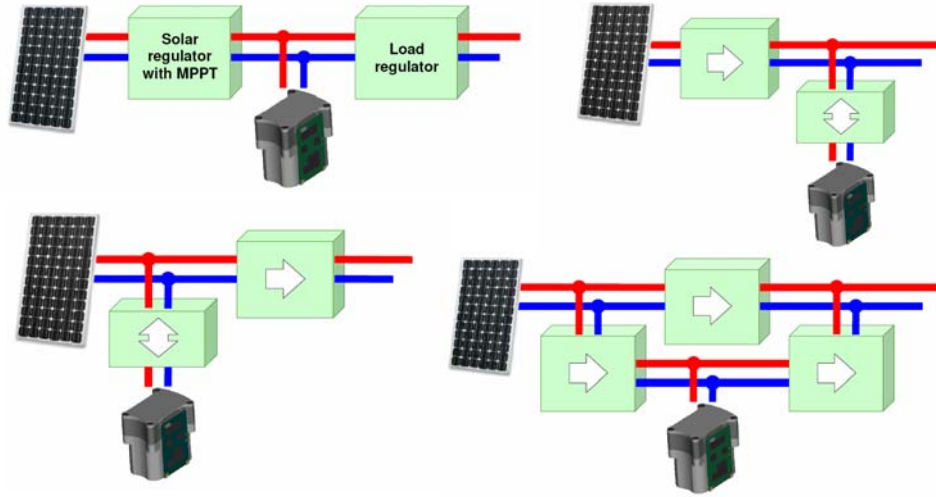


Fig. 1. 2: Multiple converter solutions for the satellite platform power system.

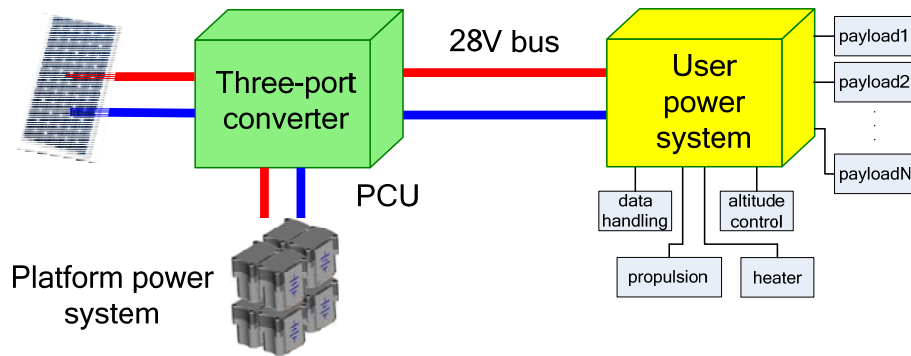


Fig. 1. 3: Satellite power system includes platform power system sourcing by solar panels and batteries, and user power system sinking by various types of user loads.

1.2. Background for Renewable Energy Applications

Recently, renewable energy sources such as PV arrays, wind generators and fuel cells are gaining more and more attention due to their advantage of being abundant in nature and causing zero-emissions. For solar energy and wind energy, they are now the world's fastest growing energy resources. Today's PV arrays and wind turbines are state-of-the-art of modern technology, with modular design and quick installation. Since these renewable sources are intermittent in nature, combining more than one renewable source can increase the certainty of continuous load supplying compared with the individual source because of the renewable sources' complementary feature.

In order to accommodate different types of renewable sources, a multi-port converter interface will be desirable to achieve the power management control among different power sources and loads, and a storage device is necessary when the ac mains is not available. Otherwise, using several independent traditional converters will increase the total cost for the renewable system, because of high component count and increased control complexity. Therefore, the multi-port converter is a great fit for applications with hybrid renewable sources requiring low cost solutions.

For example, PV and wind power are complementary since sunny days are usually calm, and strong winds often occur on cloudy days or at night time. Moreover, the optimum combinations of PV array size and wind turbine capacity can be selected based on the solar and wind profile of the installation site to achieve the lowest cost per kilowatt of power. In order to keep supplying

power to the load in case no solar or wind power is available, a storage device has to be installed, which necessitates at least one bidirectional port from a multi-port interface. For the system level control strategy, in its normal operation, MPPT of both solar and wind will be desired while maintaining a regulated output, since MPPT can ensure maximum power harvesting. In addition, a battery will collect surplus power at light loading, and supply the deficit power at heavy loading. Therefore, the solar and wind sources can be scaled to deliver the average load while the battery supplies power during peak load period. As a result, PV array and wind turbine requirement is low and the initial installing cost is reduced as well.

The PV array characteristics have been introduced in the above section; in this section we will discuss the wind energy characteristics. A wind turbine can be defined as a machine that takes kinetic energy from the wind and converts it to mechanical energy and transfers the motion to an electric generator shaft. The fundamental equation governing the mechanical power capture of the wind turbine rotor blades, which drives the electrical generator, is given by:

$$P = \frac{1}{2} \rho A C_p V^3 \quad \text{Eq. 1.2}$$

Where ρ : Air density (kg/m³)

A: Area swept by the rotor blades

V: Velocity of air (m/sec)

C_p .: Power coefficient of the wind turbine.

The theoretical maximum value of the power coefficient C_p is 0.59 and it is often expressed as the function of the rotor tip-speed to wind-speed ratio TSR. TSR is defined as the linear speed of the rotor to the wind speed.

$$TSR = \frac{\omega R}{V} \quad \text{Eq. 1.3}$$

Where R and ω are the turbine radius and the angular speed, respectively. In practical designs, the maximum achievable wind turbine efficiency C_p ranges between 0.4 and 0.5 for modern high speed turbines and between 0.2 and 0.4 for slow speed turbines.

The typical power V_s . rotor speed curve is plotted in Fig 1.4. As can be seen, there is a maximum power point at a certain rotor speed. For the wind turbine, the maximum power for different wind speeds is generated at different rotor speeds. Therefore, the turbine speed should be controlled to follow an optimal operating point which is different for every wind speed. For some designs, this is achieved by incorporating a speed control in the system design to run the rotor at high speed in high wind and at low speed in low wind, resulting in maximum electrical energy generation. Unfortunately, accurate wind speed measurement in the rotor of the turbine is difficult and requires the use of a relatively expensive anemometer if it is to be used for system control.

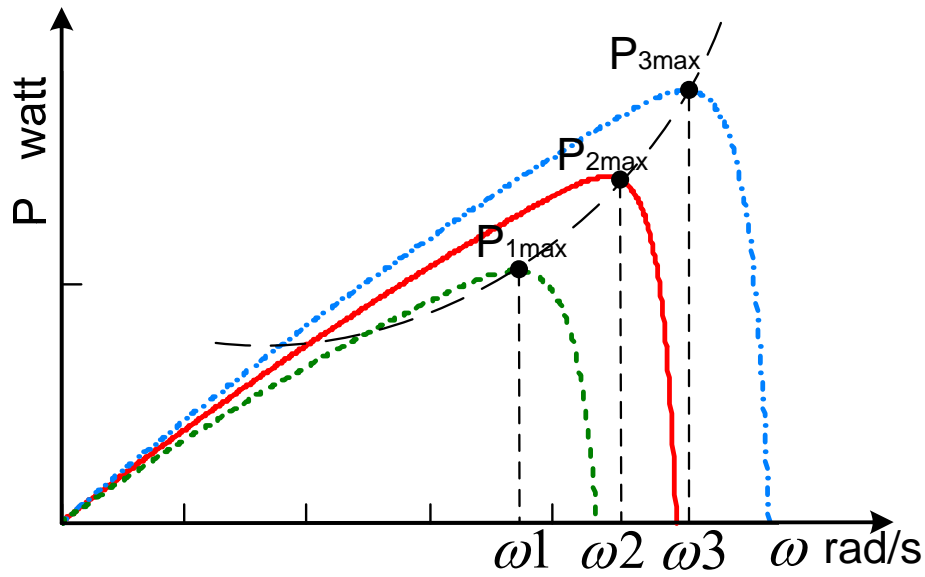


Fig. 1. 4: The wind turbine characteristics of power V_s , rotor speed.

Alternatively, a MPPT algorithm that does not need any external information like wind speed measurement can be utilized. As in Figure 1.5, almost every low to medium power wind turbine is designed to supply a three-phase AC where the frequency and magnitude varies with the speed of the wind. Additionally, a rectifier stage is often incorporated inside the wind turbine to condition the AC power into DC power. For the rectified voltage V_w and current I_w , the wind P-V curve resembles that of the solar power, in which one maximum power point exists to extract the peak power from the wind turbine. Adjusting the voltage on the dc rectifier will change the generator terminal voltage and thereby provide control over the current flowing out of the generator. Since the current is proportional to torque, the dc to dc converter will provide control over the speed of the turbine indirectly. As a result, MPPT of the wind turbine can be achieved with the similar control strategy for the PV panel.

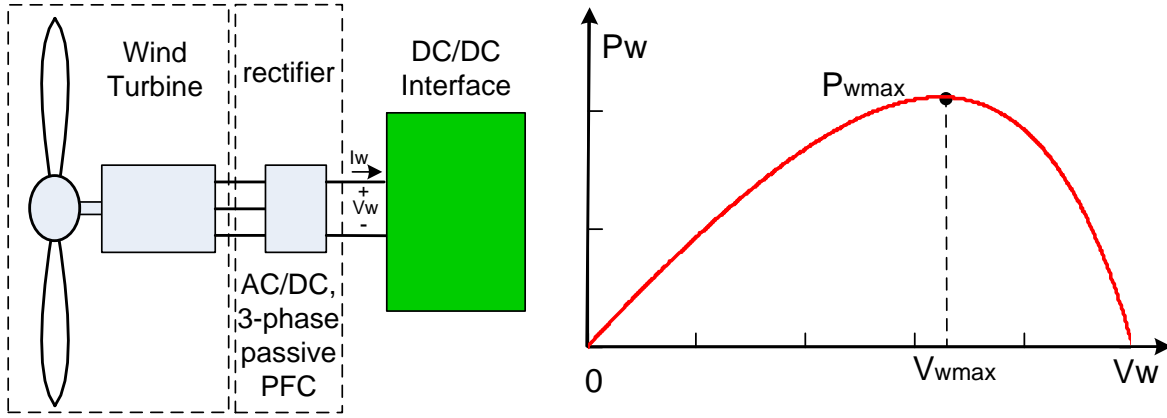


Fig. 1. 5: The wind turbine P-V characteristics.

1.3. Outline of Dissertation

The outline of this dissertation will be as follows.

The first chapter introduces the background information of the multi-port converter to be used in applications like the satellite platform power system and the hybrid renewable energy power sources. For space applications, the most important design criteria is “minimum mass”, and the multi-port converter can reduce the mass and increase the efficiency for its power system, since it has less component count and less conversion stage than traditional architectures with several independent converters. For renewable energy applications, the cost of the power electronics interface should be as low as possible. The low component count feature of the multi-port converter makes it the low cost choice for renewable energy applications.

The second chapter reviews the existing research for the multi-port converter, including both multi-input topologies and multi-port topologies. To date, most of the work is done in the power

stage design and topology investigation, with only a few reports focusing on the control aspects such as modeling and control strategies for the multi-port converter, which is actually very challenging for such kinds of multi-input multi-output systems. This dissertation is going to focus on not only the topology investigation, but also the control aspects.

The third chapter discusses the design of a three-port converter for space applications. First, the circuit operation and power stage design considerations are introduced, including the various circuit stages, ZVS analysis and DC analysis, etc. Then, the control aspects, such as various modes of operation and the autonomous mode transitions are discussed. This chapter also proposes a modeling procedure suitable for the multi-port converter based on the traditional state-space averaging method advocated by Dr. Middlebrook and Dr. Cuk [4], [5]. The major difference is that for the proposed method, different modes need to be identified first for the multi-port converter, and then the corresponding state variables need to be chosen to reveal the dynamic characteristics of the power ports that are of interest. Finally, the state-space equations in each main circuit stages are averaged to derive the converter model which follows the traditional state-space averaging method. Since control loops are coupled with each other due to the power stage integration issue, the proper decoupling method is suggested to allow separate controller design for each power port. The modeling procedure is general and is designed to be suitable for other multi-port topologies.

The fourth chapter talks about the interesting topic of paralleled multi-port converters. The main difficulty for designing current sharing controllers for multi-port converters is that there are so

many control loops involved, and the adding of the current sharing controller should not adversely affect the system stability and needs to achieve good current sharing performance, both in steady state and dynamics. Also, the added current sharing function should still preserve the attractive features like MPPT and battery charging. First, the current sharing for two three-port converters are introduced, and then followed by the current sharing for multiple three-port converter channels. A dual loop current sharing control structure is identified to be suitable for such a multi-input multi-output system, because the voltage loop and current loop can be assumed to be decoupled to simplify the control loop design. A hybrid current sharing strategy combining the active and passive control methods is proposed to achieve good current sharing dynamic performance and avoid the current sharing bus that would be present for the active current sharing method.

The fifth chapter proposes a novel four-port half-bridge converter for renewable energy applications. The four-port topology is constructed by simply adding two switches and diodes to the traditional half-bridge topology. Moreover, zero-voltage switching (ZVS) can be achieved for all main switches to allow higher efficiency at higher switching frequency, which will lead to more compact design of this multi-port converter. The circuit operation and topology is introduced first, including the driving scheme, ZVS analysis, steady state analysis, semiconductor stress consideration, etc. Three of the four ports can be tightly regulated by adjusting their independent duty cycle values, while the forth port is left unregulated to maintain the power balance for the system. The control structure targeting the hybrid solar wind application is proposed to allow MPPT of both the PV panel and the wind turbine simultaneously

or individually and then its small-signal model is derived by the modeling procedure proposed in the third chapter. Finally, a prototype is built to verify the proposed topology and confirm its ability to achieve tight independent control over three power processing paths.

The sixth chapter gives the conclusion and the scope of future work.

CHAPTER 2: LITERATURE REVIEW

Advantages of the integrated multi-port converter instead of several independent converters such as less component count and conversion stage can be obtained because resources of switching devices and storage elements are shared in each switching period. As a result, the integrated system will have a lower overall mass and more compact packaging. In addition, some other advantages of integrated power converters are lower cost, improved reliability, and enhanced dynamic performance due to power stage integration and centralized control. Additionally, it requires no communication capabilities that would be necessary for multiple converters. Therefore, the communication delay and error can be avoided with the centralized control structure. Instead of one control input for traditional two-port converter, N-port converter has N-1 control inputs, which makes the multi-port converter difficult to be modeled. Moreover, since the multi-port converter has an integrated power stage and thus the Multi-Input Multi-Output (MIMO) feature, it necessitates proper decoupling for various control loops design. Table 1 gives a comparison of the two different system structures.

Table 2.1 Comparison of Conventional Structure and Integrated Structure

	Conventional multi-converter structure	Integrated multi-port structure
Conversion stage	more than one	One
Component count	high	Low
Overall mass	high	Low
Control design	conventional and well-known	complicated and little-reported
Control structure	separated (require communication)	centralized (no communication)
Control input	one	N-1
Control loop decoupling	not required	Necessary

* N denotes the port numbers of N-port integrated converter.

Since most of the existing researches are conducted in the area of the topology investigation, the following literature review will focus on the features of different topologies.

2.1. Multi-input Converters

As shown in Figure 2.1, a multi-input integrated buck-boost topology is proposed in [10] to allow multiple input sources. The topology is capable of interfacing sources of different voltage-current characteristics to a common load, while achieving a low component count. The open-loop circuit operation has been investigated to prove that the output port can be regulated based on the duty cycle value control of the active unidirectional switches. The operation modes of both continuous conduction mode (CCM) and discontinuous conduction mode (DCM) have been analyzed to obtain voltage gain relations. However, the output voltage is reversed with regard to input, and it is a non-isolated topology, which can not meet the isolation requirement for certain critical applications.

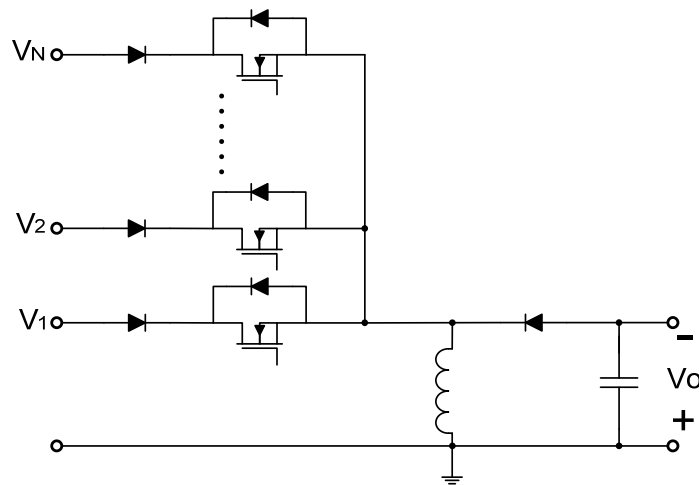


Fig. 2. 1: Multi-input buck-boost converter

Hence, an isolated version of the above-mentioned topology named as multi-input flyback converter has been proposed in [11], which is illustrated in Figure 2.2. The output voltage polarity is the same as input, and output isolation is achieved. It is shown mathematically that the idealized converter can accommodate arbitrary power commands for each input source while maintaining a prescribed output voltage. Power budgeting is demonstrated experimentally for a real converter under various circumstances, including a two-input (solar and line-powered) system. A closed-loop control example involving simultaneous tracking of output voltage and set-point tracking of the solar array shows that an autonomous system is realizable.

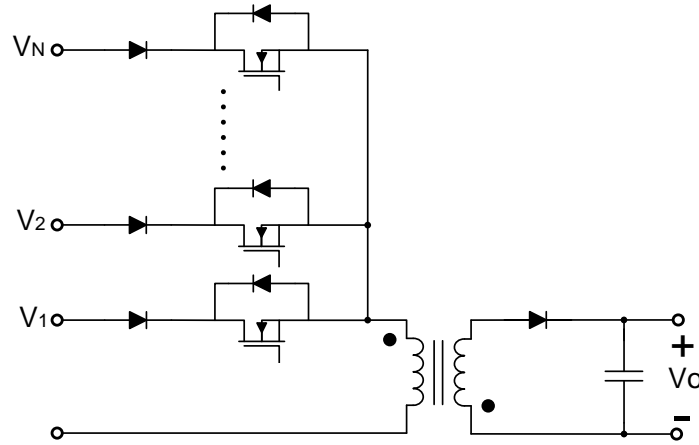


Fig. 2. 2: Multi-input flyback converter

This simple winded transformer in [11] can be replaced by a multi-winding transformer in [20] to allow more flexible input voltage range. This topology as shown in Figure 2.3 is used for a zero-emission electric power generation system that has two input sources: one solar source and one ac mains input. The steady state and dynamic characteristics of this converter has been

investigated. The boundaries of stability are clarified based on the dynamic characteristics. It is proved that if circuit parameters are designed adequately, the proposed converter is sufficiently stable and useful.

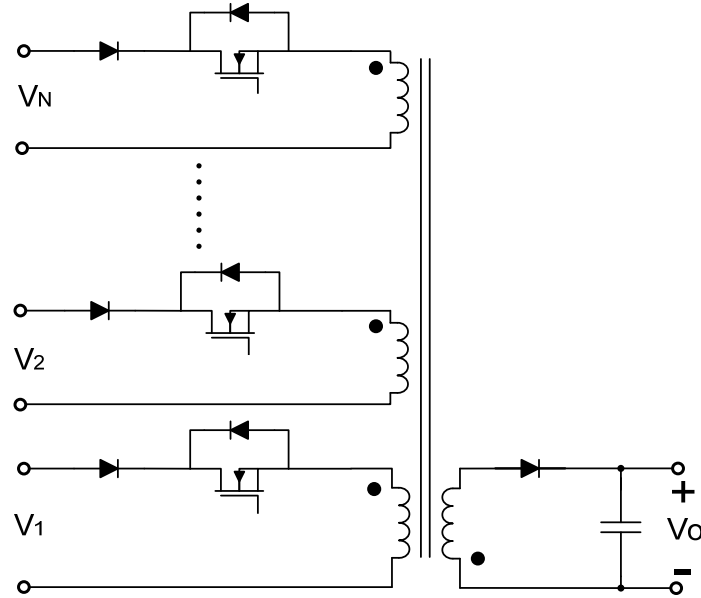


Fig. 2. 3: Multi-input flyback converter with a multi-winding transformer

As in Figure 2.4, a multi-input dc/dc converter based on the flux additivity by using a multi-winding transformer is proposed in [18]. With the phase-shifted pulse width modulation (PWM) control, this converter can draw power from two different dc sources and deliver it to the load individually or simultaneously. The major drawback of this configuration is that it uses too many active switches and the associated driving circuitry, which may not justify the advantage of low component count and compact structure for the integrated converter.

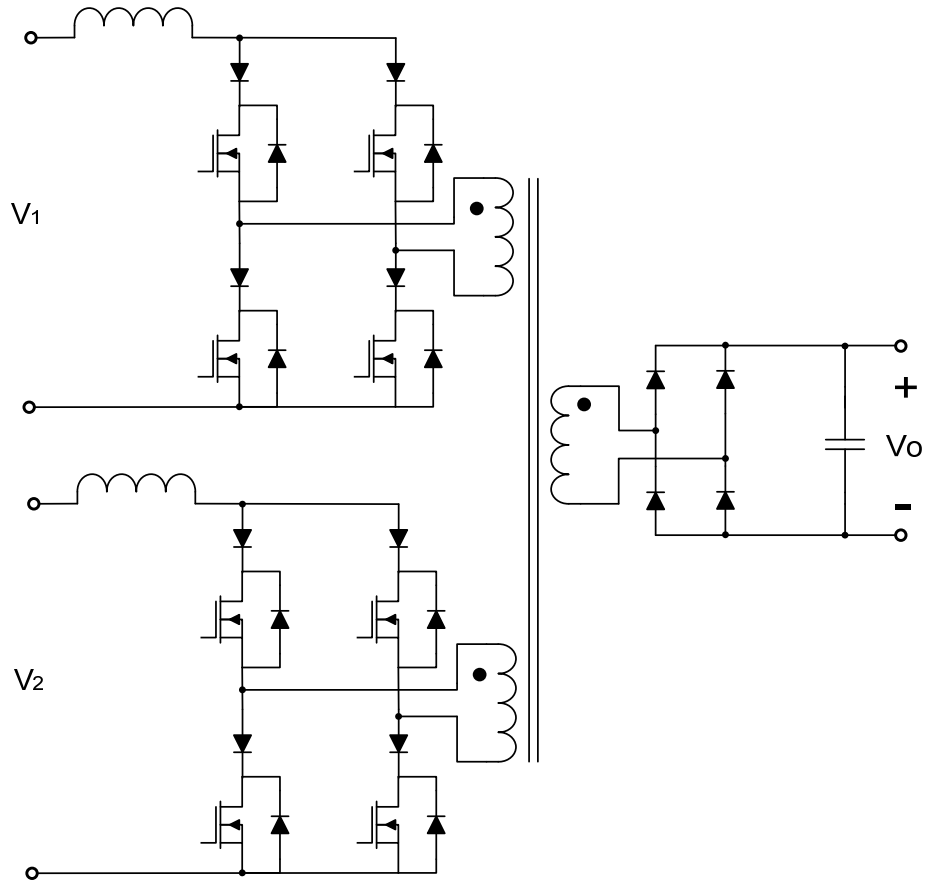


Fig. 2. 4: Two-input current-fed full-bridge dc/dc converter

In summary, the main switches in these multi-input converters mentioned above can not achieve zero voltage switching (ZVS), which may impede their applications for high switching frequency designs to further shrink the converter size and weight. But most importantly, for the power harvesting applications, when the ac mains is not available, a battery has to be installed to provide the deficit power when the renewable sources can not generate enough power. In order to interface the battery, at least one bidirectional port is required from the multi-port interface. All above-mentioned multi-input converters can not achieve this goal within one topology.

Therefore, multi-port converters having the bidirectional port are necessary to interface the storage device.

2.2. Multi-port Converters

As shown in Figure 2.5, a three-port dc-dc converter has been proposed in [25] to have bidirectional and also ZVS capabilities. It is based on full bridge cells that allow bidirectional power flow in each port. Such a configuration facilitates the matching of different voltage levels in the overall system by the multi-winding transformer. The transformer design was optimally performed in order to incorporate the leakage inductances as required by the topology to affect the phase shift control. Furthermore, for the three-port converter, a dual-PI-loop based control strategy is proposed to achieve constant output voltage and power flow management. This topology has been verified through a hybrid fuel cell and super-capacitor system to improve the slow transient response of a fuel cell stack.

A similar work has been done in [24] taking the same topology to interface 14V and 42V bus to the high voltage bus for hybrid electric vehicles (HEVs). Besides the phase shift control managing the power flow between the ports, utilization of the duty cycle control for optimizing the system behavior is discussed. The dynamic analysis and associated control design are presented. A control-oriented converter model is developed and the bode plots of the control-output transfer functions are given. A control strategy with the decoupled power flow management is implemented to obtain fast dynamic response.

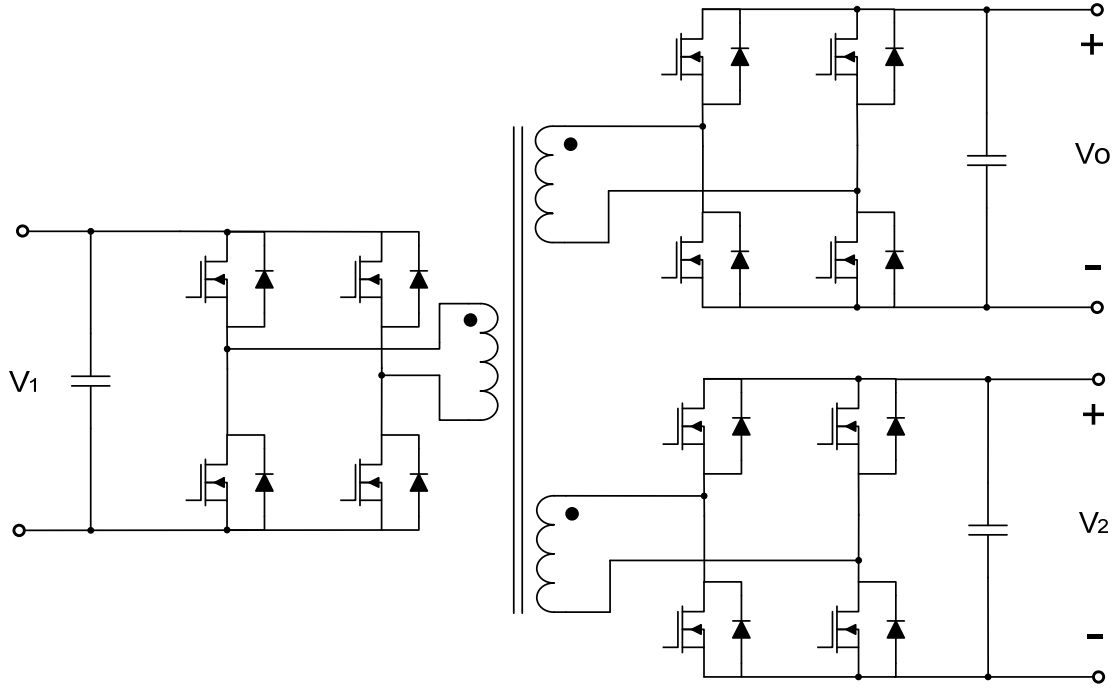


Fig. 2. 5: Three-port full-bridge dc/dc converter

As shown in Figure 2.6, a half-bridge version of this multi-port converter has been proposed in [17] for a fuel cell and super-capacitor generation system. The topology comprises a high-frequency three-winding transformer and three half-bridge cells, one of which is a boost half-bridge. The converter is controlled by phase shift, which achieves the primary power flow control, in combination with pulse width modulation (PWM). With the PWM control it is possible to reduce the rms loss and to extend the zero-voltage switching operating range to the entire phase shift region. A control scheme based on multiple PI regulators manages the power flow, regulates the output, and adjusts the duty cycle in response to the varying voltage on the port. Compared with full-bridge based topology, it applies half input voltage to the transformer

and adopts fewer switches to process the power. Therefore, the half-bridge based multi-port topology is more suitable for low to medium power applications.

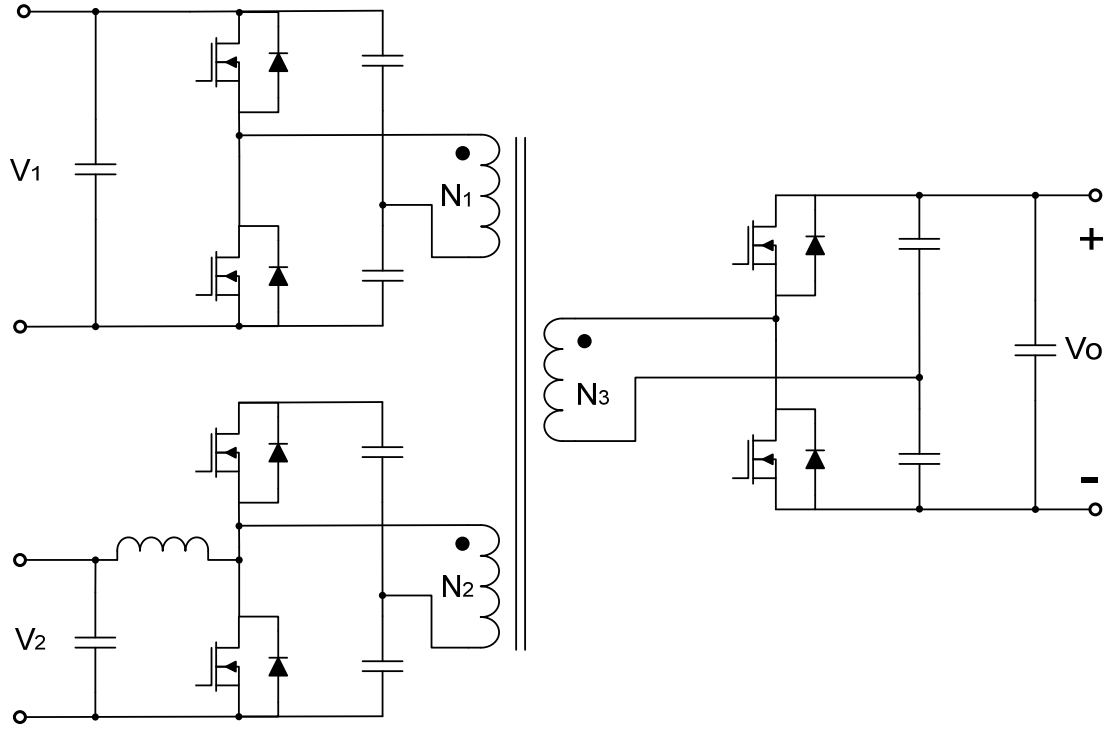


Fig. 2. 6: Three-port half-bridge dc/dc converter

As shown in Figure 2.7, a similar topology has been used in [23] to interface hybrid energy storage as the battery and ultra-capacitor to achieve high overall performance. It can interface current source input, and can achieve ZVS for all six main switches by the phase shift control. This paper also discusses the power topology operation and the control aspects of dynamic characteristics analysis and the control strategy.

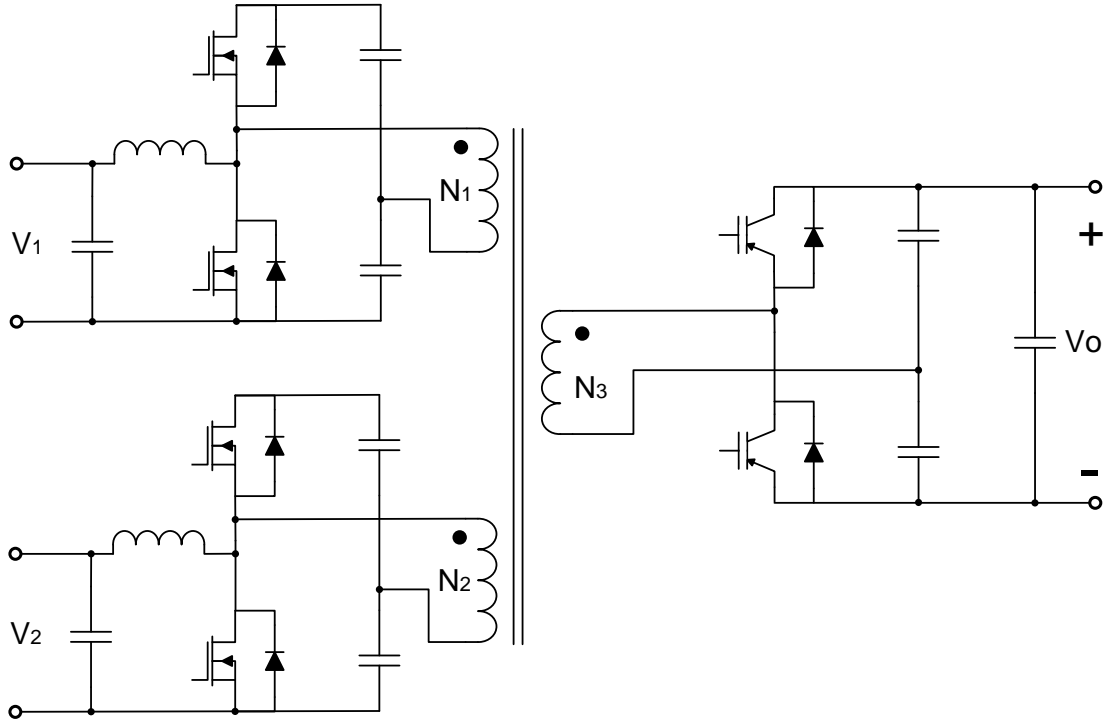


Fig. 2. 7: Triple-half-bridge bidirectional dc/dc converter

The above-mentioned topologies adopt a multi-winding transformer to couple different power ports. Therefore, all ports are fully isolated with each other. However, some applications do not require all ports to be fully isolated, and the share of some grounds may allow less component and fewer transformer windings. As shown in Figure 2.8, a topology in [15] is intended for future hybrid and fuel cell vehicles which may have three voltage nets: 14V, 42V and high voltage (>200V) buses. A soft-switched dc-dc converter using four switches has been proposed to interconnect these three nets. Its power flow management is based on a combined duty ratio and phase shift control, but soft-switching range is limited when the phase shifts between two very different voltage levels to have large current swing.

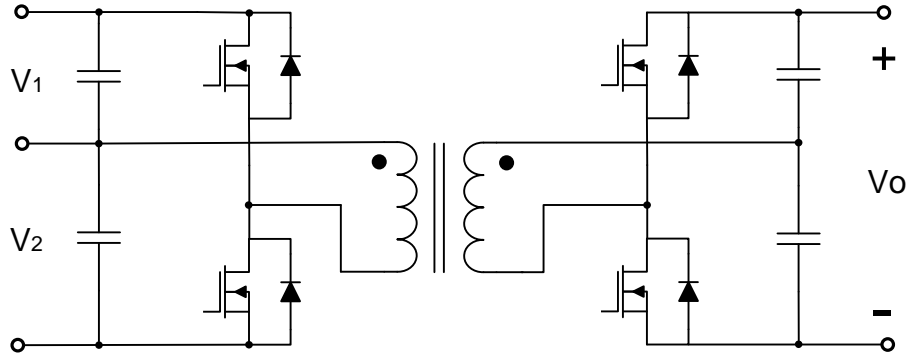


Fig. 2. 8: Reduced part, triple-half-bridge bidirectional dc/dc converter

To sum up, these multi-port topologies can be classified as two categories: non-isolated topologies [6]-[14] and isolated topologies [15]-[28]. Non-isolated multi-port converters usually take the form of buck, boost, buck-boost, etc, featuring compact design and high power density; isolated multi-port converters using bridge topologies have the advantages of flexible voltage levels and high efficiency since high frequency transformer and soft-switching techniques are used. As well, isolation may be required for certain critical applications.

2.3. Summary

From the above literature review, all of the reported multi-port solutions suffer from at least one of the following drawbacks:

1. Lack of bidirectional capability to interface the battery;
2. No isolation capability or having too many isolating power ports with a bulky multi-winding transformer;

3. Using too many active switches and passive components which can not justify the multi-port features like low component count and compact structure;
4. Lack of soft-switching capability to allow high frequency design to further shrink the converter size;
5. The power among different power ports can not be transferred individually or simultaneously.

For our applications, it requires at least one bidirectional port and only one isolated output port. The topologies with all ports isolated are over-qualified and unnecessary for our application. Therefore, the topologies with only one isolated port are sufficient. From this point of view, the topology as shown in Figure 2.8 is a good candidate. But as mentioned above, it has four main switches and its soft-switching range is limited when ports' voltage change largely. Therefore the main switches can still be reduced. Besides, our topology needs to have multiple input ports, but all above-mentioned multi-input topologies do not have ZVS soft-switching capability to allow high frequency designs. To sum up, the proposed topologies in this dissertation have the following features:

1. Have bidirectional capability;
2. Have one isolation port;
3. Low component count: have N switches for the N -port converter, that is three switches for a three-port converter;
4. ZVS for all main switches to allow high switching frequency designs;
5. The power among different power ports can be transferred individually or simultaneously.

For space applications in Chapter 3 and Chapter 4, the proposed three-port topology will have only three main switches, and it can achieve soft-switching for all the main switches for a wide input voltage range. Its main components are only three main switches, one clamping diode, one transformer, two rectification diodes and one inductor. For renewable energy applications in Chapter 5, based on the three-port converter, the proposed four-port topology adds one switch and diode to incorporate one more input port while still achieving ZVS for all four main switches. The power from both input ports can be transferred to the output port or battery port individually or simultaneously. If only one input source is available, the four-port topology reduces into the three-port operation which is almost the same as the topology proposed in Chapter 3. In Chapter 5, the proposed topology is extended into interface N power ports while still achieving ZVS for all main switches and still having very low component count. Therefore, this topology is a valuable choice for both space applications requiring minimum mass and renewable energy applications requiring minimum cost.

CHAPTER 3: AN INTEGRATED THREE-PORT DC/DC CONVERTER: CIRCUIT ANALYSIS, MODELING AND CONTROL

3.1. General Description

This chapter discusses the circuit operation, the modeling and the control of an integrated three-port converter for space applications. From topology point of view, this new three-port topology is derived by adding a diode and a switch across the transformer primary side, which provides one more control freedom and ensures a clamping path for the leakage energy to create ZVS condition for all the main switches. Since it is a new three-port converter, the small signal model will be desired to achieve the close loop controller design. Especially for such kind of multi-input multi-output (MIMO) control system, a precise model is critical to provide guidance through the whole control design process. Moreover, since various control loops are cross coupled with each other, a decoupling method suitable for such a MIMO system is proposed to allow separate controller design for each power port's feedback loop. The modeling procedure is based on the traditional state-space averaging method, and is suitable to be applied for other multi-port converters.

3.2. Circuit and Topology

This section introduces the three-port topology. As shown in Figure 3.1, it is a modified version of PWM half bridge converter which includes three basic circuit stages within a constant-frequency switching cycle to provide two independent control variables, namely duty-cycles d_1

and d_2 which are to control S1 and S2, respectively. This allows tight control over two of the converter ports, while the third port provides the power balance in the system. The switching sequence ensures a clamping path for the energy of the leakage inductance of the transformer at all times. This energy is further utilized to achieve zero-voltage switching (ZVS) for all primary switches for a wide range of source and load conditions. The circuit operation, the ZVS analysis and the DC analysis will be discussed as follows.

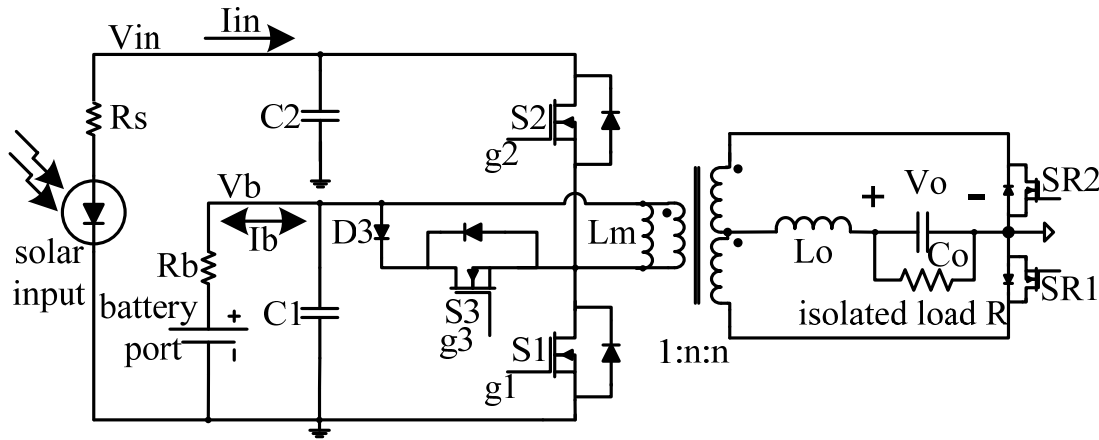


Fig 3. 1: Three-port modified half-bridge converter topology, which can achieve ZVS for all three main switches (S1, S2, S3) and adopt synchronous rectification for the secondary side to minimize conduction loss.

3.2.1. Circuit Operation Principles

The steady-state waveforms of the three-port converter are shown in Figure 3.2, and the operation stages in one switching cycle are shown in Figure 3.3.

Stage 1 (t_0 - t_1): Before this stage begins, the body diode of S1 is forced on to recycle the energy in the transformer leakage inductor, and the output is freewheeling. At time t_0 , S1 is gated on with ZVS, and then the leakage inductor is reset to zero and reverse-charged.

Stage 2 (t_1 - t_2): At time t_1 , the transformer primary current increases to reflected current of i_o , the body diode of SR2 is blocked, and the converter starts to deliver power to output.

Stage 3 (t_2 - t_3): At time t_2 , S1 is gated off, causing the leakage current i_p to charge C1 and discharge C2.

Stage 4 (t_3 - t_4): At time t_3 , the voltage across C2 is discharged to zero, and D2 conducts to carry the current, which provides ZVS condition for S2. During this interval, the output is freewheeling.

Stage 5 (t_4 - t_5): At time t_4 , S2 is gated on with ZVS, and then the leakage inductor is reset to zero and reverse-charged. Output inductor current drop between t_2 and t_5 is due to the leakage inductor discharge/charge.

Stage 6 (t_5 - t_6): At time t_5 , the transformer primary current increases to reflected current of i_2 , the body diode of SR1 is blocked, and the converter starts to deliver power to output.

Stage 7 (t_6 - t_7): At time t_6 , S2 is gated off, causing the leakage current i_p to charge C2 and discharge C1.

Stage 8 (t_7 - t_8): At time t_7 , the voltage across D3 is discharged to zero, and D3 conducts. Since S3 is gated on before this time, the leakage current freewheels through D3 and S3 so that the leakage energy is trapped. On the secondary side, output inductor current freewheels through SR1 and SR2.

Stage 9 (t_8 - t_9): At time t_8 , S3 is gated off, causing the trapped leakage energy to discharge C1 and charge C2.

Stage 10 (t_9 - t_{10}): At time t_9 , the voltage across S1 is discharged to zero, and D1 conducts to carry the current, which provides ZVS condition for S1. During this interval, the output is freewheeling.

This is the end of the switching cycle.

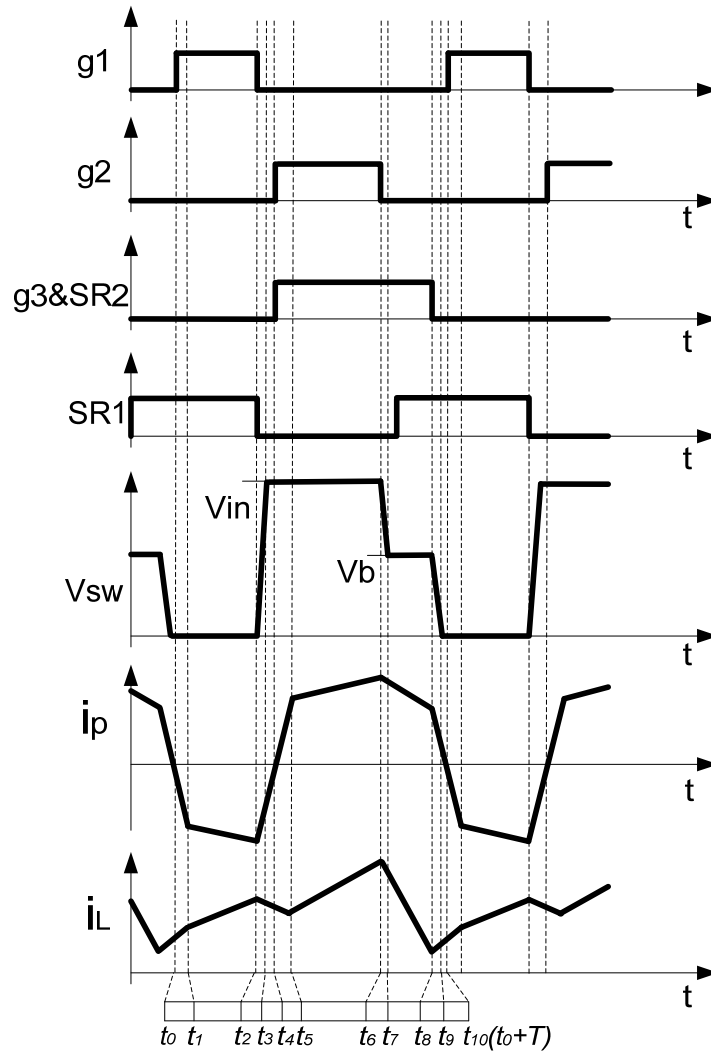
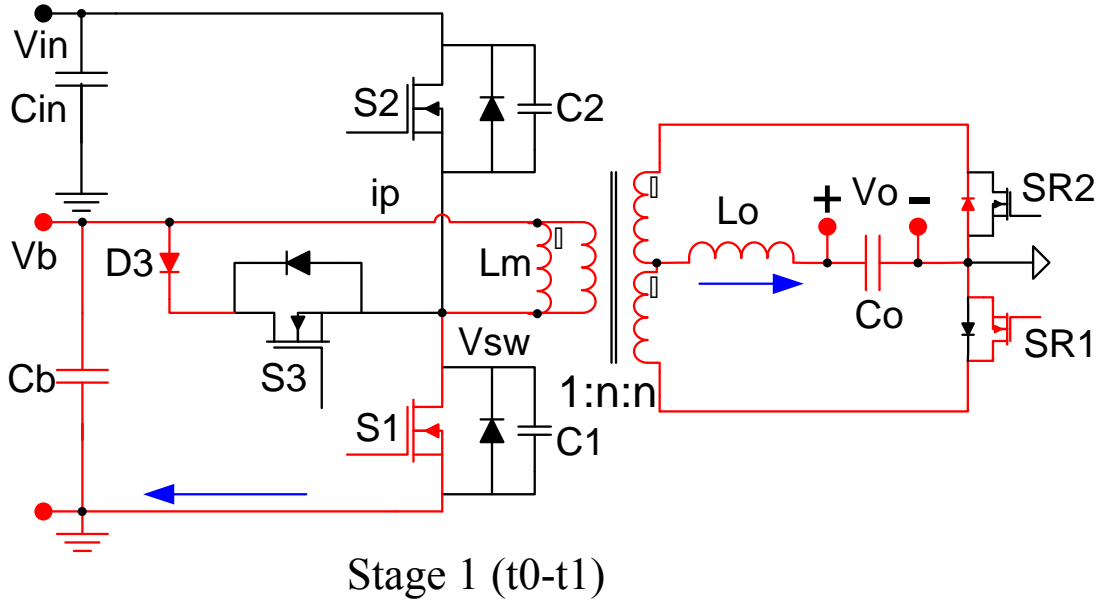
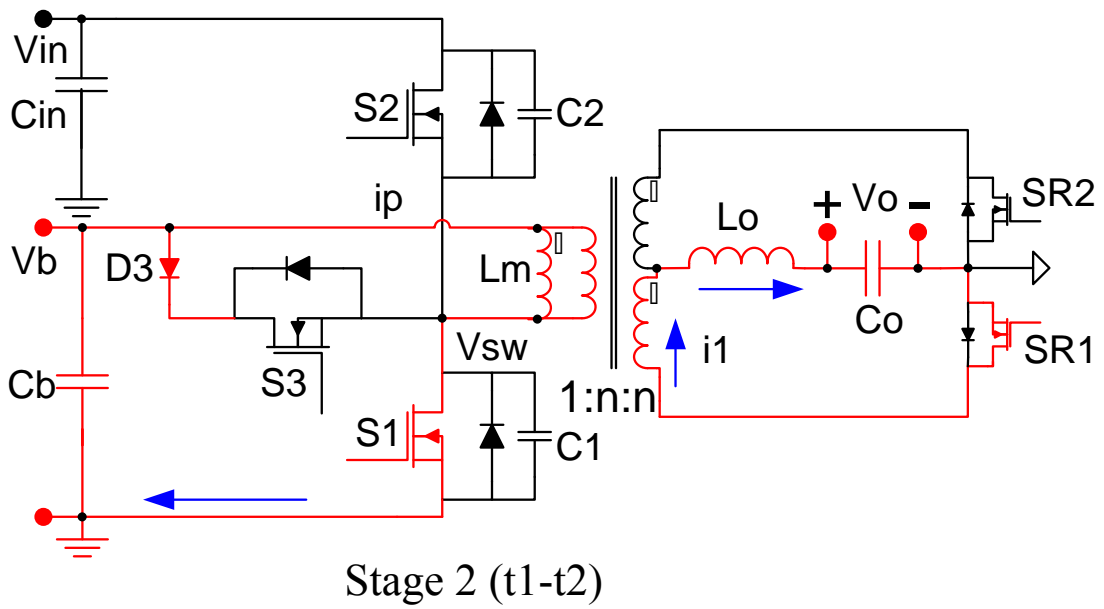


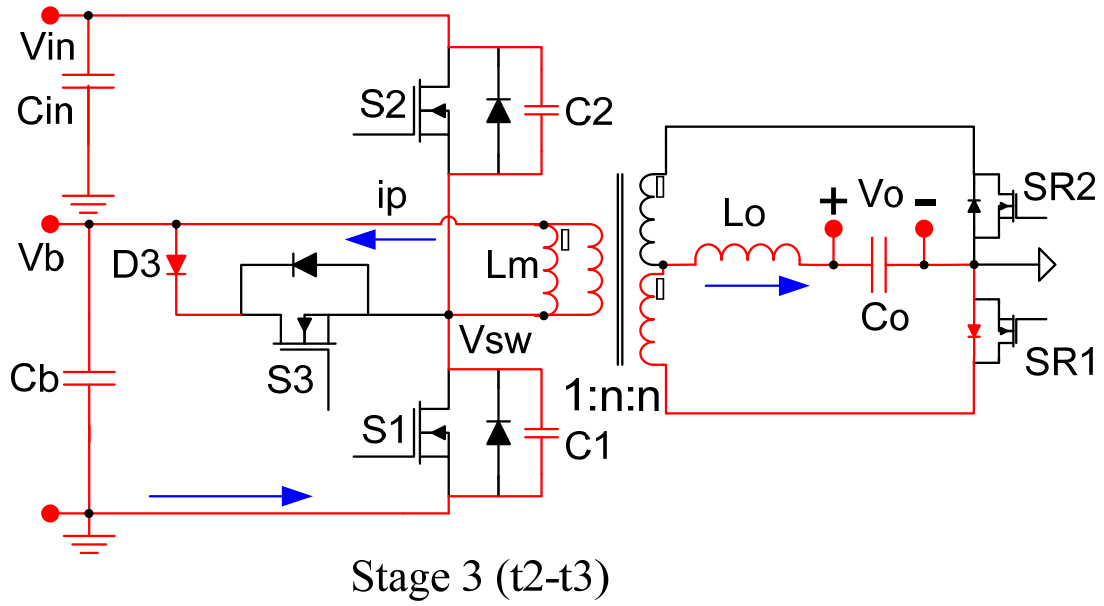
Fig 3. 2: Steady state waveforms of the three-port half-bridge converter



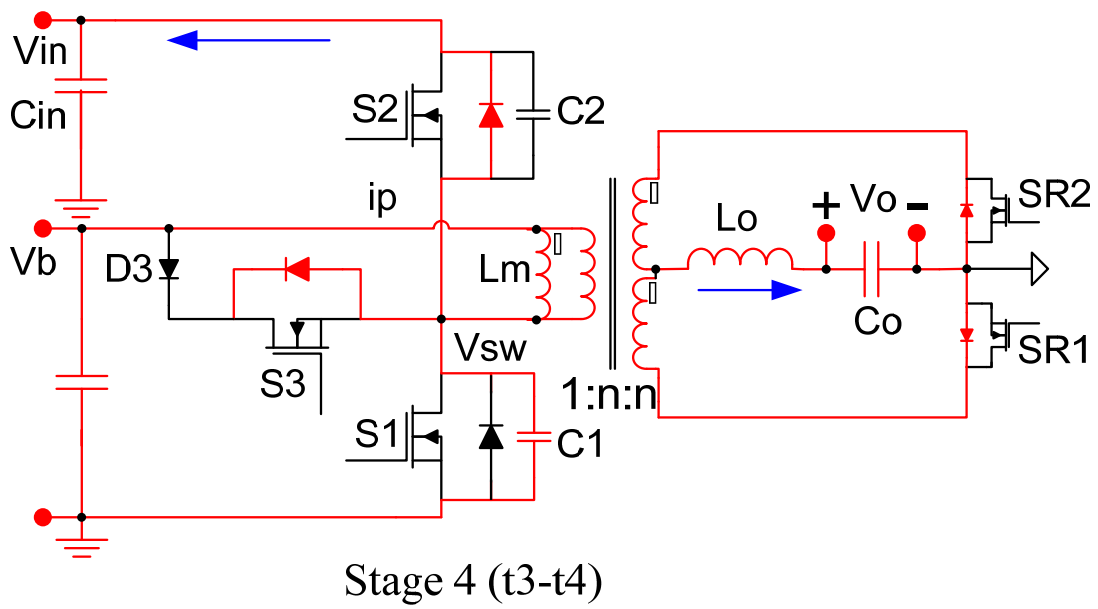
(a). Stage 1 operation



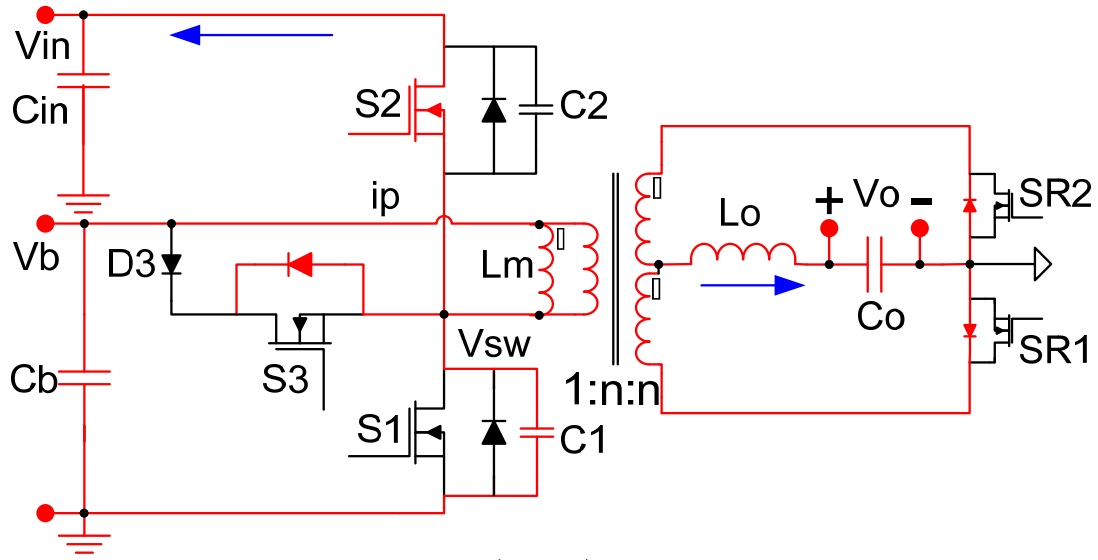
(b). Stage 2 operation



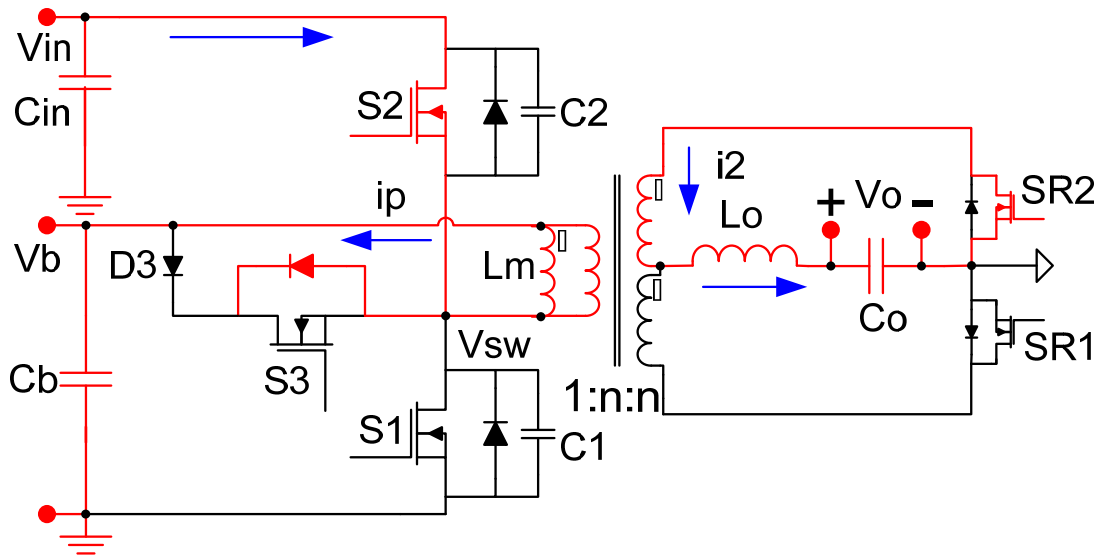
(c). Stage 3 operation



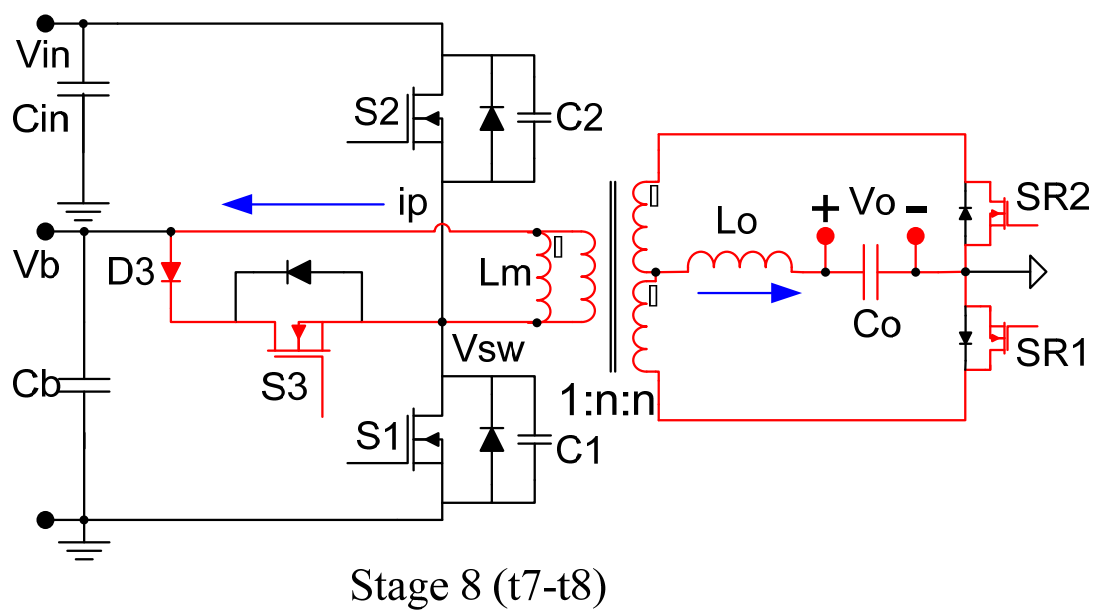
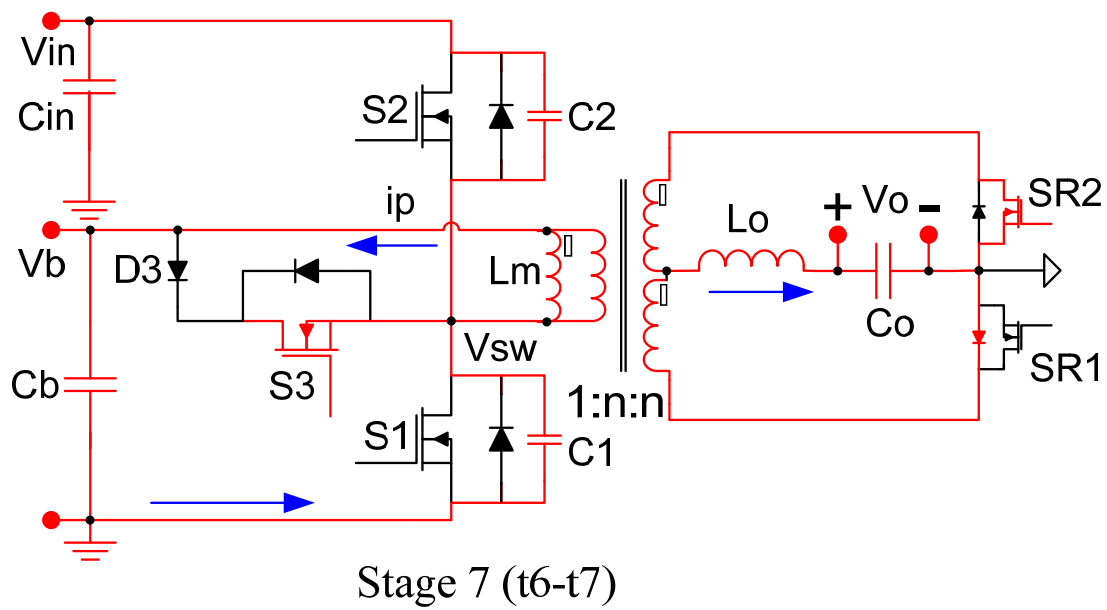
(d). Stage 4 operation

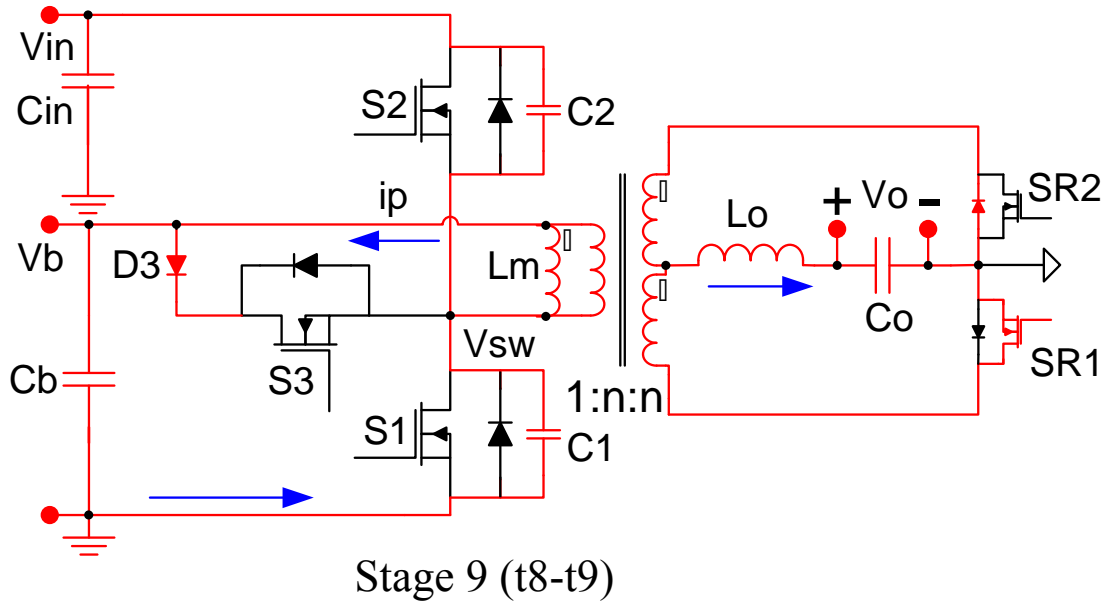


(e). Stage 5 operation

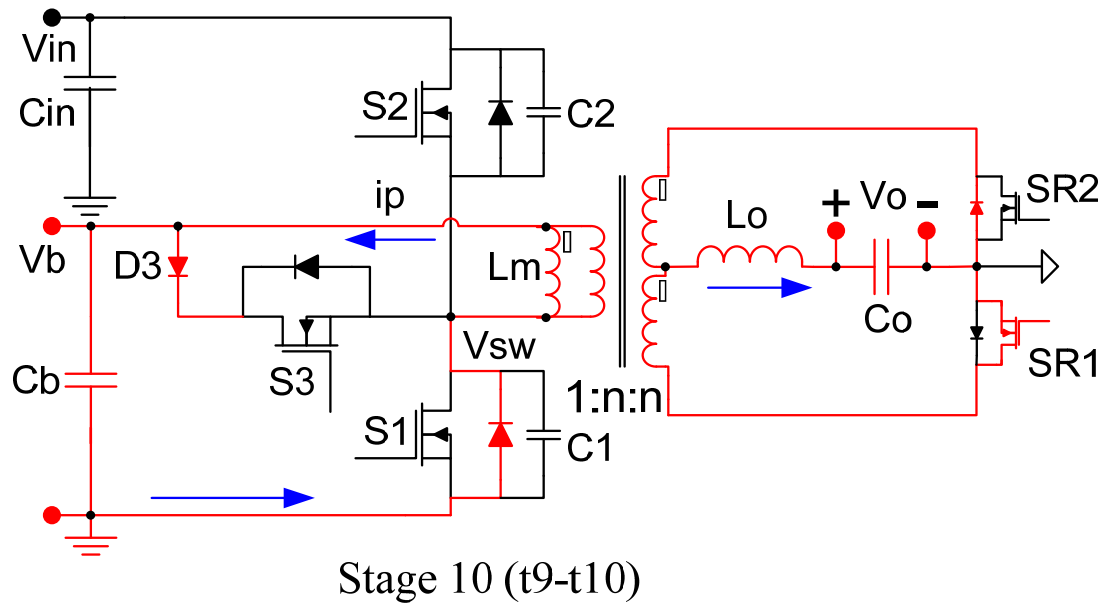


(f). Stage 6 operation





(i). Stage 9 operation



(j). Stage 10 operation

Fig 3. 3: Operation stages of the three-port half-bridge converter

3.2.2. ZVS Analysis

When loading the output port, ZVS of the switches S1 and S2 can be realized through the energy stored in the transformer leakage inductor, while ZVS of S3 is always maintained because D3 will be forced on when the switching node voltage V_{sw} is connected to the input voltage V_{in} .

After S3 is turned off, the leakage energy is released to discharge C1 and charge C2 and S3's parasitic capacitance C3. The following condition should be satisfied to achieve ZVS for S1:

$$\frac{1}{2} \cdot L_k \cdot (I_M + n \cdot I_o)^2 > \frac{1}{2} \cdot C_{oss} \cdot (V_{in}^2 + V_{bi}^2), \quad I_M + n \cdot I_o > 0 \quad \text{Eq. 3.1}$$

Where L_k is the transformer leakage inductance, C_{oss} is the MOSFET parasitic capacitance of S1, S2 and S3, V_{in} is the input voltage, I_o is the output load current, I_M is the transformer magnetizing current which is determined by the following equation.

$$I_M = \frac{I_{bi} + (D_1 - D_2)nI_o}{D_1 + D_2} \quad \text{Eq. 3.2}$$

After S1 is turned, the leakage energy may charge C1 and discharge C2 and S3's parasitic capacitance C3 to achieve ZVS for S2:

$$\frac{1}{2} \cdot L_k \cdot (I_M - n \cdot I_o)^2 > C_{oss} \cdot V_{in}^2 + \frac{1}{2} \cdot C_{oss} \cdot V_{bi}^2, \quad I_M - n \cdot I_o < 0 \quad \text{Eq. 3.3}$$

Where I_{bi} is the battery current. Therefore, when I_o is small and I_M is large, $I_M - n \cdot I_o < 0$ can not be met, and ZVS of S2 is lost. Worst case scenario would be when loading the battery port and leaving output port open, $I_M > 0$, so ZVS of S2 can not be achieved.

3.2.3. DC Analysis

Assuming an ideal lossless converter, the steady-state voltage governing relations between different port voltages can be determined by equating the voltage-second product across the converter's two main inductors to zero. First, using volt-second balance across the primary transformer magnetizing inductance, when operating in continuous conduction mode (CCM), we have:

$$V_{bi} \cdot D_1 = (V_{in} - V_{bi}) \cdot D_2 \quad \text{Eq. 3.4}$$

With $V_{in} = V_{C1} + V_{C2}$, and $V_{bi} = V_{C1}$, the voltage at the bidirectional port, V_{bi} , may be given by:

$$V_{bi} = \frac{D_2}{D_1 + D_2} V_{in} \quad \text{Eq. 3.5}$$

Where V_{in} is the voltage of the input port, D_1 and D_2 are the duty-cycles of S1 and S2, respectively, and T is the duration of the switching cycle. Assuming CCM operation, the volt-second balance across the load filter inductor yields:

$$D_1 T (nV_{bi} - V_o) + D_2 T (nV_{in} - nV_{bi} - V_o) - (1 - D_1 - D_2) T V_o = 0$$

$$V_o = 2 \frac{D_1 D_2}{D_1 + D_2} n V_{in} \quad \text{Eq. 3.6}$$

Where n is the turns ratio of the transformer, and V_o is the load-port voltage. Using Equation 3.5, this can also be re-written as:

$$V_o = 2 D_1 n V_{bi} \quad \text{Eq. 3.7}$$

Assuming a lossless converter, steady-state port currents can be related by applying the power conservation principle as follows:

$$V_{in}I_{in} = V_{bi}I_{bi} + V_oI_o \quad \text{Eq. 3.8}$$

Where I_{in} , I_{bi} , I_o are the average input, bidirectional battery, and load currents, respectively.

3.3. Modeling and Control

This section introduces a modeling method specially tailored for deriving multi-port converter's small signal models under different modes of operation. A decoupling network is then introduced to allow separate controller designs. Since there are various modes of operation, it is challenging to define different modes and further to implement autonomous mode transition based on the energy state of the three power ports. Various modes of operation are defined. And a competitive method is used to realize smooth and seamless mode transition.

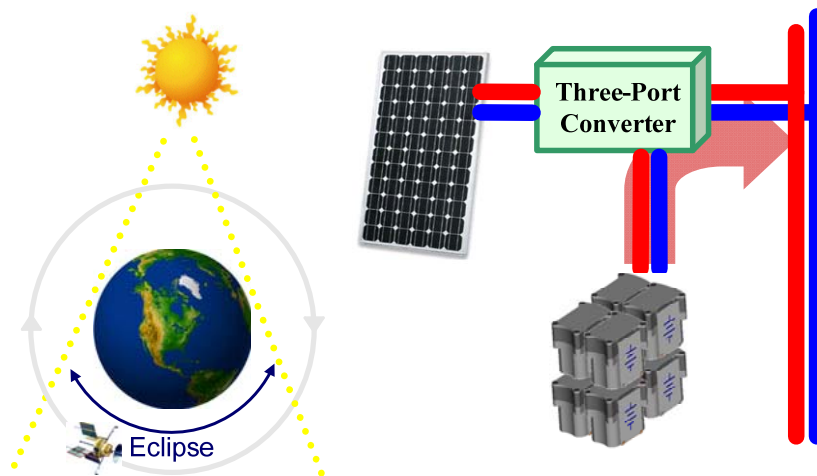
3.3.1. Mode Definition

Having different operational modes is one of the unique features for multi-port converters. As illustrated in Figure 3.4, orbital satellite's power platform experiences periods of insolation and eclipse during each orbit cycle, with insolation period being longer. Since Maximum Power Point Tracking (MPPT) can notably boost solar energy extraction of a photovoltaic (PV) system, the longer insolation period means that MPPT is more often operated to allow a smaller solar array while managing the same amount of load. Two assumptions are made to simplify analysis: 1) Load power is assumed to be constant; 2) Battery over-discharge is ignored because PV arrays

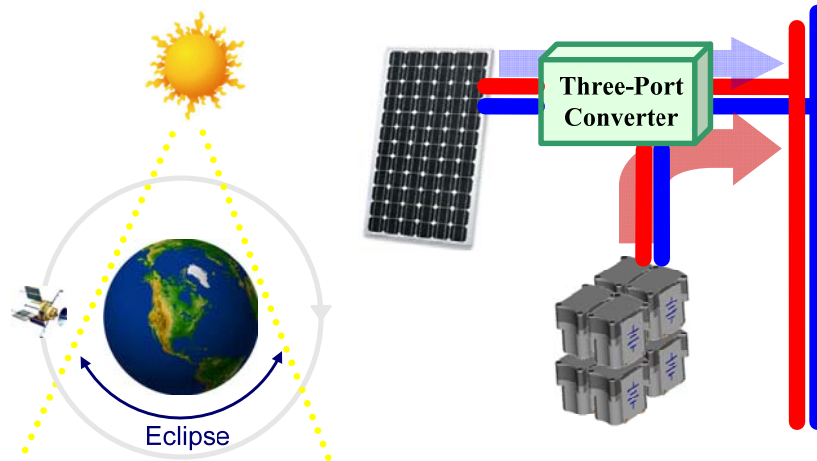
and batteries are typically over-sized in satellites to provide some safety margins. Four stages in satellite's one orbit cycle yield two basic operational modes as follows.

In Battery-balanced Mode (Mode 1), the load voltage is tightly regulated, and the solar panel operates under MPPT control to provide maximum power. The battery preserves the power balance for the system by storing unconsumed solar power, or providing the deficit during high load intervals. Therefore, the solar array can be scaled to provide average load power while the battery provides the deficit during peak power of load, which is attracting to reduce solar array mass.

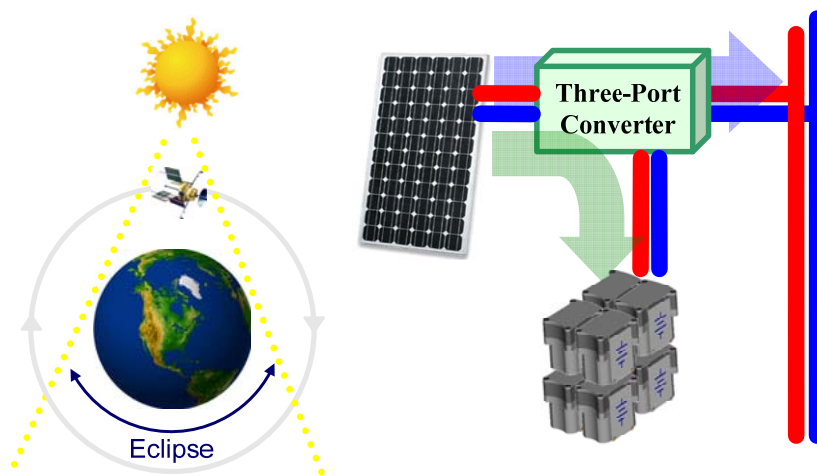
In Battery-regulation Mode (Mode 2), the load is regulated and sinks less power than is available, while the battery charge rate is controlled to prevent overcharging. This mode stops to start Mode 1 when the load increases beyond available solar power. That is, battery parameter falls below either maximum voltage setting or maximum current setting.



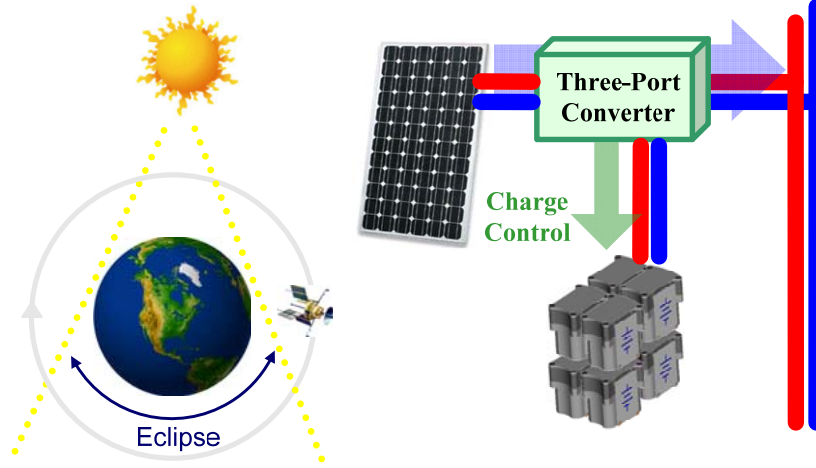
(a). Stage I operation (eclipse period)



(b). Stage II operation (initial insolation)



(c). Stage III operation (increased insolation)



d). Stage IV operation (battery charge control)

Fig 3. 4: Different operational modes in satellite's one orbit cycle. Three-port converter can achieve MPPT, battery charge control and load regulation depending on available solar power, battery state of charge and load profile. In stage I, battery acts as the exclusive source during eclipse period. In stage II&III, solar power is maximized to decrease battery state of discharge in stage II for initial insolation period and then to increase battery state of charge in stage III for increased insolation period. In stage IV, battery charge control is applied to prevent battery over-charging and extend battery service life.

3.3.2. Control Structure

The multi-objective control architecture which aims to regulate different power ports is shown in Figure 3.5, control loops are named as follows: input voltage regulation (IVR), output voltage regulation (OVR), battery voltage regulation (BVR), and battery current regulation (BCR).

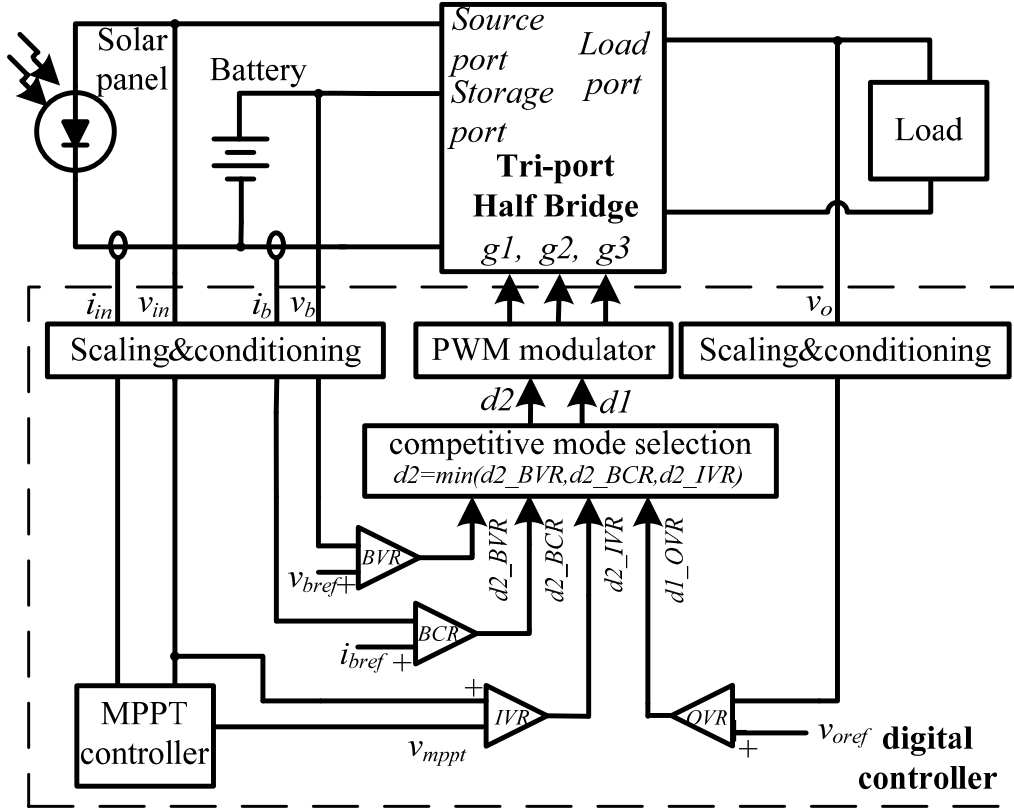


Fig 3. 5: Three-port converter's control architecture to achieve MPPT for solar port, battery charge control for battery port and meanwhile always maintaining voltage regulation for output port. OVR is to control d_1 , and the rest of control loops (BVR, BCR and IVR) are competing the minimum value to control d_2 .

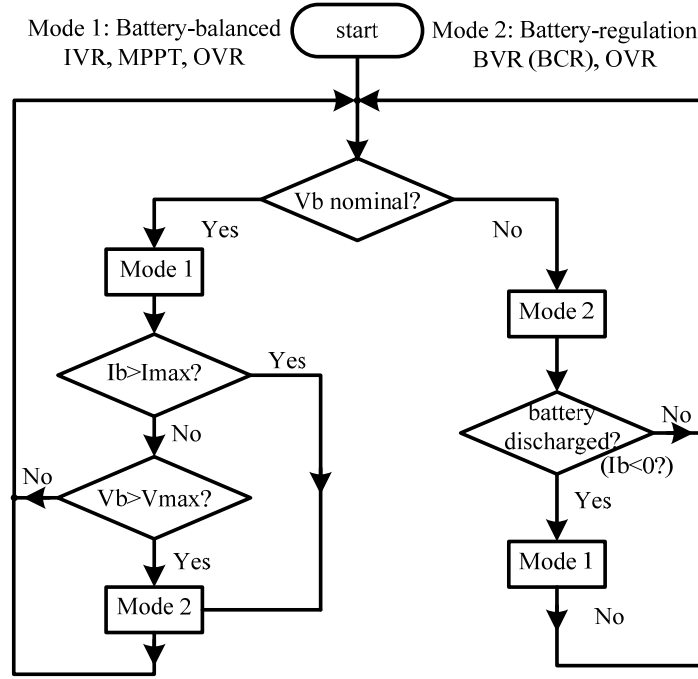
The output port loop is simply a voltage-mode control loop, closed around the load voltage, and duty cycle d_1 is used as its control input. According to the DC circuit equation $V_o = 2V_b \cdot D_1 \cdot n$, output voltage V_o can only be controlled by d_1 , since battery voltage V_b is almost constant and transformer turn's ratio n is fixed. As a result, d_2 is assigned to control either input port or battery port.

The IVR loop is used to regulate the solar panel voltage to its reference value. The reference is provided by an MPPT controller [34] using perturb and observe algorithm, and represents an estimate of the optimal operating voltage, duty cycle d_2 is used as the control input when realizing the IVR loop. Otherwise, d_2 can be decided by battery control loop which has two controllers, BVR and BCR. It should be mentioned that BCR is to prevent battery over-current, so it can be considered a protection function. Under normal operation, only one of two loops (IVR or BVR) will be active depending on the battery state of charge. Therefore, whether d_2 is commanded by IVR, BVR or BCR depends on which mode it is in.

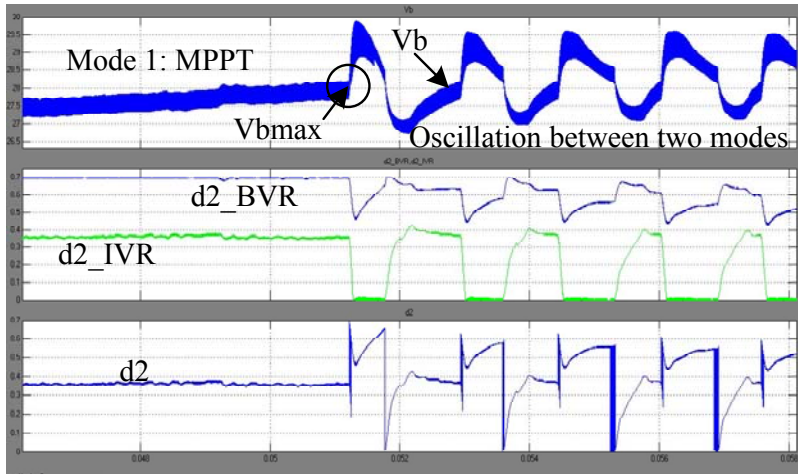
3.3.3. Autonomous Mode Transitions

The mode of operation is determined according to the present operating conditions such as available solar power, battery state of charge and load profile. Figure 3.6(a) gives the flow chart for traditional mode transition algorithm. Mode 1 will be the default mode, where the converter will spend most of the time. Mode 1 is desirable because it enables maximum solar power input. When the converter is in Mode 1, the controller will continually check the battery parameter, and then switch to Mode 2 if the maximum setting voltage or current is reached. Once the converter is in Mode 2, it stays there until the load increases beyond available power. Although this algorithm is straightforward, without careful design of mode transitions, system oscillation will occur due to duty cycle's instant change. In a simulation as shown in Figure 3.6(b), when battery voltage reaches its maximum setting V_{bmax} , it switches to Mode 2 suddenly, that is, d_2 is switched

from a nominal value to d_{2_BVR} which is saturating at that moment, causing a battery voltage spike. But when the spike of V_b reduces below V_{bmax} , it will force the converter to switch back to Mode 1 and cause d_2 another step change to introduce another voltage spike. And thus this process continues for a long time. Besides, small battery voltage spike can cause huge current spike which is usually large enough to break the circuit because of small battery internal resistance.



(a)



(b)

Fig 3. 6: (a) Conventional mode transition algorithm flow chart which is inclined to cause oscillation; (b) Oscillation between Mode 1 and Mode 2 because of instant switching of duty cycle value

In order to avoid the sudden transition between modes, the autonomous mode transition is proposed in a competitive manor as shown in Figure 3.7(a). BVR, BCR and IVR are run in parallel to compete for minimum value in order to win control over d_2 . Again, BCR will not be active during normal operation. So battery control is mainly BVR loop operation. For example, when converter is in Mode 1 with MPPT to maximize solar power, d_2 will be determined by IVR loop, while BVR output is saturated at its upper limit because battery voltage does not reach its maximum setting. BVR will start to take control over d_2 when battery maximum setting V_{bmax} is reached and BVR output goes down to win the minimum function. It should be noted that if IVR loop loses control, MPPT function needs to be disabled accordingly because of MPPT algorithm's inherent noise issue [33]. For example, in Figure 3.7(b), when converters are run in MPPT to maximize solar power, d_2 will be determined by IVR loop, while BVR output is saturated at its upper limit because battery maximum voltage value is not reached. BVR will start to take control when V_{bmax} is reached and BVR output goes down to win the minimum function. Figure 3.7(c) shows Mode 2 to Mode 1 transition when the battery starts to discharge for sudden increase of load demand or decrease of solar power. This method simplifies the algorithm.

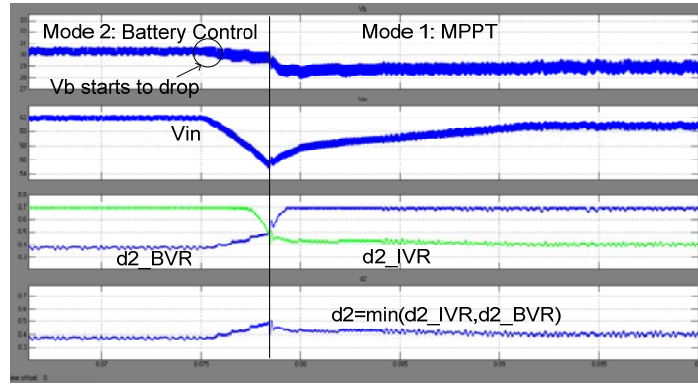
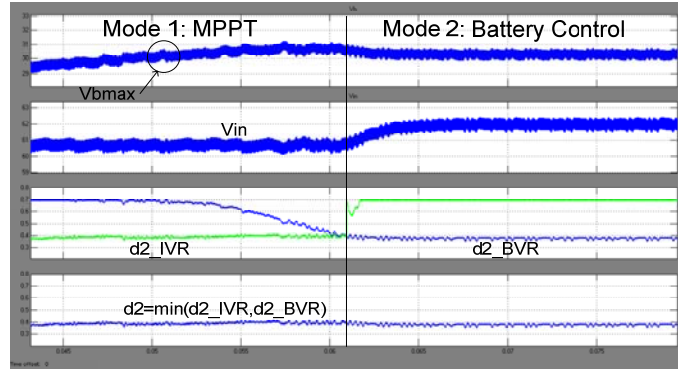
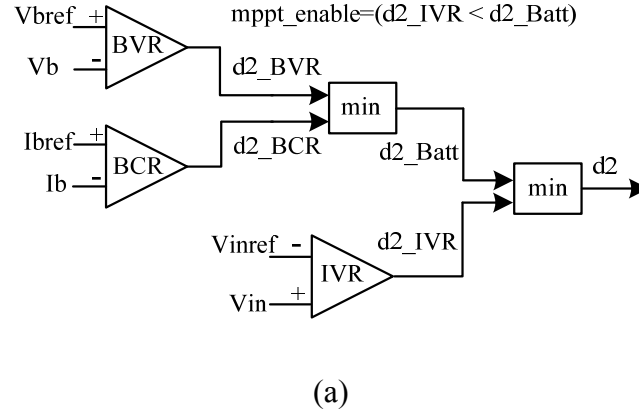


Fig 3. 7: (a) the proposed minimum function competitive method to allow smooth transition of modes; (b) Mode 1 to Mode 2 transition with no oscillation; (c) Mode 2 to Mode 1 transition with no oscillation.

3.3.4. Converter Modeling and Controller Design

Small signal model is the basis for optimized controller design. Especially for such a complicated MIMO system of three-port converter, an effective model will be helpful to realize closed loop control and furthermore to optimize the converter dynamics. Since there are two modes of operation for the three-port converter, small signal models in both modes need to be obtained separately. Unlike conventional two-port converter, multi-port converter is high-order system, and the symbolic derivation of these plant transfer functions is fairly tedious, so it is difficult to obtain values of poles and zeros for analysis. Alternatively, the dynamics of the plant can be described in a matrix form, therefore computer software is used to plot the bode graph of different transfer functions. A common problem about MIMO system is the existence of various interacting control loops which complicate compensator designs; therefore a decoupling network is introduced to allow separate controller designs for each of the three power port.

3.3.4.1 *Three-port Converter Modeling during Battery-Regulation Mode*

Before deriving for small signal transfer functions of the converter, state equations for four energy storage element during each circuit stage are developed. For Battery-regulation Mode, these include the battery capacitor C_I , the transformer magnetizing inductance L_m , the output inductance L_o , and the output capacitance C_o . There are three main circuit stages as illustrated in Figure 3.8.

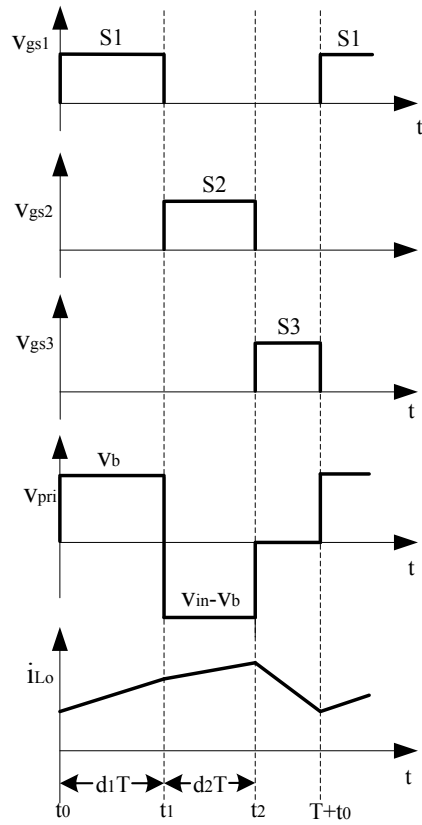


Fig 3. 8: Basic waveforms of the three-port converter. v_{pri} and i_{Lo} represent transformer primary side voltage and output inductor current, respectively.

Stage I ($t_0 - t_1$): In stage I, S1 is gated ON, applying a positive voltage to the transformer primary side, while output inductor is charging. Synchronous Switch SR1 is gated ON to allow current flow through output inductor L_o . Current of battery port filter capacitor is equal to the sum of battery current, transformer magnetizing inductor current and reflected secondary side current. The state equation in this stage is as follows.

$$\begin{cases} C_1 \cdot dv_{C1} / dt = \frac{-v_{C1}}{R_b} + i_{Lm} - n \cdot i_{Lo} \\ L_m \cdot di_{Lm} / dt = -v_{C1} \\ L_o \cdot di_{Lo} / dt = v_{C1} \cdot n - v_o \\ C_o \cdot dv_o / dt = i_{Lo} - \frac{v_o}{R} \end{cases} \quad Eq. 3.9$$

Stage II (t1 - t2): In stage II, S2 is gated ON, a negative voltage is applied to the transformer primary side, and output inductor is still charging. Synchronous Switch SR2 is gated ON to allow a current flow path through L_o . The transformer primary voltage is input voltage subtracts battery voltage, and thus output inductor charging rate changes accordingly. The state equation in this stage is as follows.

$$\begin{cases} C_1 \cdot dv_{C1} / dt = \frac{-v_{C1}}{R_b} + i_{Lm} + n \cdot i_{Lo} \\ L_m \cdot di_{Lm} / dt = v_{C2} - v_{C1} \\ L_o \cdot di_{Lo} / dt = (v_{C2} - v_{C1}) \cdot n - v_o \\ C_o \cdot dv_o / dt = i_{Lo} - \frac{v_o}{R} \end{cases} \quad Eq. 3.10$$

Stage III (t2 - T+t0): In stage III, S3 is gated ON, zero voltage is applied to the transformer primary side due to middle branch (S3 and D3 path)'s clamping, and output inductor is discharging. This allows both the magnetizing and output inductor currents to free-wheel. Both SR1 and SR2 are turned ON, therefore output inductor current distributes into both of rectifying paths. The state equation in this stage is as follows.

$$\begin{cases} C_1 \cdot dv_{C1} / dt = \frac{-v_{C1}}{R_b} \\ L_m \cdot di_{Lm} / dt = 0 \\ L_o \cdot di_{Lo} / dt = -v_o \\ C_o \cdot dv_o / dt = i_{Lo} - \frac{v_o}{R} \end{cases} \quad \text{Eq. 3.11}$$

Before we perform the averaging to three different state equations, we consider that the state variables have a perturbation \hat{x} superimposed to the DC value X ,

$$x = X + \hat{x} \quad \text{Eq. 3.12}$$

And similarly, $d = D + \hat{d}$, $v = V + \hat{v}$.

To obtain the small-signal model, we assume that the perturbations are small, i.e., $\hat{d} \ll D$, $\hat{v} \ll V$, etc. We also assume that the perturbations do not vary significantly during one switching period, which means that the dynamic models that will be obtained are valid for frequencies much smaller than the switching frequency. If we substitute Eq.3.12 in Eq.3.9, Eq.3.10, Eq.3.11, apply the averaging to three state equations multiplied with corresponding duty cycle value, and then neglect second order terms, we obtain small-signal equations which are demonstrated as follows.

$$\left\{ \begin{array}{l} C_1 \cdot d\hat{v}_{C1} / dt = \frac{-\hat{v}_{C1}}{R_b} + \hat{i}_{Lm} \cdot (D_1 + D_2) + n \cdot \hat{i}_{Lo} \cdot (D_2 - D_1) + I_{Lm} \cdot (\hat{d}_1 + \hat{d}_2) + \frac{n \cdot V_o \cdot (\hat{d}_2 - \hat{d}_1)}{R} \\ L_m \cdot d\hat{i}_{Lm} / dt = -\hat{v}_{C1} \cdot (D_1 + D_2) - \frac{(\hat{d}_1 + \hat{d}_2) \cdot D_2 \cdot V_{in}}{(D_1 + D_2)} + \hat{d}_2 \cdot V_{in} \\ L_o \cdot d\hat{i}_{Lo} / dt = \hat{v}_{C1} \cdot n \cdot (D_1 - D_2) - \hat{v}_o + \frac{(\hat{d}_1 - \hat{d}_2) \cdot n \cdot D_2 \cdot V_{in}}{(D_1 + D_2)} + \hat{d}_2 \cdot n \cdot V_{in} \\ C_o \cdot d\hat{v}_o / dt = \hat{i}_{Lo} - \frac{\hat{v}_o}{R} \end{array} \right. \quad Eq. 3.13$$

Therefore the system can be represented in a matrix form using a state-space model after converting Eq.3.13 into frequency domain. The state-space model takes the following form.

$$dX / dt = A \cdot X + B \cdot U, Y = I \cdot X \quad Eq. 3.14$$

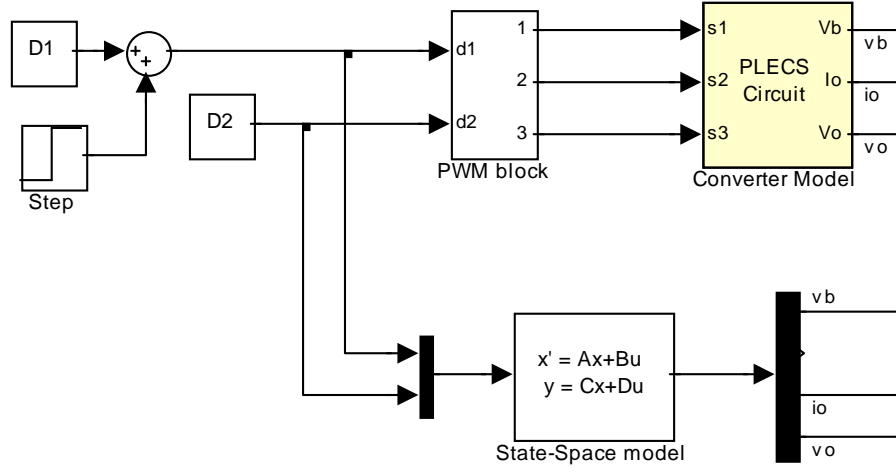
Where X is a matrix containing the state variables V_{C1} , i_{Lm} , i_{Lo} and V_o , U is a matrix containing the control inputs d_1 and d_2 , Y is a matrix containing the system outputs, I is the identity matrix. For this model the four state variables are also the system outputs. Filling in the A and B matrices using the state equations gives the following result.

$$A = \begin{bmatrix} -\frac{1}{R_b \cdot C_1} & \frac{(D_1 + D_2)}{C_1} & \frac{n \cdot (D_2 - D_1)}{C_1} & 0 \\ -\frac{(D_1 + D_2)}{L_m} & 0 & 0 & 0 \\ \frac{n \cdot (D_1 - D_2)}{L_o} & 0 & 0 & -\frac{1}{L_o} \\ 0 & 0 & \frac{1}{C_o} & -\frac{1}{R \cdot C_o} \end{bmatrix}, \quad X = \begin{bmatrix} \hat{v}_{C1} \\ \hat{i}_{Lm} \\ \hat{i}_{Lo} \\ \hat{v}_o \end{bmatrix}$$

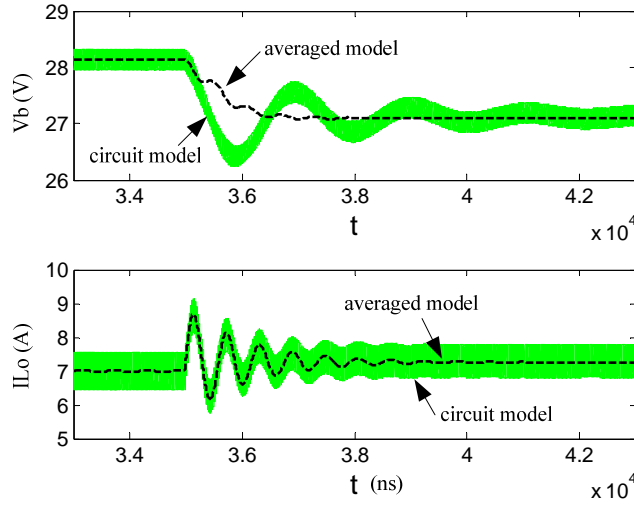
$$B = \begin{bmatrix} \frac{I_{Lm} - n \cdot V_o / R}{C_1} & \frac{I_{Lm} + n \cdot V_o / R}{C_1} \\ \frac{D_2 \cdot V_{in}}{(D_1 + D_2) \cdot L_m} & \frac{D_1 \cdot V_{in}}{(D_1 + D_2) \cdot L_m} \\ \frac{n \cdot D_2 \cdot V_{in}}{(D_1 + D_2) \cdot L_o} & \frac{n \cdot D_1 \cdot V_{in}}{(D_1 + D_2) \cdot L_o} \\ 0 & 0 \end{bmatrix}, \quad U = \begin{bmatrix} d1 \\ d2 \end{bmatrix}$$

Eq. 3.15

In order to verify the derived state-space averaged model, MATLAB's Simulink is used to compare the averaged model at the bottom with the actual switching converter model on the top as shown in Figure 3.9(a). The converter model is realized by actual switches and passive components, while the averaged model is expressed by state-space matrices such as A and B . Then a small-signal perturbation in the form of a small step change is applied to one of the duty cycles. Figure 3.9 (b) shows that the averaged model correctly approximates the battery voltage and output inductor current for battery-regulation mode.



(a)



(b)

Fig 3. 9: (a) Model comparison due to duty cycle step, (b) Averaged model and circuit model comparison for Battery-regulation Mode.

The feedback control loops of OVR and BVR are then designed based on the state space models.

Using the model, transfer functions for output and battery voltage to different duty-cycle values

can be extracted according to small signal diagram of Figure 3.10. For example, $G(s)(4,1)$ represents the 4th state variable V_o and the 1st control variable d_1 , thus equals to open loop transfer function of V_o / d_1 . So the row number denotes the sequence of state variable, and column number denotes that of control input. The values such as g_{11} and g_{12} are not expressed because the symbolic derivation of these transfer functions is fairly tedious. Alternatively, a computer software like MATLAB can be used to calculate the desired transfer functions and then plot out the bode plots for analysis in the frequency domain.

$$\begin{aligned}
 G(s) &= (s \cdot I - A)^{-1} \cdot B, \\
 v_o / d_1 &= g_{11} = G(s)(4,1), \quad v_b / d_1 = g_{21} = G(s)(1,1), \\
 v_o / d_2 &= g_{12} = G(s)(4,2), \quad v_b / d_2 = g_{22} = G(s)(1,2)
 \end{aligned}
 \tag{Eq. 3.16}$$

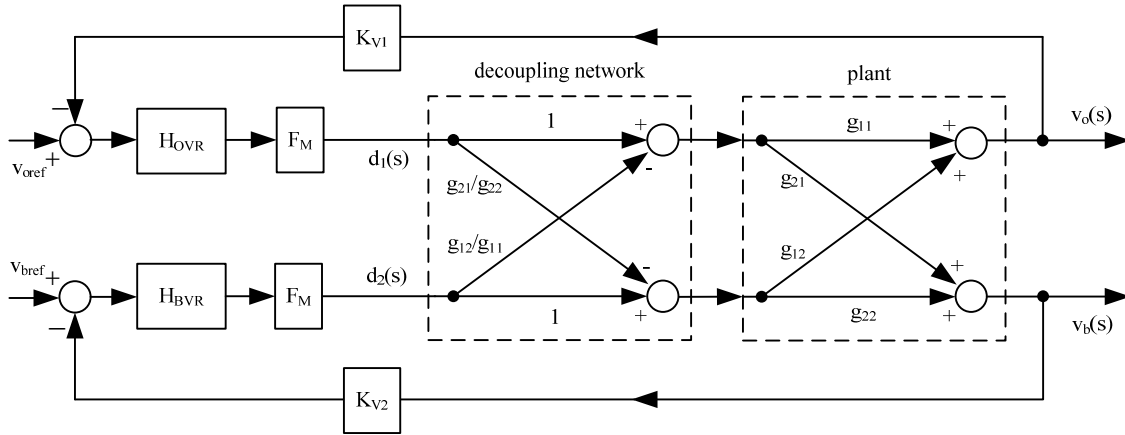


Fig 3. 10: Small signal model of Battery-regulation Mode, control inputs and outputs are decoupled to enable separate controller design. V_{oref} and V_{bref} are the references for output voltage and battery voltage, respectively. H_{OVR} and H_{BVR} are the compensators need to be designed.

In Figure 3.10, PWM modulator gain F_M is calculated using the following equation,

$$F_M = 2^M \cdot f_s / f_{PWMclock} \quad Eq. 3.17$$

Where PWMclock is the clock frequency of PWM counter, f_s is the switching frequency, and M is chosen to allow the logical value in the compare register of the PWM to be between 0 and 1.

The gains K_{V1} and K_{V2} actually take into account both sensing gain and Analog to Digital conversion gain, the latter is dependent on the resolution of Analog to Digital converter.

As mentioned earlier, it is difficult to design close loop compensators for each control loop without proper decoupling method. Therefore a decoupling network as in Figure 8 is introduced so that the control loops can be designed independently with different bandwidth requirement. Since output port voltage regulation requirement is the most stringent of the three and battery characteristics are relatively slower, the BVR loop is designed to have a one decade lower bandwidth than that of OVR. The derivation of decoupling network G^* is described as follows. The state vector matrix X can be written as $X = G \cdot U^*$, where U^* is the modified input vector made up of duty cycles U , $U^* = G^* \cdot U$. Therefore, $X = G \cdot G^* \cdot U$. According to modern control theory, our goal is to make $G \cdot G^*$ a diagonal matrix to allow one control input to determine one output independently. So based on $G^* = X \cdot U^{-1} \cdot G^{-1}$, G^* can be derived and simplified as

$$G^* = \begin{bmatrix} 1 & -g_{12} / g_{11} \\ -g_{21} / g_{22} & 1 \end{bmatrix} \quad Eq. 3.18$$

Since g_{11} and g_{21} are already known, the OVR controller can then be designed with the following equation:

$$v_o(s)/d_1(s) = g_{11} - g_{12} \cdot g_{21} / g_{22} \quad \text{Eq. 3.19}$$

Similarly, the BVR loop design utilizes the BVR loop equation:

$$v_b(s)/d_2(s) = g_{22} - g_{12} \cdot g_{21} / g_{11} \quad \text{Eq. 3.20}$$

With the open loop control objects of $V_o(s)/d_1(s)$ and $V_b(s)/d_2(s)$ available, now it is possible to explore the close loop compensators design. In order to design OVR loop compensator H_{OVR} so that a stable and high bandwidth output loop gain can be obtained, the open bode plot of OVR loop before compensation has been plotted in Figure 3.11(a). The bode shape implies that it has two main poles at around $L_o C_o$ resonance, which causes a -40dB/decade slope. So the design objective is to boost up the low frequency gain to minimize steady state error and make it pass 0dB line at -20dB/decade slope while maintaining a sufficient phase margin. A tradition PI controller will be able to handle this, but if two poles are close to cause sharp phase drop as in this case, a PID controller is recommended to boost up the phase. After compensation, the crossover frequency for the OVR loop is set at 4.1 kHz with a phase margin of 78 degrees. H_{OVR} takes the following form,

$$H_{OVR} = 80 \cdot (s/2\pi \cdot 400 + 1) \cdot (s/2\pi \cdot 800 + 1) / s / (s/2\pi \cdot 4000 + 1) / (s/2\pi \cdot 4000 + 1) \quad \text{Eq. 3.21}$$

For the BVR loop as shown in Figure 3.11(b), the open loop bode also shows a two main pole feature which is easy to compensate, but in order to comply with the bandwidth assumption which is one decade lower than OVR loop, a low gain PI controller is adopted to deliberately

shape it to cross 0dB line at the desired frequency range, and the pole will be placed in front of zero to force a sharp drop of gain curve, but it should be noted that phase margin should be sufficiently large to allow this kind of zero pole placement. If one set of zero and pole is not enough, two sets of zero and pole (PID controller) may be utilized. The crossover frequency of the BVR loop is set at 390 Hz, and phase margin of BVR is set at 88 degrees. The compensator of H_{BVR} used is as follows,

$$H_{BVR} = 0.7 \cdot (s / 2\pi \cdot 1000 + 1) \cdot (s / 2\pi \cdot 1000 + 1) / s / (s / 2\pi \cdot 200 + 1) / (s / 2\pi \cdot 300 + 1) \quad \text{Eq. 3.22}$$

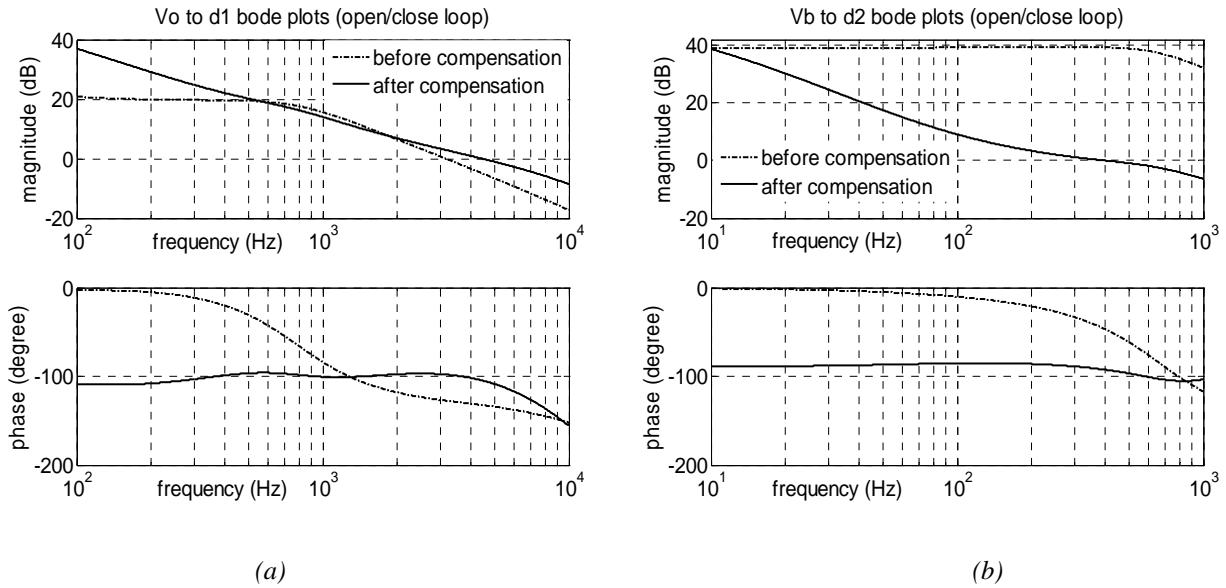


Fig 3. 11: Simulated bode plots for Battery-regulation Mode, (a) $V_o(s)/d_1(s)$; (b) $V_b(s)/d_2(s)$.

Dashed line denotes open loop plant transfer function before applying the compensator, solid line denotes close loop transfer function after applying the compensator. BVR loop bandwidth is set to be one tenth of that of OVR.

3.3.4.2 Three-port Converter Modeling during Battery-Balanced Mode

The same method is followed for battery-balanced mode. In this mode, the input port voltage V_{C2} is considered as a state variable instead of the battery port voltage V_{C1} . Averaged model is derived by state-space representation. The state matrix X contains the four state variables V_{C2} , i_{Lm} , i_{Lo} , and V_o , and the input matrix U remains the two control variables d_1 and d_2 . The A and B matrices take the following form:

$$A = \begin{bmatrix} -\frac{1}{R_s C_2} & -\frac{D_2}{C_2} & -\frac{n \cdot D_2}{C_2} & 0 \\ \frac{D_2}{L_m} & 0 & 0 & 0 \\ \frac{n \cdot D_2}{L_o} & 0 & 0 & -\frac{1}{L_o} \\ 0 & 0 & \frac{1}{C_o} & -\frac{1}{R \cdot C_o} \end{bmatrix}, \quad X = \begin{bmatrix} \hat{v}_{C2} \\ \hat{i}_{Lm} \\ \hat{i}_{Lo} \\ \hat{v}_o \end{bmatrix}$$

$$B = \begin{bmatrix} 0 & -\frac{1}{C_2} \cdot \left(I_{Lm} + \frac{n \cdot V_o}{R} \right) \\ -\frac{V_b}{L_m} & \frac{D_1 \cdot V_b}{D_2 \cdot L_m} \\ \frac{n \cdot V_b}{L_o} & \frac{n \cdot D_1 \cdot V_b}{D_2 \cdot L_o} \\ 0 & 0 \end{bmatrix}, \quad U = \begin{bmatrix} d1 \\ d2 \end{bmatrix} \quad \text{Eq. 3.23}$$

Again, it can be seen from Figure 3.12 that the averaged model correctly approximates the input voltage and output current according to the simulation. Since matrix A and B is derived, transfer functions for output and input voltage to duty cycle values can be extracted from the small signal model as shown in Figure 3.13.

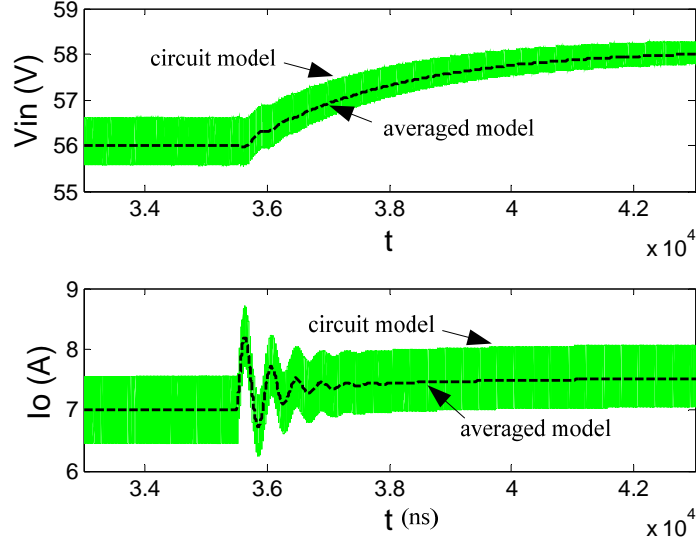


Fig 3. 12: Averaged model and circuit model comparison for Battery-balanced Mode

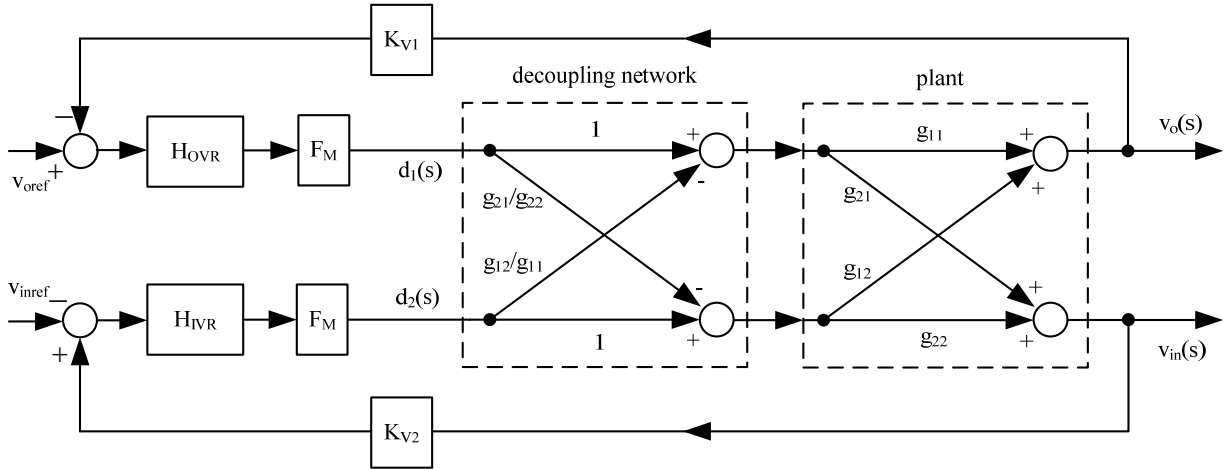


Fig 3. 13: Small signal model of Battery-balanced Mode, control inputs and outputs are decoupled to enable separate controller design. V_{oref} and V_{inref} are the references for output voltage and input voltage, respectively. H_{OVR} and H_{IVR} are the compensators need to be designed.

The same decoupling network is adopted here as the Battery-regulation Mode. In fact, the design of OVR is exactly the same, because no matter in which mode, the transfer function of V_o / d_1 should be the same even though different approaches are applied, therefore bode plot of V_o / d_1 before and after compensation in this mode should be the same as the Battery-regulation Mode.

Then according to

$$v_{in}(s) / d_2(s) = g_{22} - g_{12} \cdot g_{21} / g_{11} \quad Eq. 3.24$$

The $V_{in}(s) / d_2(s)$ bode plot before compensation is plotted in Figure 3.14, which has high bandwidth and 100 degrees of phase margin. IVR compensator H_{IVR} is then designed to enforce relatively low control loop bandwidth with some phase drop. Therefore a PI controller with extremely low gain and one set of zero and pole is adopted to achieve this design goal. The bandwidth of IVR loop is designed at 500 Hz, which is about one decade lower than OVR bandwidth. The phase margin is set at 61 degrees in this case.

$$H_{IVR} = 0.08 \cdot (s / 2\pi \cdot 10 + 1) / s / (s / 2\pi \cdot 200 + 1) \quad Eq. 3.25$$

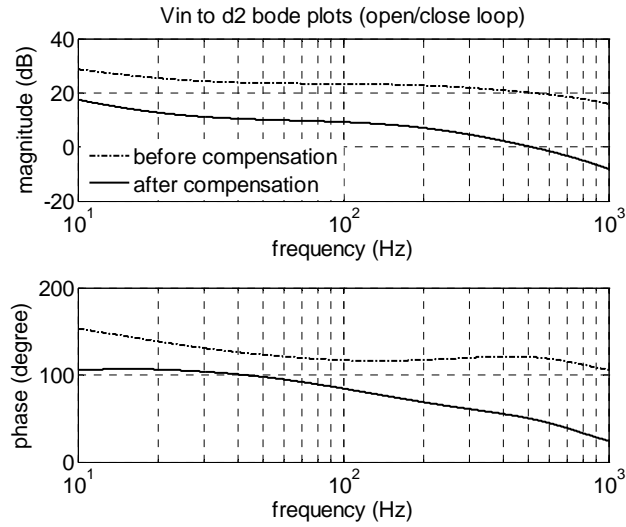


Fig 3. 14: Simulated bode plots of $V_{in}(s)/d_2(s)$. Dashed line denotes open loop plant transfer function before applying the compensator, solid line denotes close loop transfer function after applying the compensator.

3.4. Experimental Results

The mode transition and control structure for both operational modes are tested through a 200 W prototype as illustrated in Figure 3.15. Power stage's input port, battery port and output port are marked as in the prototype photo. It consists of two boards, power stage board and controller board. All feed back control loops' compensators are implemented by a direct digital design method [32].

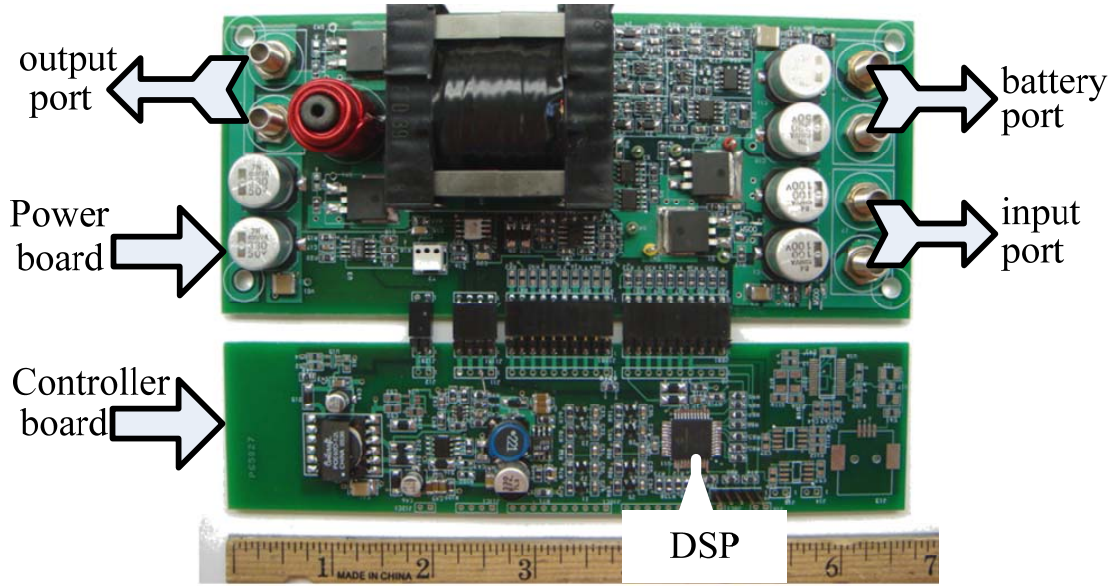


Fig 3. 15: Prototype photo of three-port converter which consists of one controller board and one power board.

The values of circuit parameters used in the simulation and experimental circuit are listed in the following table:

Table 3.26 Values of Circuit Parameters

output inductor	L_o	65 μ H	output voltage	V_o	28V
magnetizing inductor	L_m	45 μ H	input voltage	$V_{in} (V_{C2})$	60 V
output filter capacitor	C_o	680 μ F	battery voltage	$V_b (V_{C1})$	28 V
battery port filter capacitor	C_l	680 μ F	input port filter capacitor	C_2	210 μ F

Figure 3.16 shows the waveforms when the power is transferred from input port to the output load port, while battery port is chosen to be open. Output inductor current i_{L_o} has four stages, and transformer magnetizing average current I_{pri} is zero, implying no battery power. Figure 3.17

shows the waveforms when the most power is transferred from input port to the battery port. Output inductor current i_{Lo} average represents the load current, which is zero. Therefore, negative i_{Lo} is observed. I_{pri} average value represents the battery current, which is 7A.

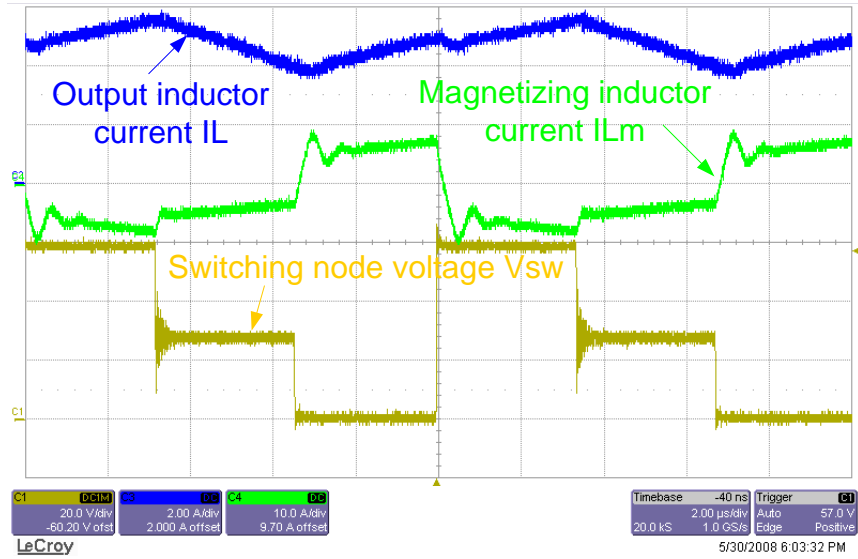


Fig 3. 16: Loading output port when the battery current is zero

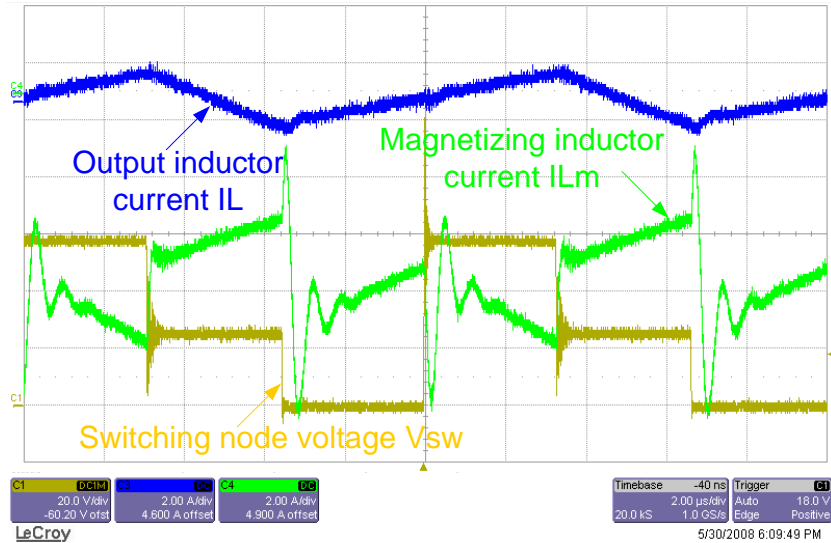


Fig 3. 17: Loading battery port when the output current is zero

Figure 3.18, Figure 3.19 and Figure 3.20 show the gating signal V_{gs} and switching node V_{sw} waveforms of the switches S1, S2 and S3, respectively. The conclusion is that all three main switches can achieve ZVS, because they all turn on after their V_{ds} go to zero.

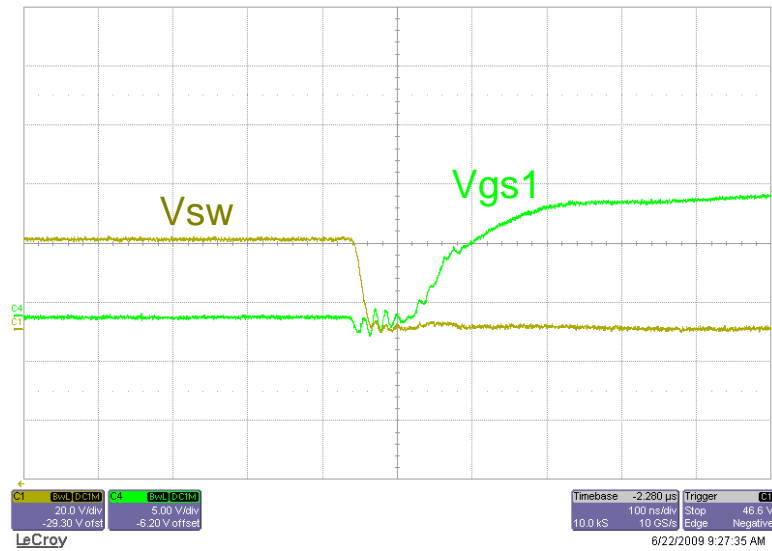


Fig 3. 18: ZVS for S1

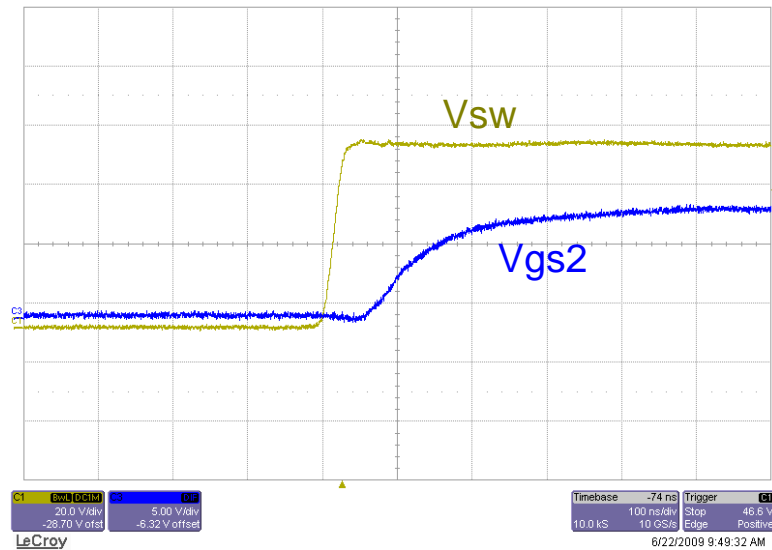


Fig 3. 19: ZVS for S2

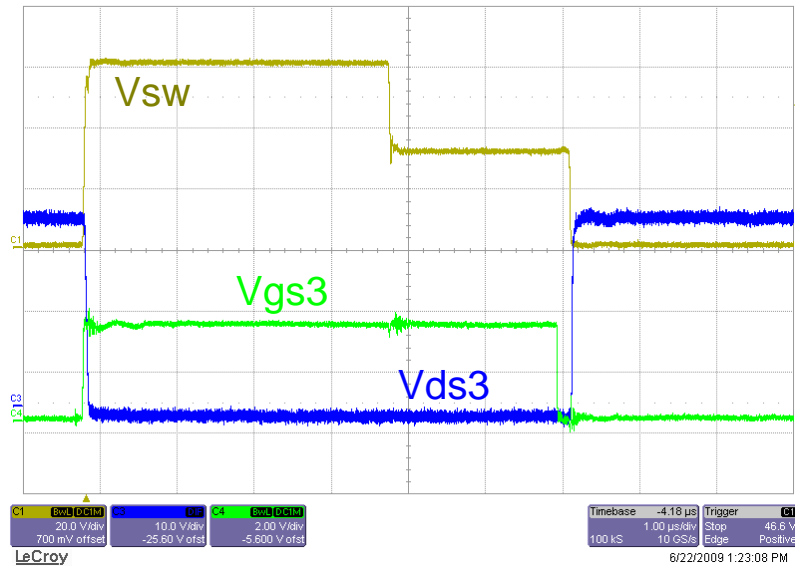


Fig 3. 20: ZVS for S3

Figure 3.21, Figure 3.22 and Figure 3.23 show the efficiency curves when the power is transferred from one port to the other port. The highest efficiency is observed when the power is transferred from solar port to battery port. The reason is that this operation has minimal transformer losses, since the power is exchanged within the primary side.

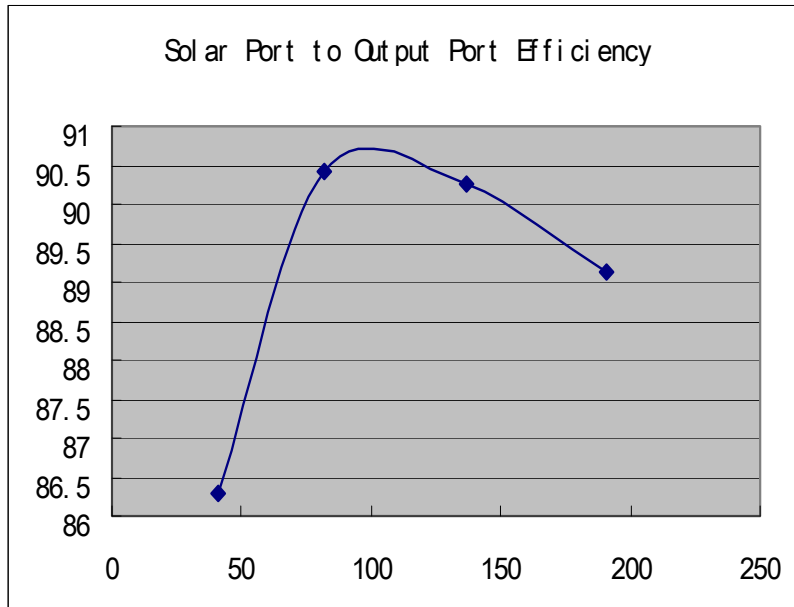


Fig 3. 21: The efficiency when the power is transferred from solar port to output port

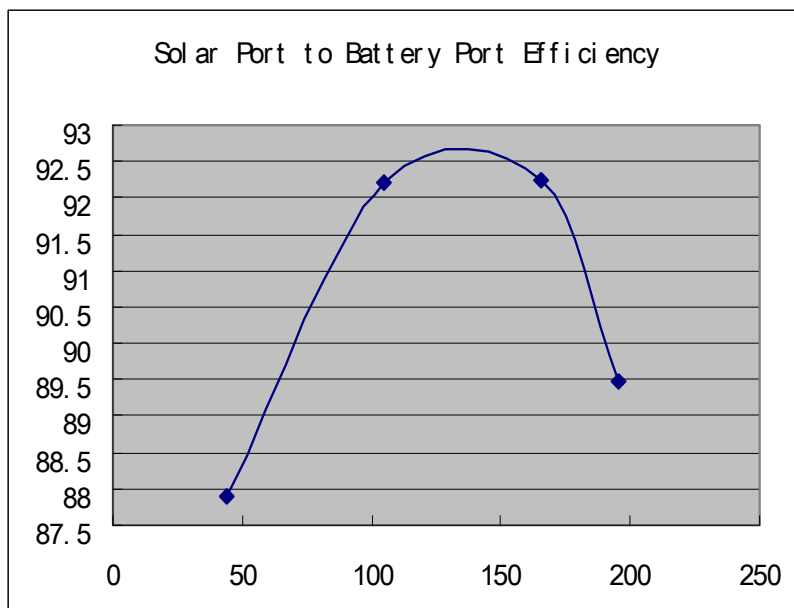


Fig 3. 22: The efficiency when the power is transferred from solar port to battery port

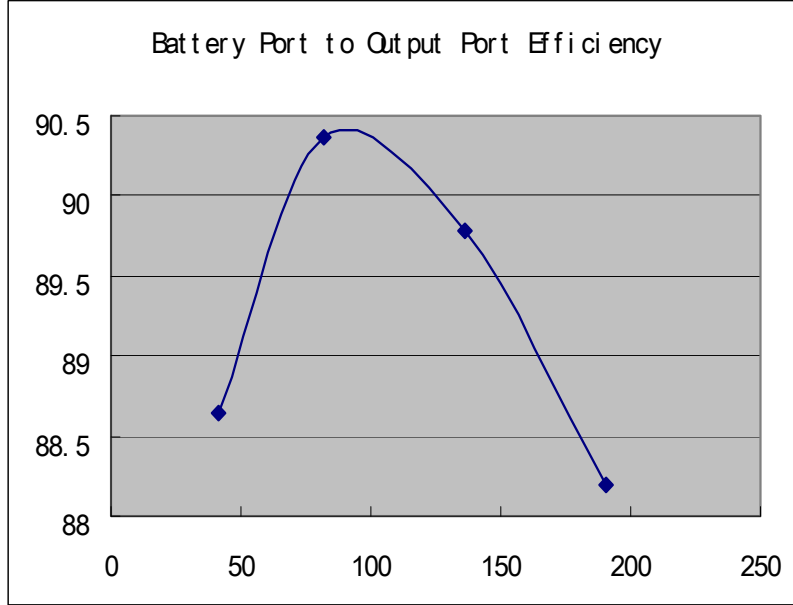
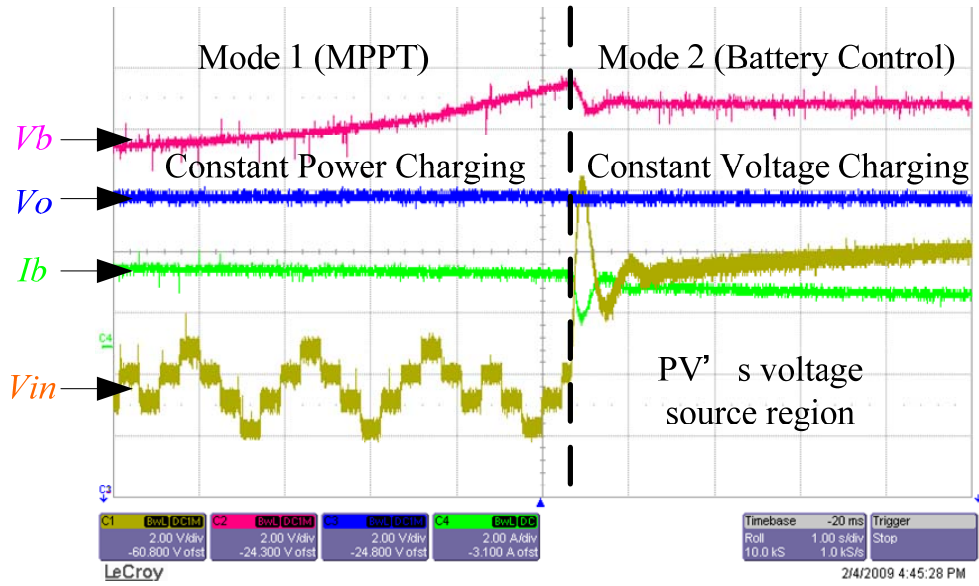


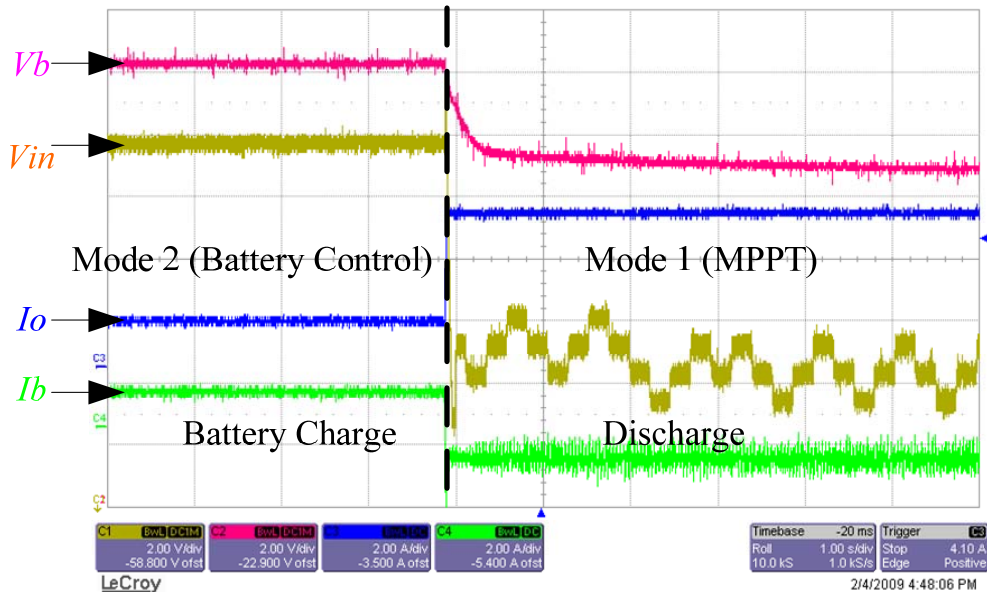
Fig 3. 23: The efficiency when the power is transferred from battery port to output port

Figure 3.24(a) shows mode transition from Battery-balanced Mode (Mode 1) to Battery-regulation Mode (Mode 2) when battery maximum voltage setting of 29 V is reached. Solar panel first works under IVR control with MPPT to maximize solar power, then it is forced to operate in solar panel's voltage source region when IVR loses control and BVR takes control over d_2 , so the input port provides power balance after the transition into battery regulation mode. It can be seen that the transition of the proposed competitive method is smooth and causes no oscillation that is experienced with the sudden transition of duty cycles mentioned in section IV. The battery voltage has 0.5V overshoot, and input voltage has 2.5V overshoot, both are within acceptable range according to specifications.

Figure 3.24(b) gives Mode 2 to Mode 1 transition when load level suddenly increases to force the battery to source instead of sink. Since battery voltage setting can not be met during discharging, d_I will be controlled by IVR since BVR quickly loses control, and solar panel quickly reacts to work under MPPT control so as to harvest maximum available solar power, and battery becomes to provide the power balance in Mode 1.



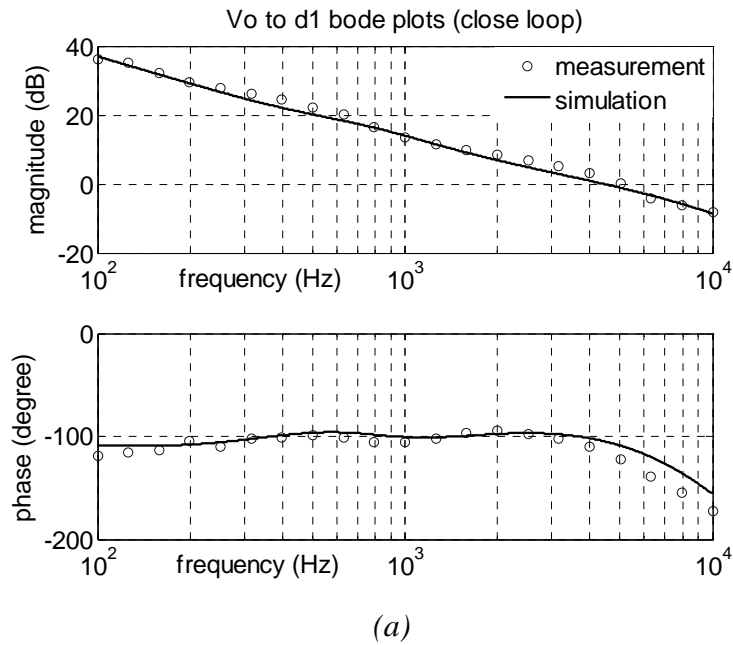
(a)



(b)

Fig 3. 24: Autonomous mode transition, (a) Mode 1 to Mode 2; (b) Mode 2 to Mode 1

Frequency analyzer is used to verify the control loop design. Close loop bode plots of three control loops are tested respectively as shown in Figure 3.25, and the dotted bode plot measurement agree with the previous simulation in the form of solid lines.



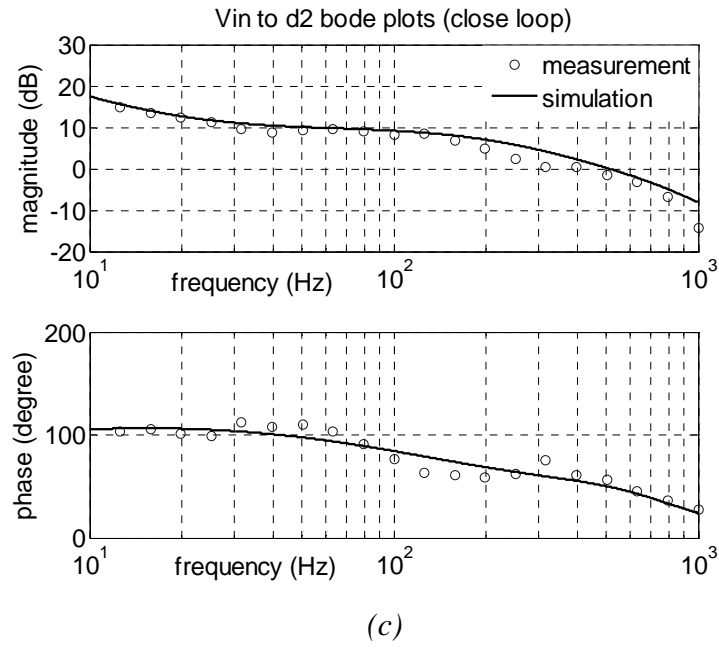
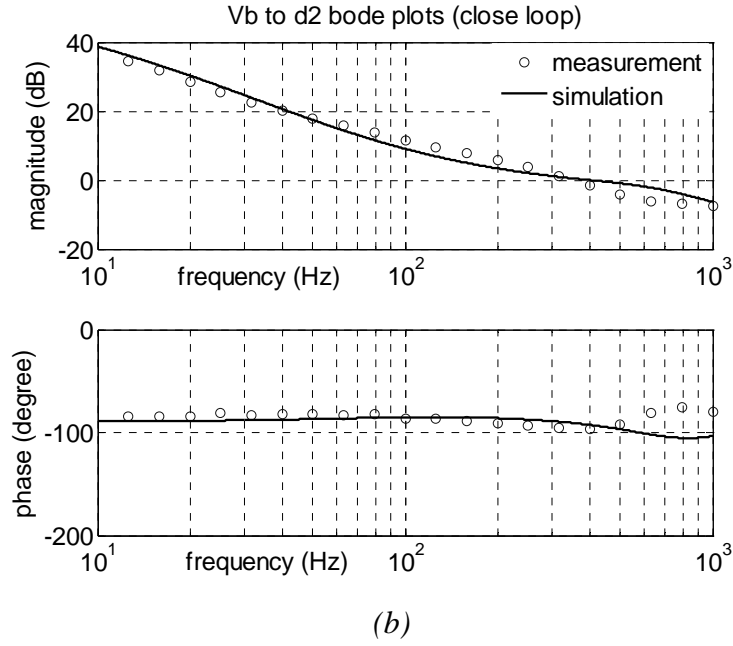
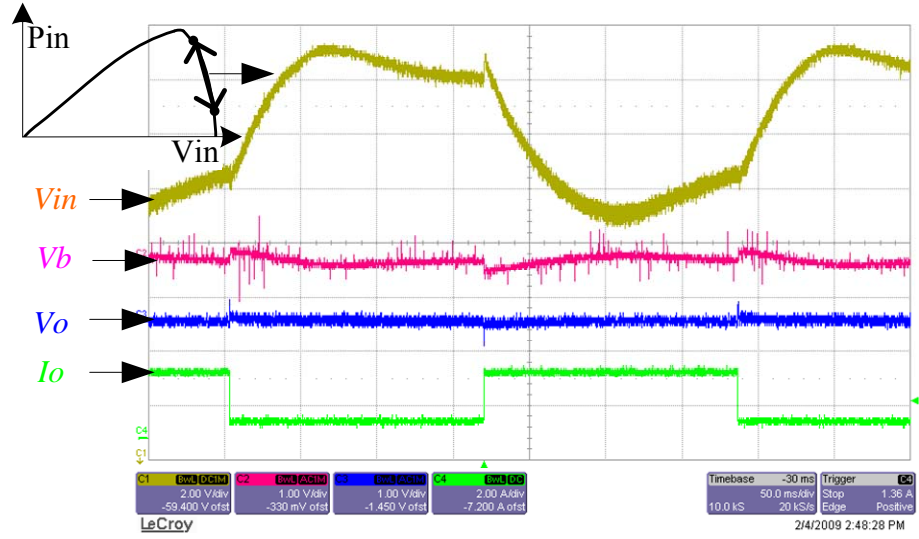


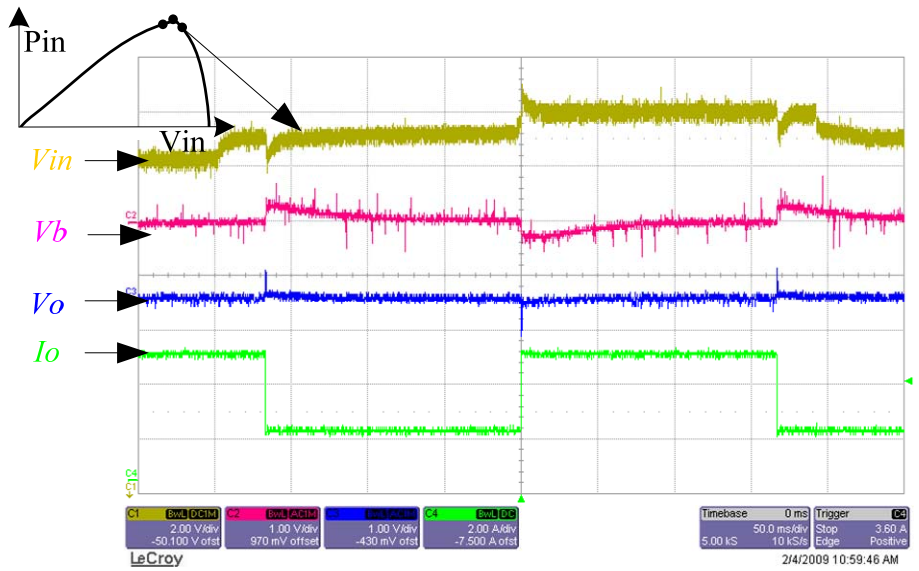
Fig 3. 25: Simulated and measured bode plots, (a) V_o / d_1 , (b) V_b / d_2 , (c) V_{in} / d_2

Figure 3.26(a) shows the input voltage, battery voltage and output voltage response to a load transient between 1A and 3A in Battery-regulation Mode. Output voltage transient response of

500us settling time is much faster than battery voltage settling time of 40ms because OVR bandwidth is ten times larger than that of BVR. Input voltage changes according to load level changes because input port provides power balance. Figure 3.26(b) demonstrates the system transient response in Battery-balanced Mode when MPPT is active. The load step is from 1A to 5A. Input voltage response to load transient of 20ms settling time is much slower than output voltage settling time of 500us because IVR crossover frequency is set at one tenth of that of OVR. Input voltage remains uninterrupted at around MPP even during load changes, which is the unique feature of three-port converters, because MPPT and load regulation can not be achieved simultaneously by conventional two-port converter.



(a)



(b)

Fig 3. 26: (a) Battery-regulation Mode load step response, (b) Battery-balanced Mode load step response.

Figure 3.27 presents the typical experimental results of three different ports' voltage and current imitating for satellite's one orbit cycle which includes four orbiting stages to verify the control design for space applications. The output voltage is regulated all the time while output load level is commanded to change from 3A to 0.5A deliberately to allow for mode transitions. As mentioned in section II, in Stage I of satellite cycling, no solar power is available due to eclipse, therefore input current I_{in} is zero and battery discharges to supply for full load. In Stage II of initial insolation, solar panel operates in MPPT to maximize power input, but it is still not enough to support full load, so the battery still discharges but with less discharging current, while I_{in} is 1.3A. In Stage III, solar insolation level increases and solar power at this point not only supplies for full load but also has extra to charge the battery, meanwhile battery current I_b becomes positive. At the 30 minute point, load requirement is suddenly reduced from 3A to 0.5A. As a result, the power deficit goes to charge battery and triggers battery current regulation to prevent over-current, so BCR takes control over d_2 from previous IVR commanding, and MPPT is disabled accordingly. During this period (30-34min), because input power and output power is fixed, battery power is fixed as well, more specifically, battery current reduces due to increase of battery voltage. So it eventually goes out of current protection and BCR loses control when IVR takes control back over d_2 again to operate in MPPT. Then battery voltage setting is quickly reached, and BVR wins control over d_2 and thus battery voltage is regulated, meanwhile I_b drops gradually. When satellite enters into eclipse again, the system will go through another same cycling period.

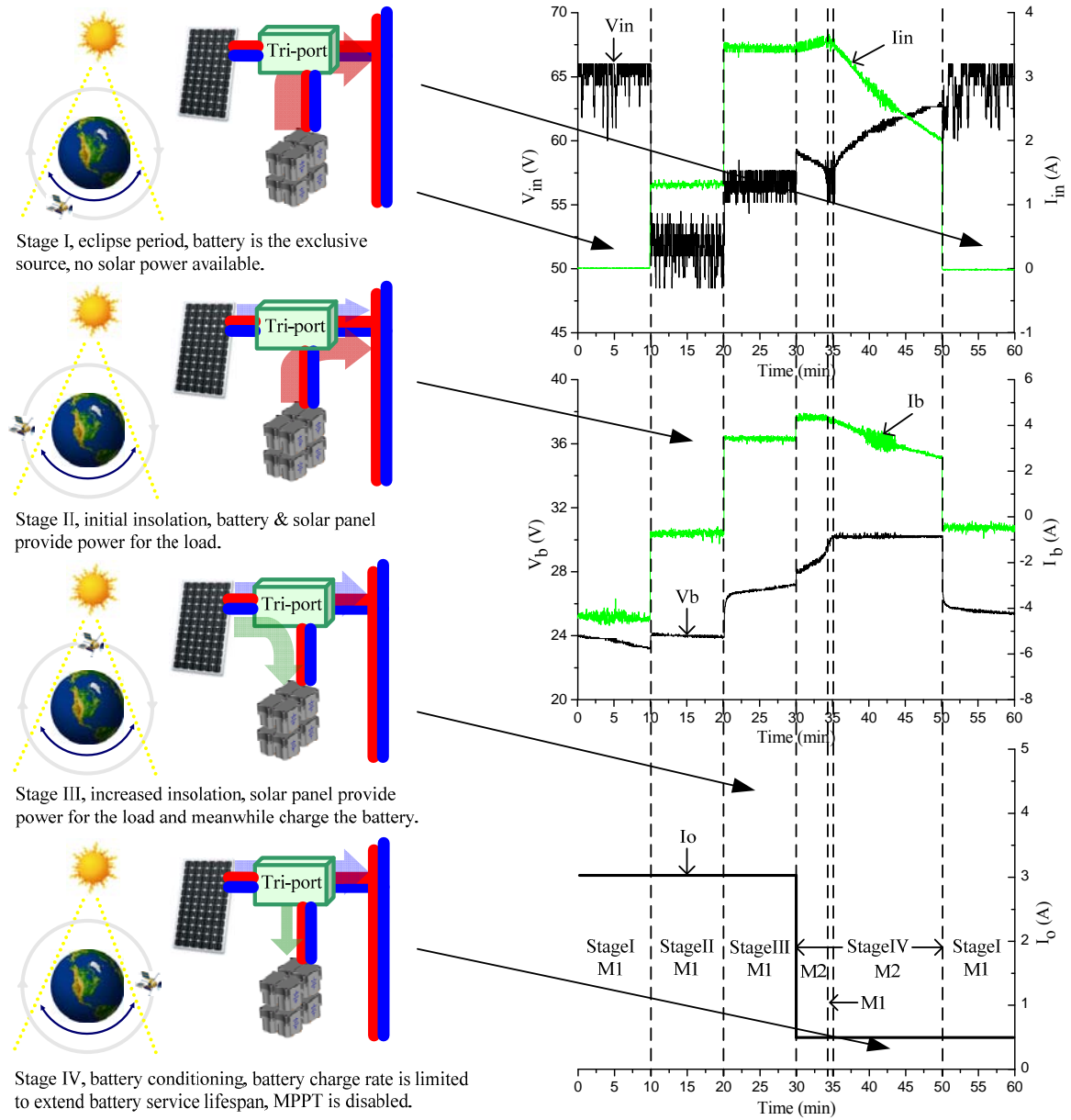


Fig 3. 27: Different mode operations based on available solar power, battery state of charge and load profile, left column shows four stages in satellite's one orbit cycle; for the right column, top one shows input solar panel voltage and current, middle one represents battery voltage and current, bottom one shows output port load level while its voltage is maintaining regulated all the time.

CHAPTER 4: PARALLEL OPERATION OF MULTIPLE THREE-PORT CONVERTERS

4.1. General Description

A desirable feature of a parallel system is that individual converters share the current equally and stably. Specifically, for paralleled three-port converters, current sharing (CS) control for two of three ports is required. In other words, traditional one port CS control is not enough for three-port converters because unequal current distribution in the other two ports may occur due to power stage non-identities. Moreover, how to maintain system stability while achieving good transient CS response is a key issue since there are many interacting control loops due to power train integration with three power ports. In this dissertation, a dual loop CS control structure is identified to be very suitable for paralleled multi-port converters, due to the convenient decoupling assumption between voltage loop and CS loop. A hybrid CS structure combining both active and passive CS methods is proposed to achieve good transient CS performance without requiring the CS bus among different converter channels.

4.2. Current Sharing for Two Paralleled Converters

A large body of work has been done in the past on the paralleled converters' CS issue [50]-[59], but most of the researches have focused on traditional two-port converters. Since the three-port converter is a relatively new concept and has advantages such as multiple functionalities, low mass and high efficiency, etc; its CS issue is also worth studying. Normally the multi-port

converter is a high order system with multiple interacting feedback control loops. Therefore it is already complicated to design controllers for the integrated converter with abundance of control loops, and the additional two CS control loops for the paralleled three-port converters will further challenge the steady state and dynamic performance, therefore proper decoupling between CS loop and voltage loop is necessary to prevent control loop interaction and the dynamic analysis is desired to help judge overall system stability.

As shown in Figure 4.1, the integrated system contains two paralleled three-port converters, in which two of three ports will be controlled simultaneously with CS control, and the two ports being regulated simultaneously can be either the output port with the battery port, or the output port with the input port.

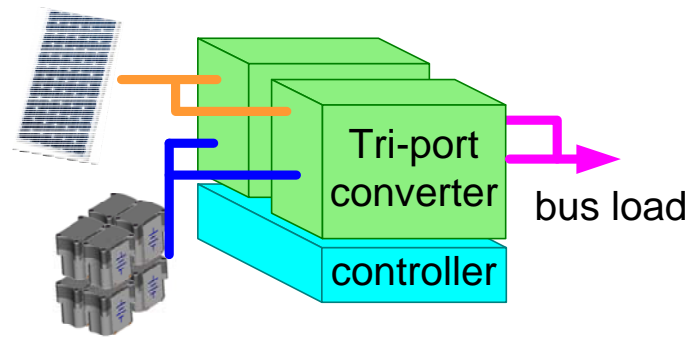


Fig.4. 1: Paralleled three-port converter system interfacing solar panel, battery pack and bus.

4.2.1. Output Port Current Sharing for Two Paralleled Converters

As in Figure 4.2, the proposed active CS method achieves uniform current distribution with tight voltage regulation. More specifically, democratic (also referred to as autonomous) maximum

current sharing that is constructed by the paralleled voltage controller and the CS controller is adopted, which is referred as dual loop CS. The democratic current reference is utilized due to the redundancy requirement to achieve fault-tolerance.

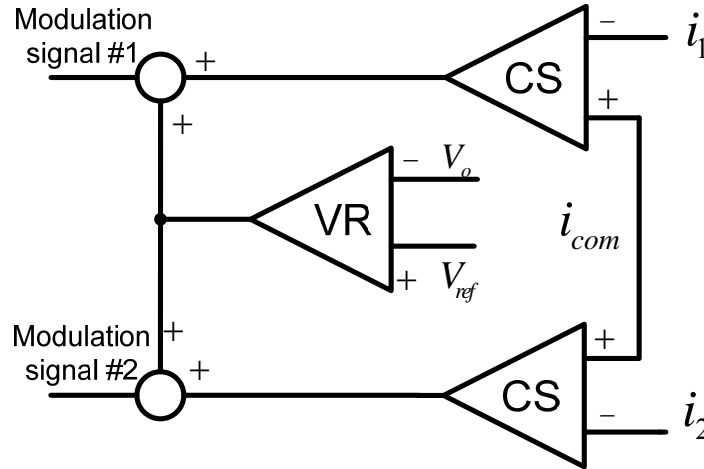


Fig.4. 2: Dual loop CS control structure

Instead of the dual loop CS control structure, the other two conventional types of CS control structures are: (1) Outer voltage regulation and inner CS loops as shown in Figure 4.3; (2) Inner voltage regulation and outer CS loops as shown in Figure 4.4. Outer voltage regulation and inner CS loop structure utilizes the output of voltage compensator as current command, and is mostly used based on current mode control, so it is unsuitable for this application which requires voltage mode control to maintain a regulated bus voltage. For the inner voltage regulation and outer CS loop structure, the CS compensator design must consider the voltage compensator design since the later one is a part of the overall CS loop. In other words, the two loops are closely coupled together which therefore will complicate the control loop design. To sum up, the outer loop is always limited by inner loop in terms of control loop bandwidth; as a result it is difficult to apply

decoupling method. For three-port converters having various interacting control loops, a control structure allowing separate voltage loop and current loop controller design is highly demanded since it will keep design process simple and clear, which is the main reason that dual loop CS structure is adopted.

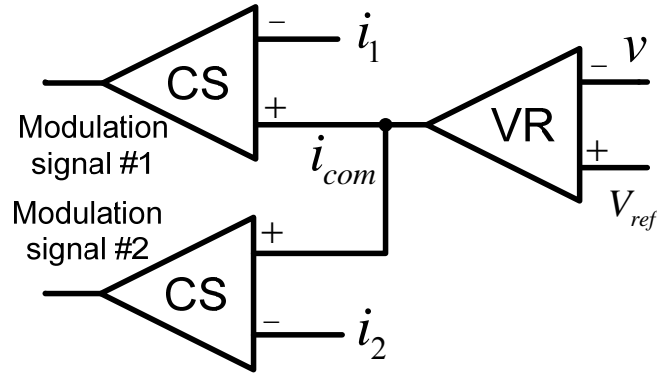


Fig.4. 3: Outer voltage loop and inner CS loop control structure

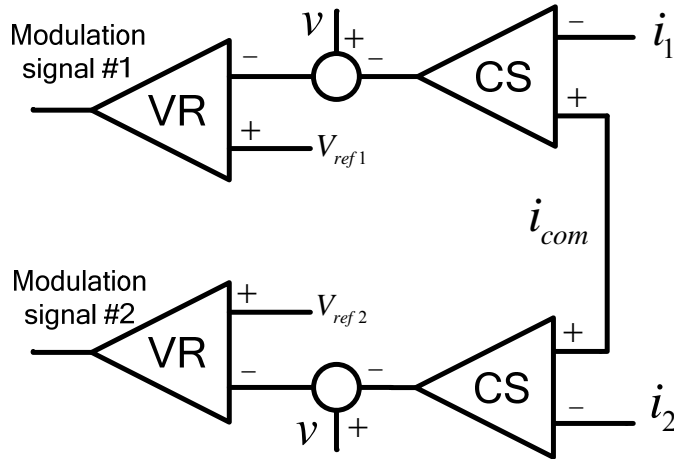


Fig.4. 4: Inner voltage loop and outer CS loop control structure

Although many efforts have been made to analyze the inner-outer CS control structure [49]-[53], few literatures [54], [55] have been reported on this kind of dual loop CS structure. Above all,

special design considerations for three-port converters are required because of integrated power train issue.

The advantage of paralleled CS structure is that a convenient decoupling assumption can be made in the abundant control loops for designing such complicated systems. Small signal analysis of the proposed paralleled CS structure shows that the CS loop and voltage loop are not heavily coupled with each other even with large non-identities in power stages, which allows convenient decoupling and further simplifies the compensator design.

4.2.2. Modeling of Dual-loop Current Sharing Structure

The output CS loop design of the paralleled converters with democratic maximum CS control is composed of the following steps: 1) individual converter is designed stably with OVR closed loop operation; 2) CS control loop is added and overall output control loop analysis is applied to ensure overall output port stability. It should be mentioned that democratic CS and dedicated master CS basically produce the same small signal model. Therefore without loss of generality, module#1 is designated as master and thus module #2 is assigned as a slaver for simplicity.

Figure 4.5 gives the small signal block diagram for output control loops (VR and CS) together with the decoupled converter model obtained in Chapter 3. H_{VR} denotes voltage loop compensator while H_{CS} denotes CS loop compensator which needs to be designed.

When two paralleled modules are considered, voltage loop gain with CS control loops open (outputs of both CS loops are zero) can be obtained as follows:

$$T_v = v_y / v_x = H_{VR} \cdot (G_{vd1} + G_{vd2}) \quad \text{Eq. 4.1}$$

Obviously, for the master module, CS loop does not affect its duty cycle because CS loop output is saturated at its lower limit, which is zero. On the other hand, CS loop output will affect duty cycle of slaver module since it is not zero, and when considering voltage loop to be open, its CS loop gain can be expressed as:

$$T_i = H_{CS} \cdot G_{id2} \quad \text{Eq. 4.2}$$

T_i represents CS loop gain which determines CS dynamic performance and can help to derive the overall output loop gain T_{sys} as follows:

$$T_{sys} = v_y / v_x = T_v + H_{VR} \cdot (G_{id1} - G_{id2}) \cdot H_{CS} \cdot G_{vd2} / (1 + T_i) \quad \text{Eq. 4.3}$$

Equation (5) demonstrates when two modules are identical, that is to say, $G_{id1} = G_{id2}$, it only needs to judge OVR loop itself and CS loop has no effect on overall output port stability. In other words, the voltage loop and CS loop are 100% decoupled. However, in practice, there are always some power stage non-identities such as component tolerances and temperature variations and connection asymmetry among converters; otherwise, CS can be achieved naturally since converters are exactly the same and are connected symmetrically. Since G_{id1} will not be exactly the same as G_{id2} , the question now becomes how T_{sys} will be different with T_v if some

values of power stage parameters are not the same. Since the converter model derived only includes those passive component values (without considering active components like MOSFETs), 30% deviation of output filter inductor L and output filter capacitor C values (both including equivalent series resistances) are assumed. Therefore, to consider the worst case scenario, module #2 is assumed to have 70% L and C values of those of module #1. Then bode plots are calculated and plotted through computer software MATLAB to show the deviation between voltage loop gain T_v and overall system loop gain T_{sys} . CS loop gain T_i is designed to have high bandwidth (1kHz compared with 3kHz for voltage loop) with sufficient phase margins to achieve good CS dynamic response during load transients.

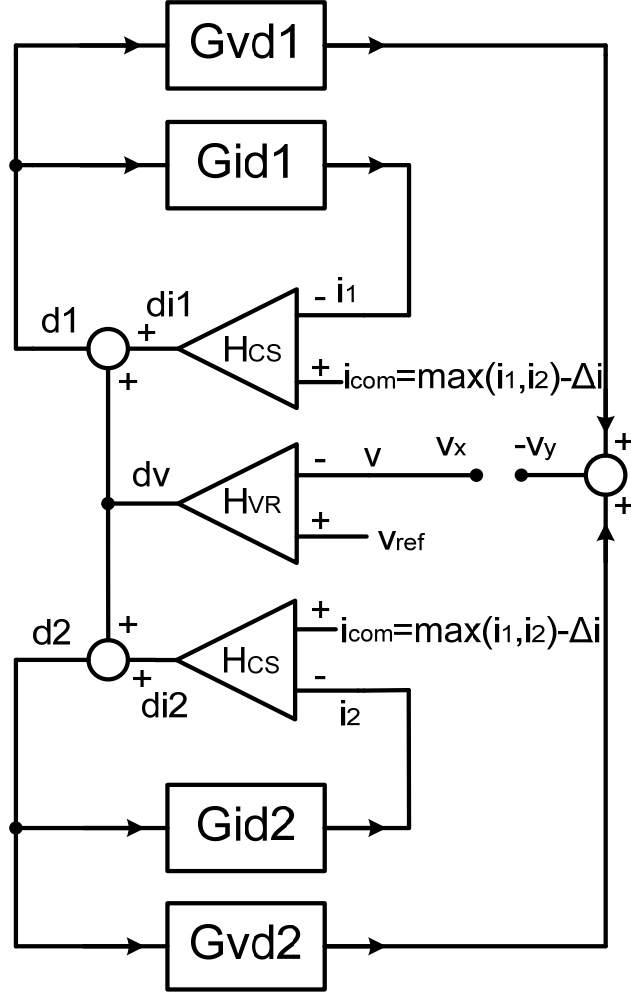


Fig.4. 5: Loop analysis of output port with two paralleled converters, G_{id} and G_{vd} are already obtained from section II (battery port control loop diagram is similar with output port)

Figure 4.6 illustrates that the overall loop gain of T_{sys} almost agrees with the voltage loop gain of T_v even with 30% deviation of passive components considered. This result is desirable because it basically proves that dual loop CS structure's voltage loop and CS loop are not coupled with each other heavily. Therefore, decoupling assumption between voltage loop and CS loop in this CS structure is reasonable. Though CS loop gain of T_{cs} does not affect overall loop gain of T_{sys} , it

decides the CS dynamic performance by itself. Therefore the design of T_{cs} has to achieve enough phase margins in order to meet stability criteria. Figure 4.7 gives another unstable CS loop design expressed as T_{cs}' , it has only 10 degrees of phase margins, therefore will easily cause current instability which is observed in Figure 4.8(b). Since the voltage gain T_v is the same for both designs, the output voltage response is not affected too much in spite of unstable CS loop. Therefore, the time-domain behavior also confirms the decoupling concept.

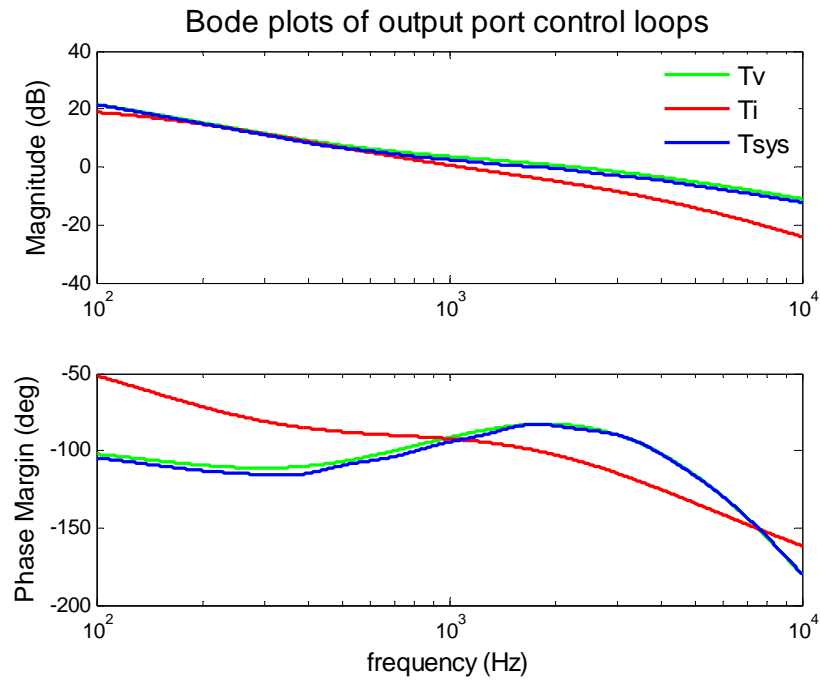


Fig.4. 6: Calculated bode plots of output port control loops

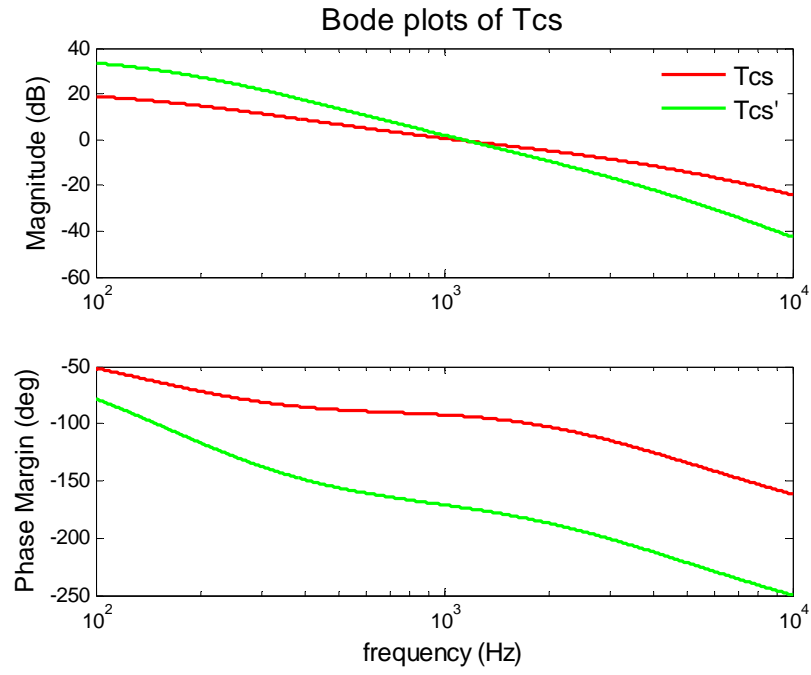
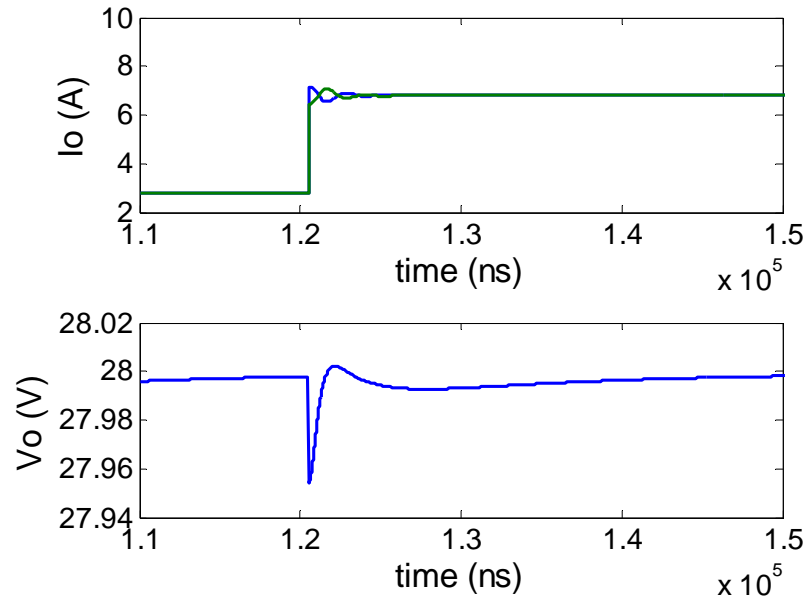
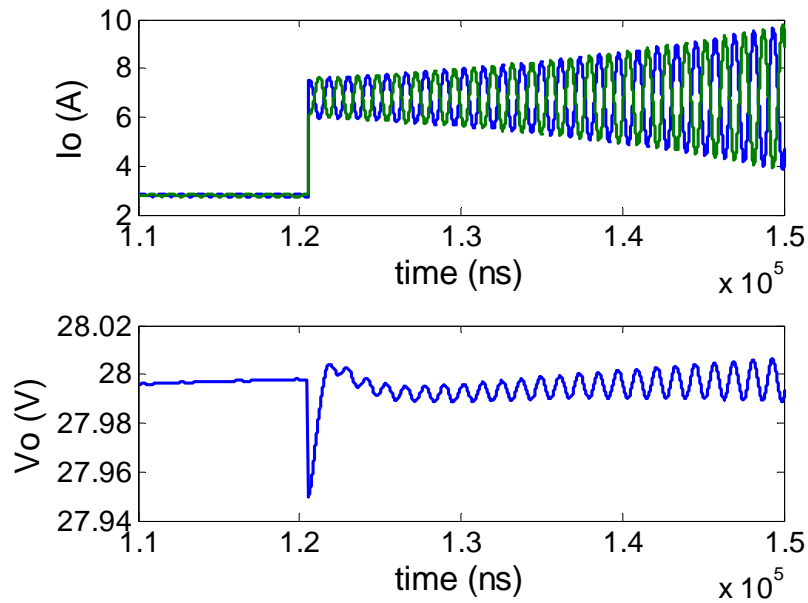


Fig.4. 7: Bode plots of CS loop gain T_{cs} , stable and unstable



(a)



(b)

Fig.4. 8: Transient response to load steps from 40% to 100%, (a) stable CS loop gain T_{cs} ; (b) unstable CS loop gain T_{cs}'

4.2.3. Battery Port Current Sharing for Two Paralleled Converters

Two-Stage Charging delivers power to the battery in two steps as shown in Figure 4.9. In the first step, the battery is charged by maximum available solar power which is the deficit of input and output power, so it can be taken as a constant power charging period, in which battery voltage rises gradually. When the battery upper voltage setting V_{bmax} is met, the converter will switch to regulate its voltage to prevent over-charging, which is the second charging step. But one thing that should be mentioned is that unlike regular constant current battery charging, the battery cannot obtain a constant charging current because of solar power and load changes as shown in Figure 4.10 and Figure 4.11. Figure 4.10 illustrates the MPP moves from A to C during irradiance increase when load is constant, and the available battery energy is the difference of input and output load power. B, C provide increased charging current for battery, while no charging current will be available at A. Figure 4.11 shows the battery power during load changes. A, B provide decreased charging current, while battery discharges at C.

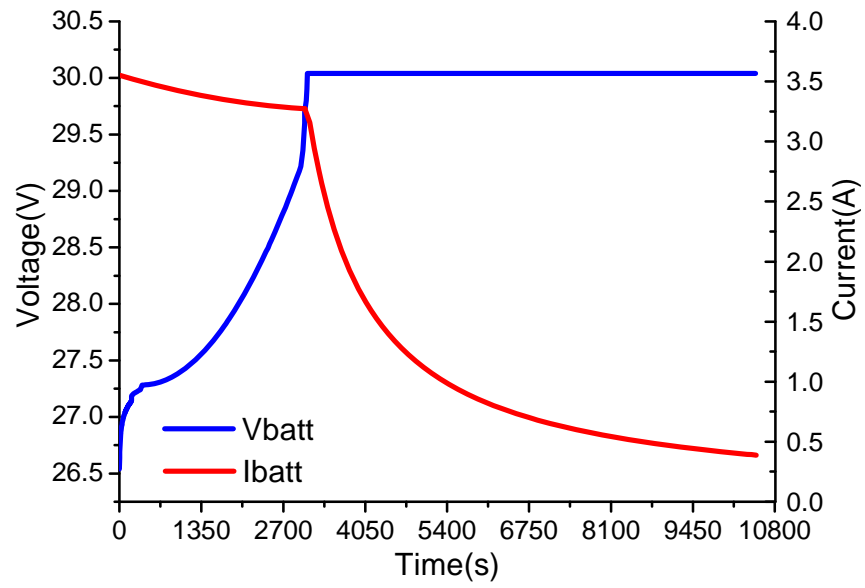


Fig.4. 9: Battery two stage charging profile

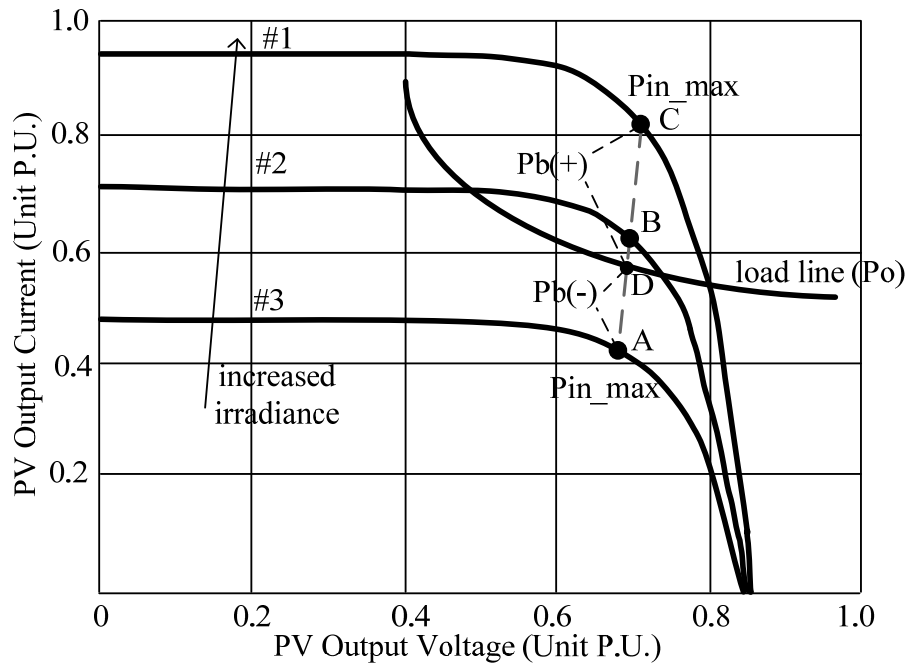


Fig.4. 10: Solar array irradiance changes, then battery charging power changes accordingly

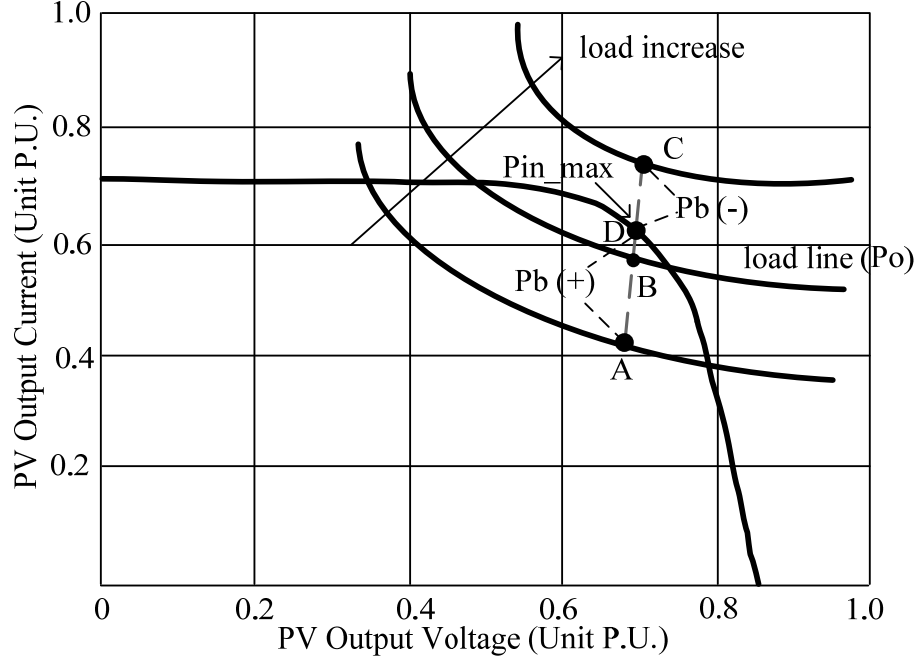


Fig.4. 11: Load level changes, then battery charging power changes accordingly

When the battery ports are connected together, a reliable CS is required to achieve battery current sharing and meanwhile has to perverse the battery charging regulation function. The true redundant active voltage positioning (AVP) droop method is utilized to realize CS for battery port. Unlike AVP concept in voltage regulator modules to improve voltage regulation, AVP method is borrowed here for current sharing control. The design procedure consists of two following steps: 1) stable individual converters are designed by closing both OVR and BVR loops. 2) “droop” is added to each module to obtain CS.

Since in this approach, the droop characteristic is implemented in an open-loop fashion, stability problem is not a concern for the droop CS. But this droop rate design will influence the battery port CS performance.

Fig 4.12 shows the simplified paralleled battery system. R_{d1} and R_{d2} are the “droop” resistors digitally programmed which represents droop rate, V_{b1} and V_{b2} are the no load regulated battery voltage normally with different voltage values. The CS error $\Delta I/I$ is determined by both voltage source values and droop rates. The following discussion demonstrates how to minimize CS error according to droop rate with gain mismatches in practical conditions. Droop design under ideal conditions has already been covered in [3,5], so only design under non-ideal conditions is presented here in this section.

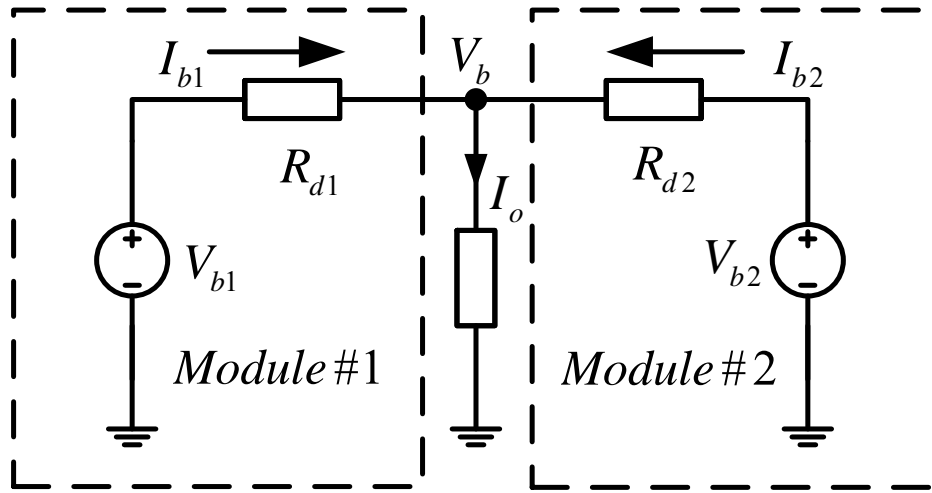


Fig.4. 12: Battery output model with droop resistances

When battery is providing current, the droop equation of the system is characterized by:

$$V_b = V_{b1} - R_{d1} \cdot I_{b1} = V_{b2} - R_{d2} \cdot I_{b2} \quad \text{Eq. 4.4}$$

The droop rate actually includes the information of CS network, ADC, and the programming droop rate. So even though the programming droop rate is the same for both modules, different CS error may occur due to different current sensing gain and ADC gain as shown by Figure 4.13. Figure 4.13(a) is the undesirable condition which gives increased CS error as the load increases. Figure 4.13(b) is acceptable since CS error remains the same value as the load increases. The desirable droop rate setting is that we can achieve the result of Figure 4.13(c) or Figure 4.13(d). The difference is that two modules share equal current at 50% load for (c) or 100% load for (d). Therefore different programming droop rate is suggested to compensate different sensing gain and ADC gain. The design rule is straightforward as indicated by Fig 9 that the one with higher voltage reference should have a larger droop rate.

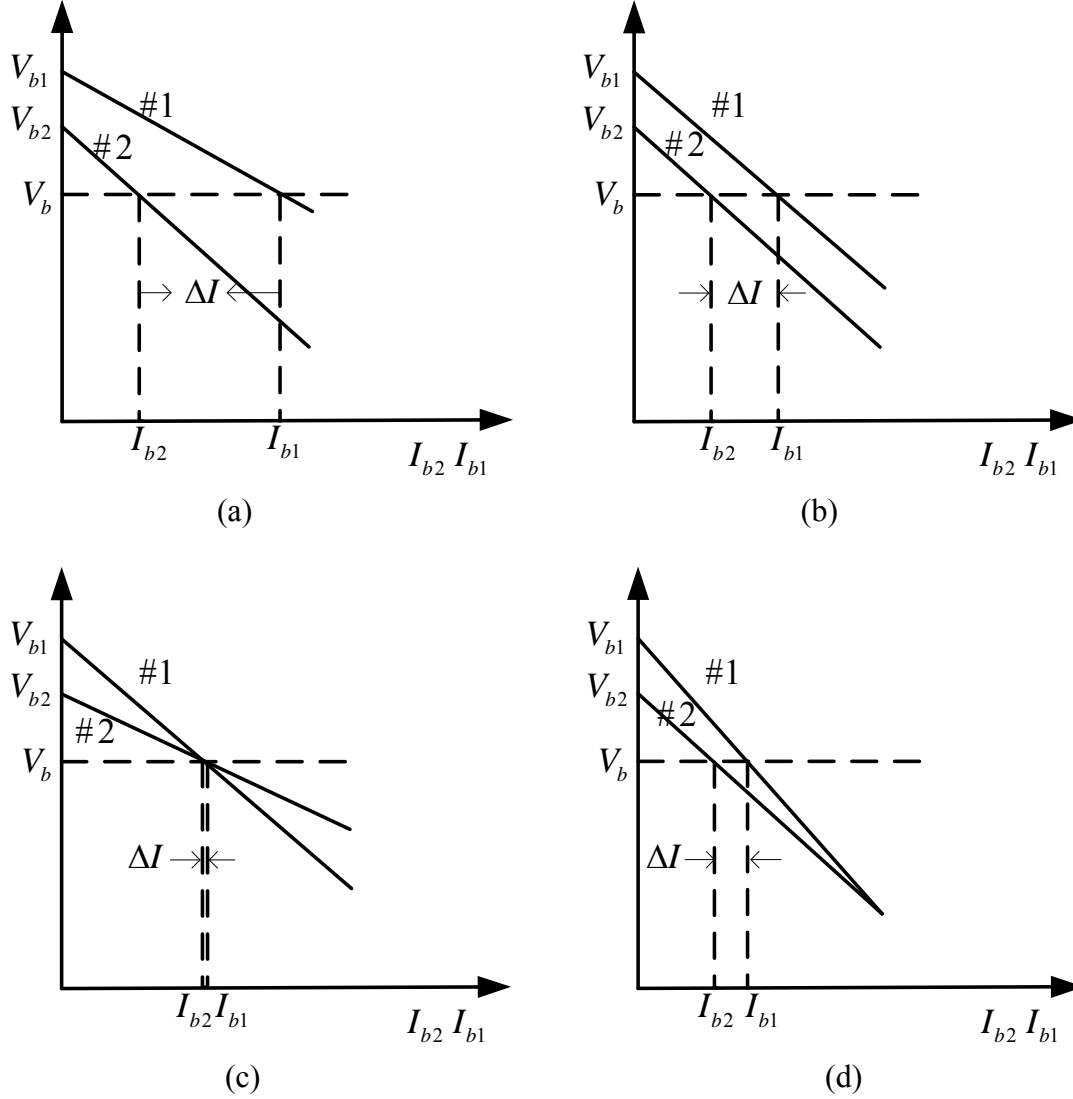


Fig.4. 13: Effect of different droop rate on CS error (a) undesirable (b) acceptable (c) good, zero error at 50% (d) good, zero error at 100%

As in Figure 4.14, with the proposed CS function incorporated, the converter will switch to battery voltage regulation at the point of V_{bmax} minus I_b times R_{droop} , someplace earlier than V_{bmax} .

So the converter achieves CS at the cost of getting charged slightly slower than the regular method. But CS function is critical to such three-port converters; tradeoff has to be made between the passive CS and battery charging.

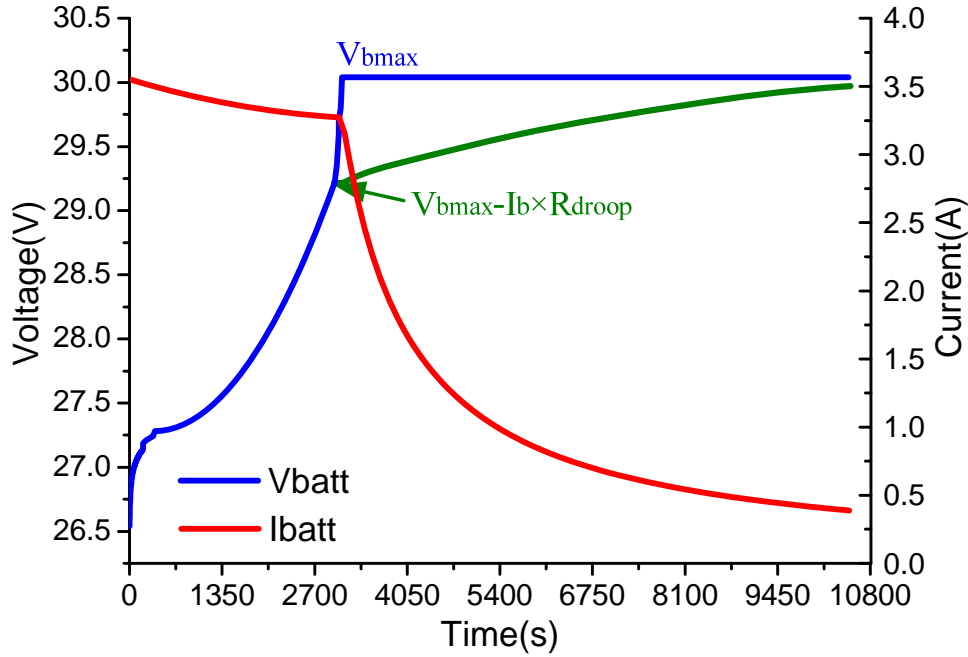


Fig.4. 14: Battery charging algorithm with CS

4.2.4. Input Port Current Sharing for Two Paralleled Converters

With available input voltage & current information of the two converters within one channel, it is possible to incorporate CS function into MPPT algorithm as in Figure 4.15. It should be noted that only intra-channel level CS is required for input port since different channels have different PV sources. The Perturb & Observe MPPT method is used as shown in Fig 4.16. After input voltage reference $V_{ref(k+1)}$ is obtained, it is added to the product of coefficient K and the

individual current measurement to derive modified voltage references. So if input current I_1 is larger than I_2 , V_{ref1} will be greater than V_{ref2} . Since a higher input voltage will bring down its input current, simple current sharing without closed loop control is achieved. Most importantly, this CS is compatible with MPPT algorithm. But it should also be noted that the speed of CS control will be dependent on MPPT controller speed. Due to the slow characteristics of PV, in most conditions, its current sharing control and MPPT control do not need to be very fast, which justifies the feasibility of this method for most applications.

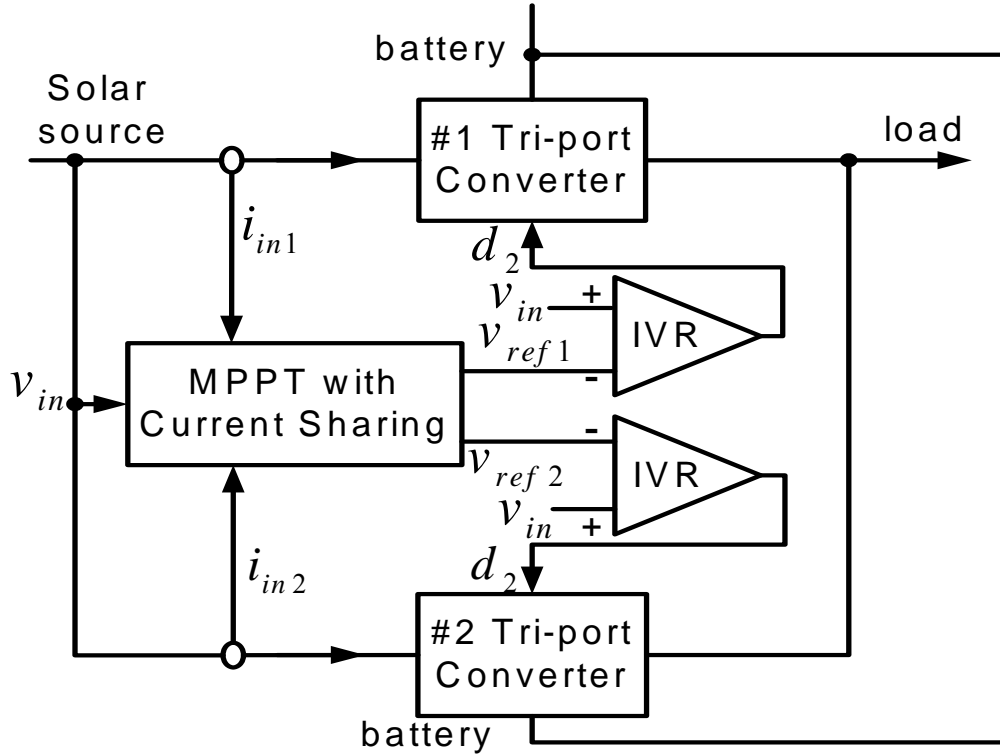


Fig.4. 15: Input port current sharing diagram

4.3. Experiments for Two Three-port Converters

The proposed CS structure for three power ports is tested through a 400W prototype as shown in Figure 4.17, which consists of one DSP controller board and two paralleled three-port power stages (each converter rated at 200W). Figure 4.18 shows the test setup.

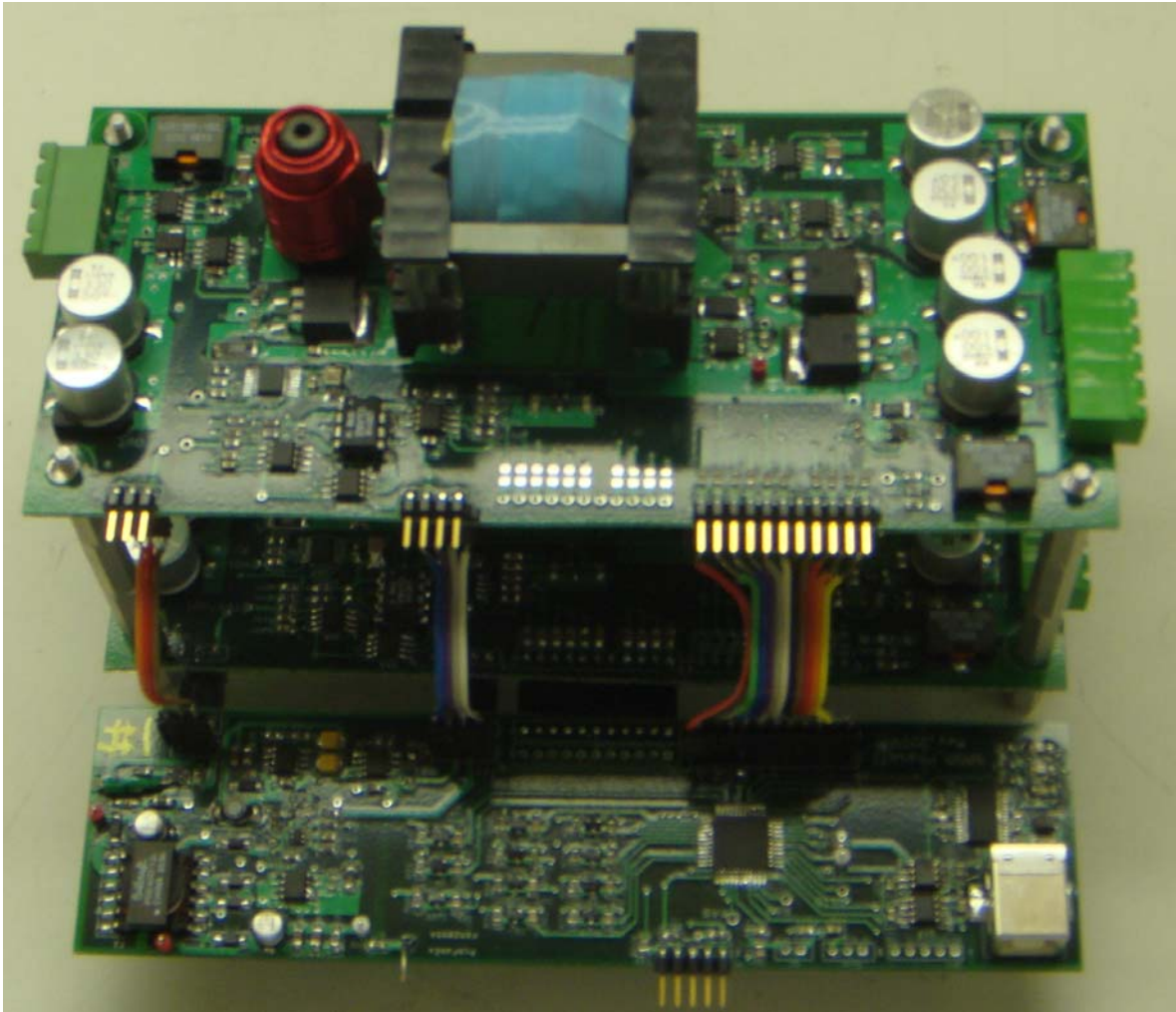


Fig.4. 17: Prototype photo of two paralleled converters sharing with one DSP controller board, each power stage is rated at 200W, input port and battery port has the same ground while output port is isolated.

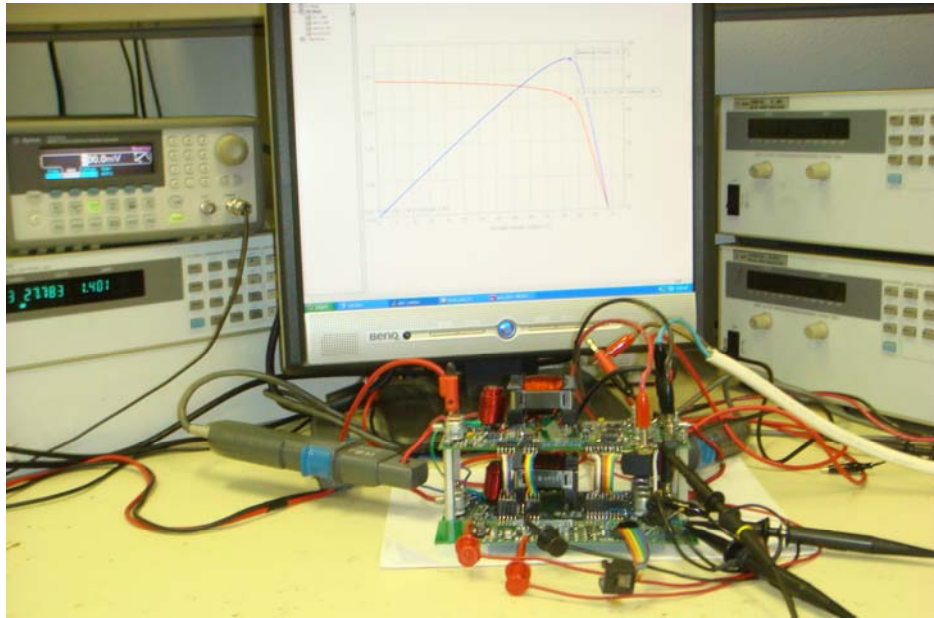


Fig.4. 18: Test setup with two paralleled three-port converters

Figure 4.19 demonstrates the steady state waveforms when output current sharing function is enabled and two converters are working under 12A load level. The converter's output filter inductor current agrees with each other while the switching node voltage shows large difference, which implies that large load current differences will occur with no CS control. This is shown in Figure 4.20 that only when the CS function is enabled, then CS can be achieved.

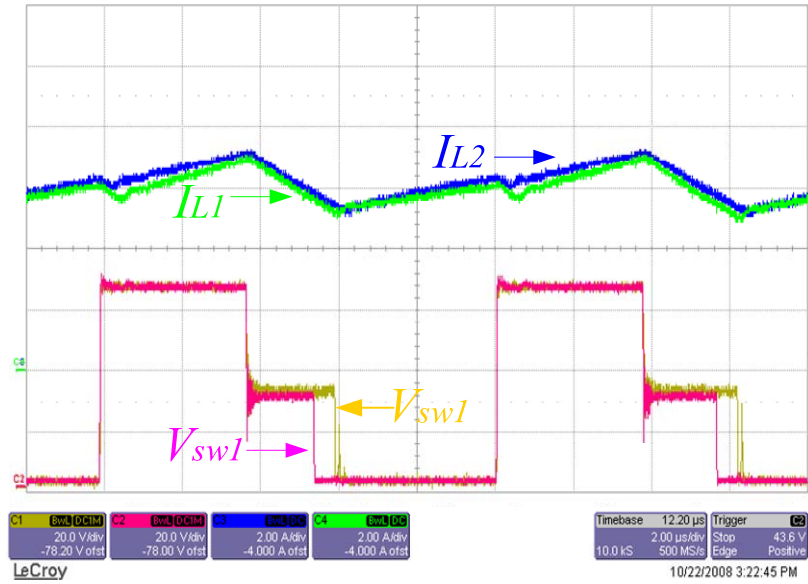


Fig.4. 19: Steady state waveforms for output inductor current and switching node voltage

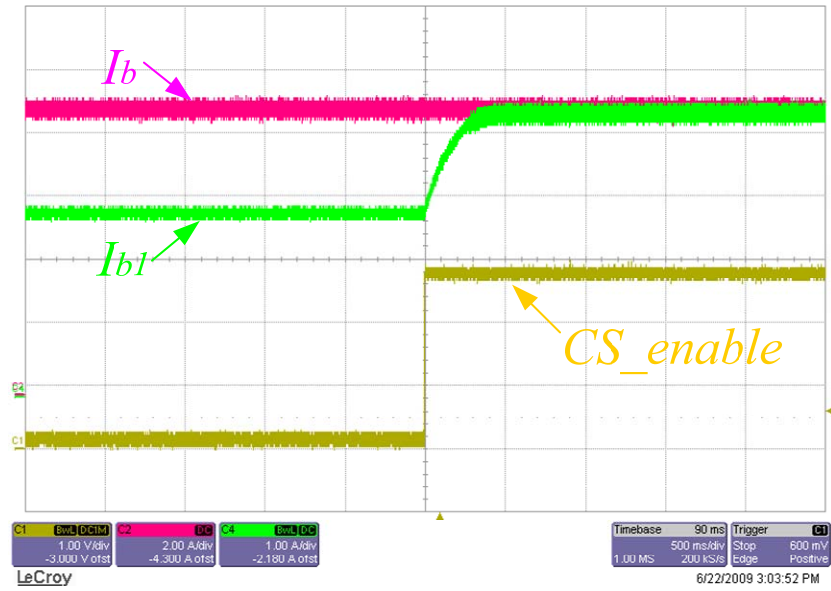


Fig.4. 20: Current sharing performance before and after CS function enabled

Figure 4.21 and Figure 4.22 exhibit the load transient response and steady state performance of output port CS, respectively. In both transients and steady state, the proposed dual loop CS enables good CS performance.

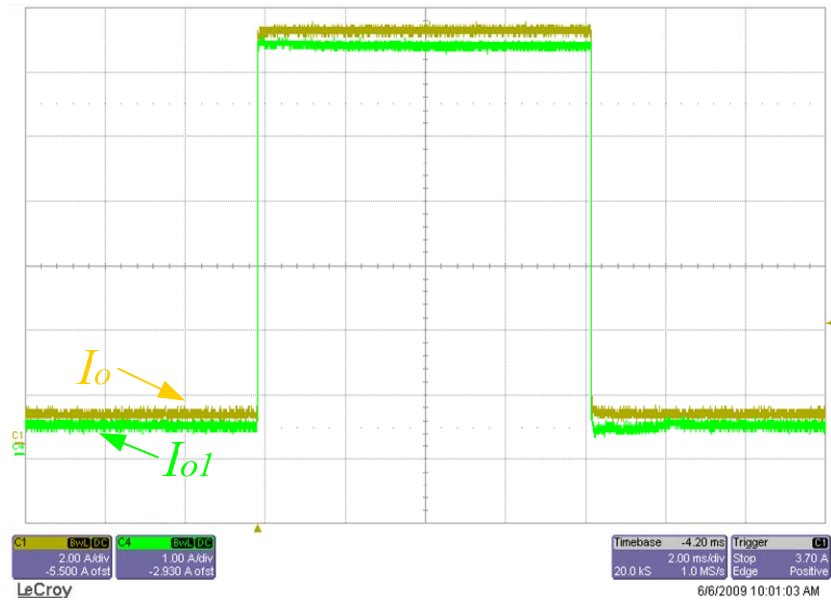


Fig.4. 21: Current sharing performance before and after CS function enabled

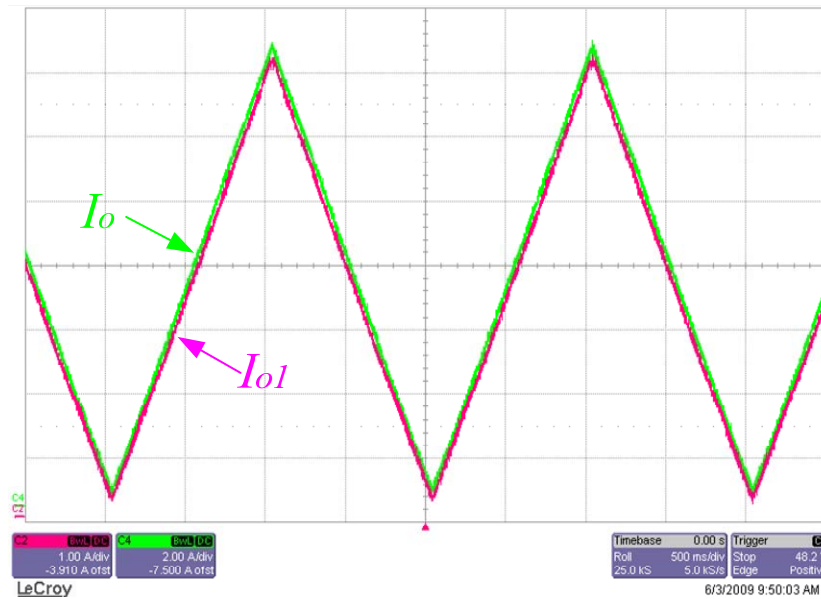


Fig.4. 22: Output port load sweep (0.5-14A)

Figure 4.23 and Figure 4.24 illustrate the load transient response and steady state performance of the battery port CS, respectively. The battery voltage changes according to the different current level.

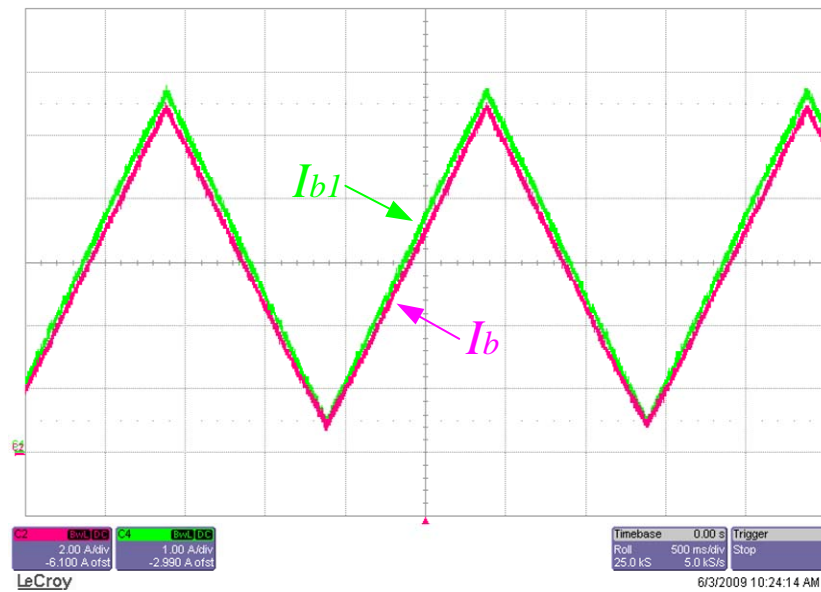


Fig.4. 23: Battery port load sweep (0.5-11A)

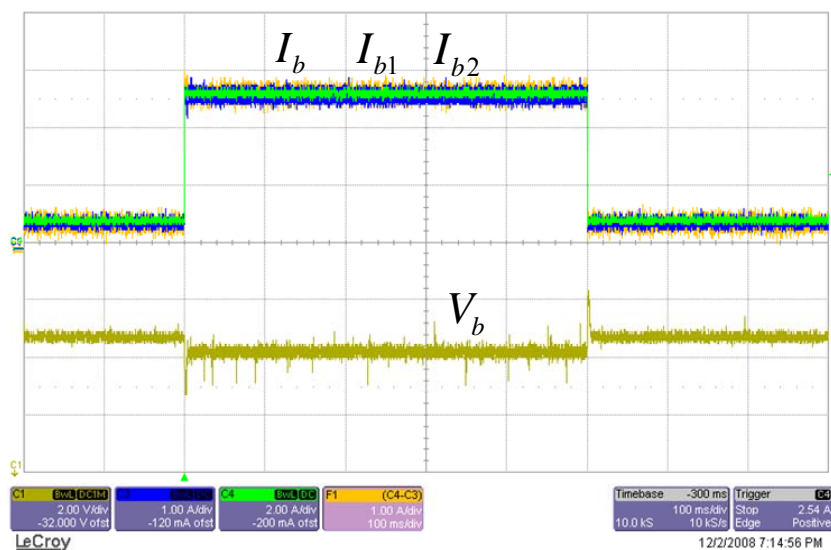


Fig.4. 24: Battery load transient (1-5.5A)

Figure 4.25 and Figure 4.26 give the real world bode plots for output port and battery port, which are obtained from the frequency analyzer. As can be observed, with CS loop closed or open, it does not make big differences for output port voltage feedback loop, which proves that CS loop and voltage loop can be assumed to be decoupled for the output port. Also, the result agrees with simulated bode plots provided in section 4.2.1. For the battery port, whether the droop CS function is added or not, the bode plots for BVR loop are the same because the droop CS basically takes the open-loop fashion, and does not affect the close-loop characteristics.

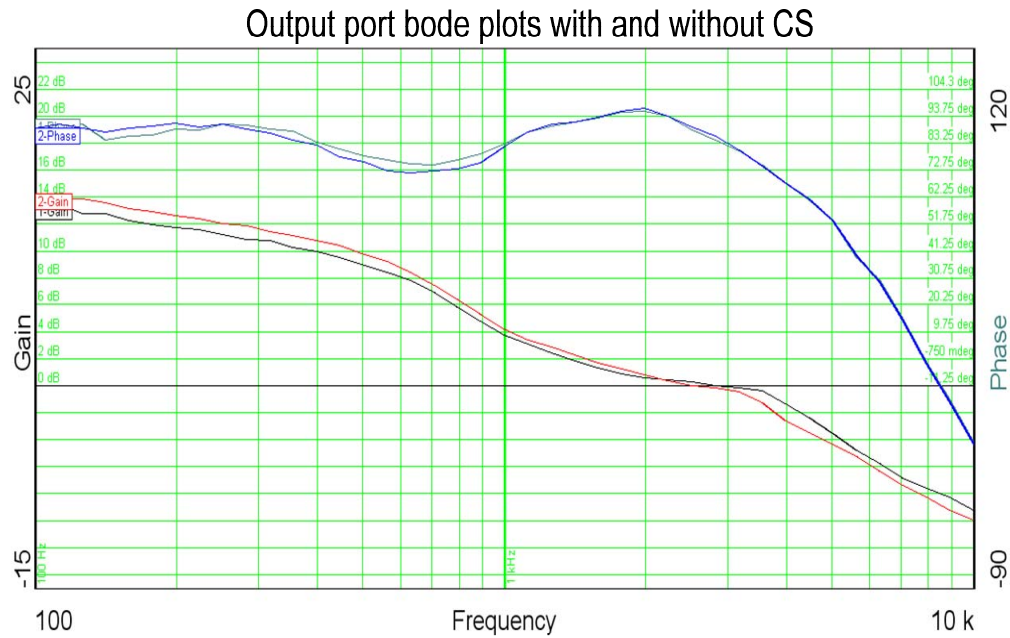


Fig.4. 25: Measured bode plots of output port (T_v and T_{sys} agree with each other)

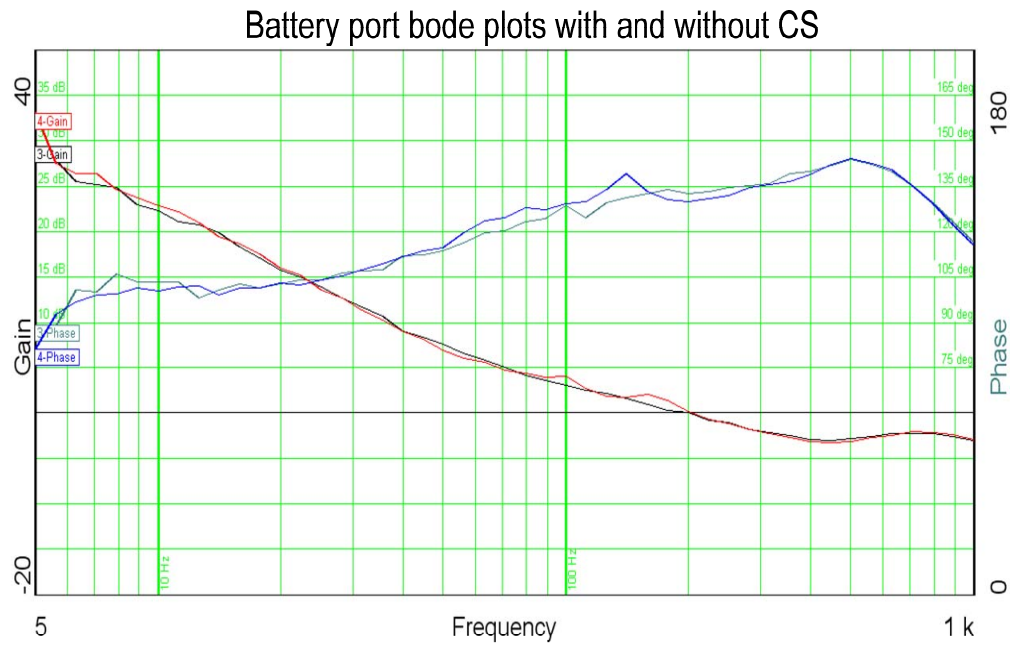


Fig.4. 26: Measured bode plots of battery port, droop CS does not affect BVR loop

4.4. Multi-channel Paralleled Three-port Converters

As shown in Figure 4.27 two converters are connected at each port to form one channel, and these independent channels have different solar sources, while the battery ports and output ports are all connected together to interface with one battery pack and the distribution bus which provides power to satellite user power system consisting of all kinds of different loads. The distributed PV panel structure allows maximum solar power harvesting for each PV panel.

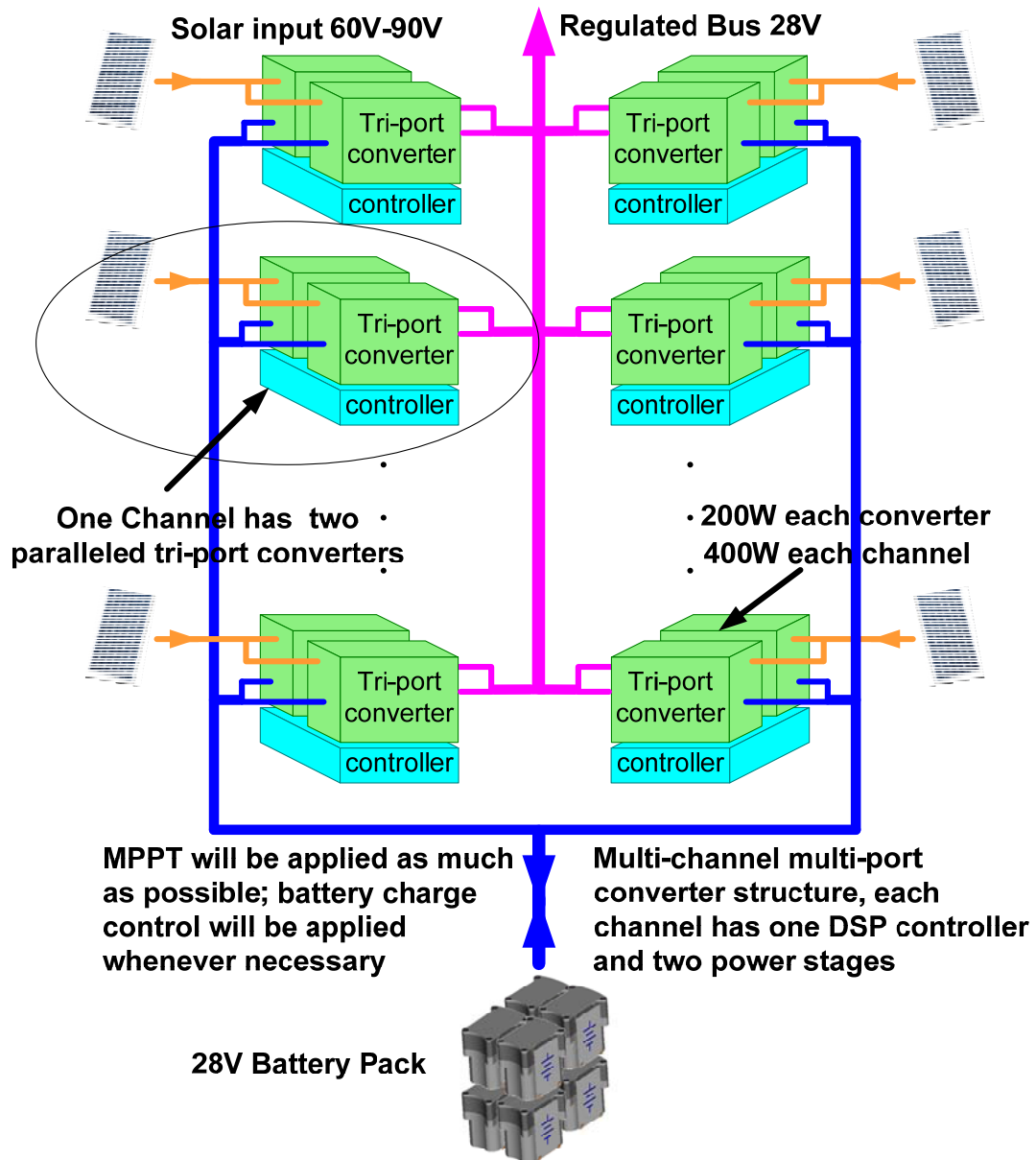
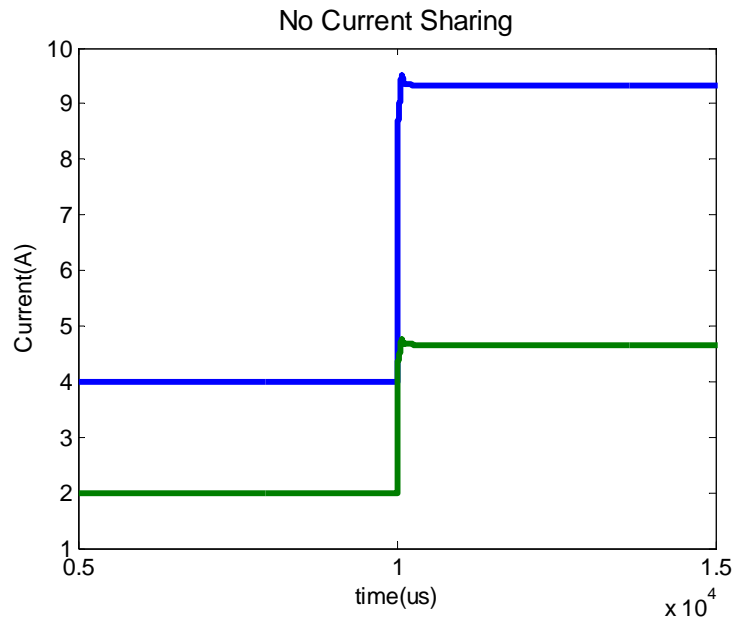


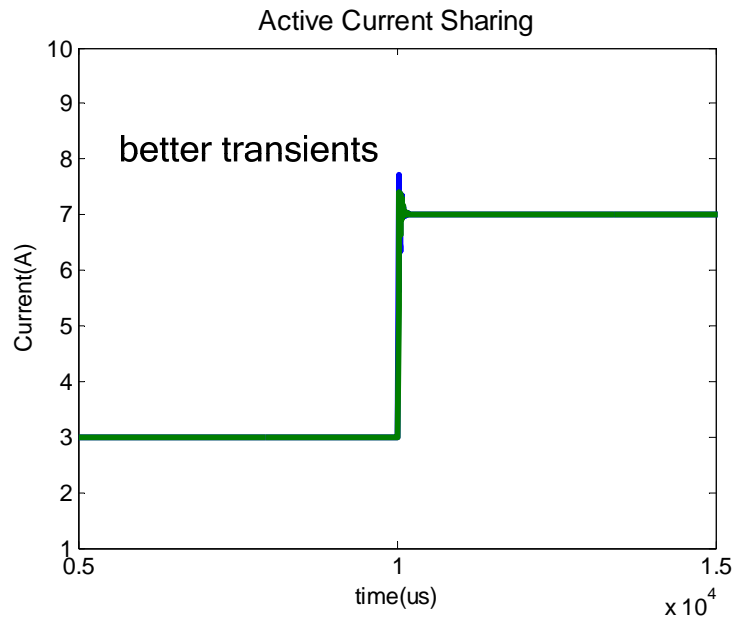
Fig.4. 27: Multi-channel converter structure

Current Sharing control (CS) is necessary to equally distribute power at both intra & inter-channel level. There are basically two categories of CS method, active method [50]-[54] and passive droop method [55], [56]. Active CS has better transients but it requires one or two shared

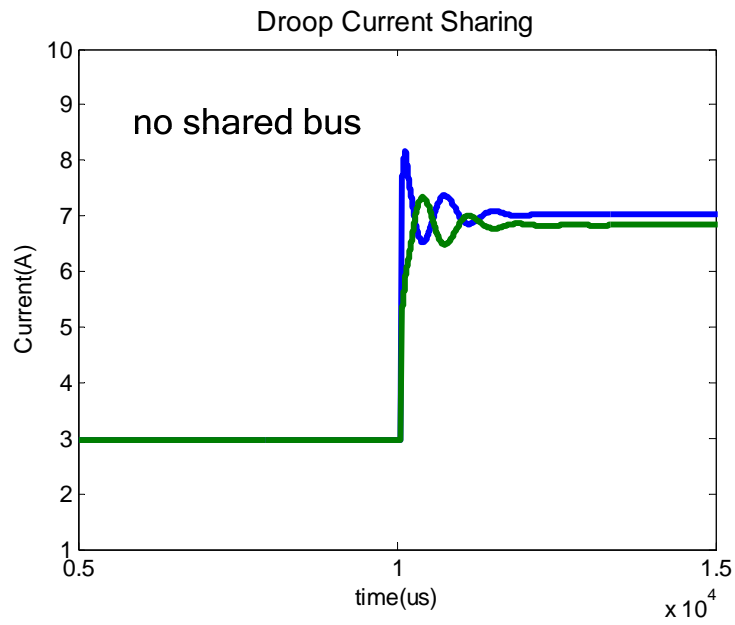
bus, meaning that real time communication necessitating extra wiring is required among different channels (inter-channel level), which is difficult to implement and easy to catch up noise. On the other hand, droop CS method requires no bus structure, and the droop rate can be programmed conveniently within DSP instead of inserting real resistors which will dissipate power. Figure 4.28 gives the CS result with different methods. In order to take advantage of both active and passive CS method, a hybrid CS method is proposed for output port CS control strategy. “Hybrid” means active CS at intra-channel level and droop CS at inter-channel level. Therefore, compared with droop method, hybrid method has better transients and will allow lower current limit setting to have better circuit protections due to the inherent active CS structure (Figure 4.28(b)). For input port and battery port, proposed intra-channel CS functions in section 4.2.3 and 4.2.4 are well suited to existing MPPT or battery charge control, and can be extended to apply for the multi-channel operation.



(a)



(b)



(c)

Fig.4. 28: CS results with different approaches: (a) no current sharing, (b) active current sharing, (c) droop current sharing.

4.4.1. Output Port Hybrid Current Sharing Method

The output port hybrid CS method is shown in Figure 4.29. On top of the dual loop CS structure presented in section 4.2, the voltage reference is subtracted by some droop voltage, which accounts for the current sharing among different channels.

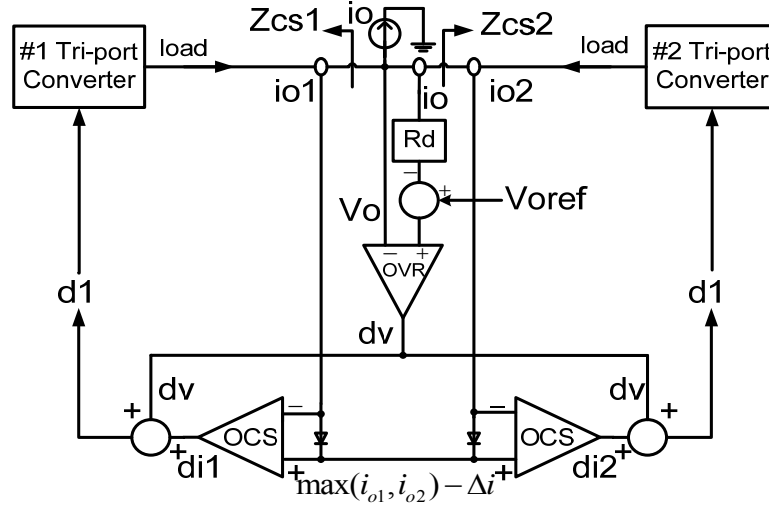


Fig.4. 29: Output port hybrid CS structure

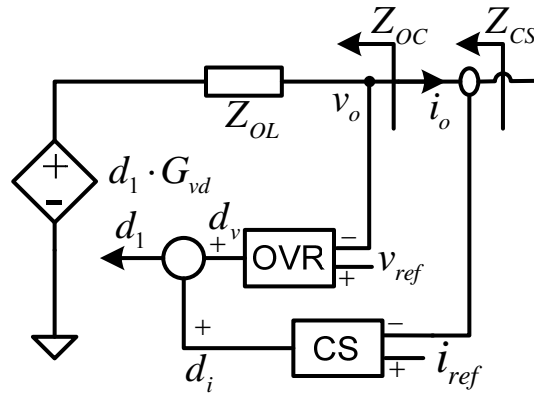


Fig.4. 30: Thevenin equivalent circuit

This section introduces an effective method to judge CS performance through the thevenin equivalent impedance, thus output impedance is to judge output CS performance. Its DC value determines steady state CS error, and the dynamic CS performance during transients is determined by its impedance value over the interested frequency range. T_o illustrate the impedance analysis approach, the power stage is represented by a thevenin equivalent circuit in series with an impedance as shown in Figure 4.30. We can understand Z_{OL} , Z_{OC} , Z_{CS} as follows: Z_{OL} represents the open loop impedance without considering OVR and CS loop; Z_{OC} represents the close loop impedance with OVR closed but CS loop left open; Z_{CS} represents the modified impedance with both OVR and CS closed. In other words, we can simply treat the converter as a black box only represented by this small signal impedance Z_{CS} . And Z_{CS} for each module can be derived as follows:

$$\left\{ \begin{array}{l} Z_{CS1} = -\frac{v_o}{i_{o1}} = \frac{Z_{OL1}}{1 + H_{OVR} \cdot G_{vd1}} \\ Z_{CS2} = -\frac{v_o}{i_{o2}} = \frac{Z_{OL1} \cdot Z_{OL2} + Z_{OL1} \cdot H_{CS} \cdot G_{vd2}}{Z_{OL1} + (1 + H_{OVR} \cdot G_{vd1}) \cdot H_{CS} \cdot G_{vd2} + H_{OVR} \cdot G_{vd2} \cdot Z_{OL1}} \end{array} \right. \quad Eq. 4.5$$

The expression for the admittance Y_{CS2} which is the reciprocal of Z_{CS2} can be further simplified as follows:

$$Y_{CS2} = (Y_{OC2} + Y_{OC1} \cdot T_{CS}) / (1 + T_{CS}) \quad Eq. 4.6$$

Where $T_{CS} = H_{CS} \cdot G_{vd2} / Z_{OL2}$ is defined as the CS loop gain.

Examination of this equation indicates that in the case of identical modules ($Y_{OC1} = Y_{OC2}$), the term $(1 + T_{CS})$ will cancel out meaning that CS will be achieved naturally for such identical

modules. But unfortunately modules are not identical in reality due to their variations of parameters. So the objective is to modify terminal impedance to make them equal to each other in the desired frequency range. For instance, if the crossover frequency of CS loop gain T_{CS} is designed to be high, the impedance of different converter terminals will be altered to match each other in that frequency range as shown in Figure 4.31. As a result, CS transients of hybrid CS will be improved compared with conventional droop method as shown in Figure 4.32.

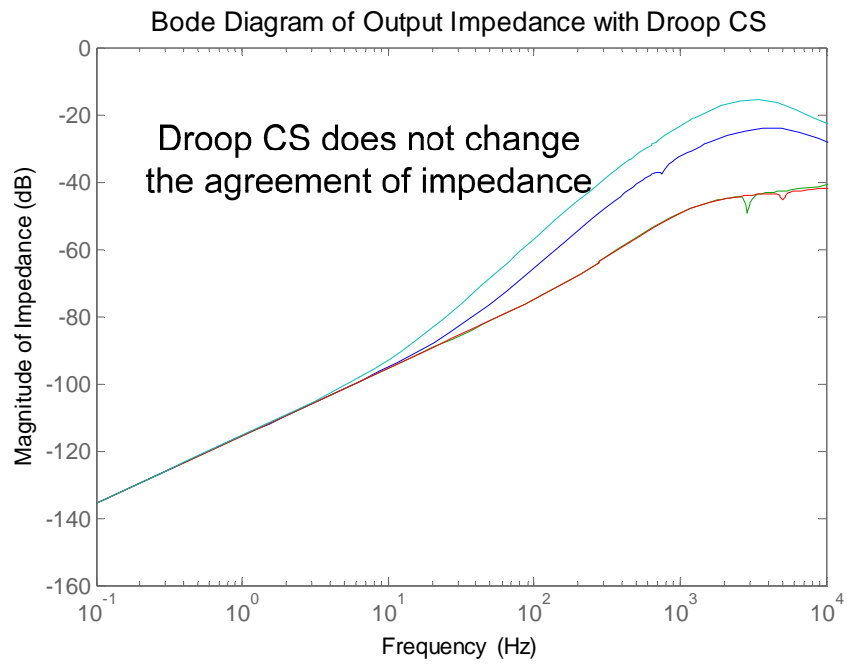
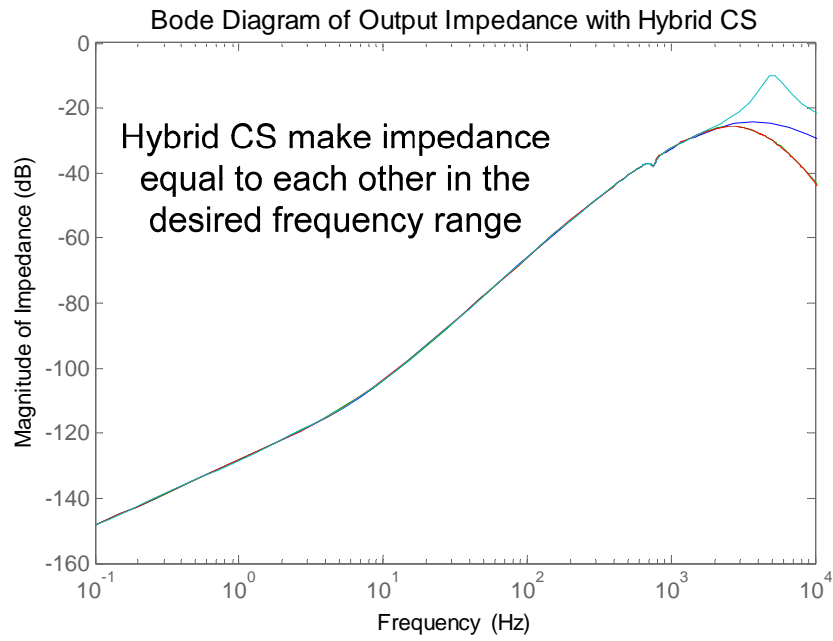
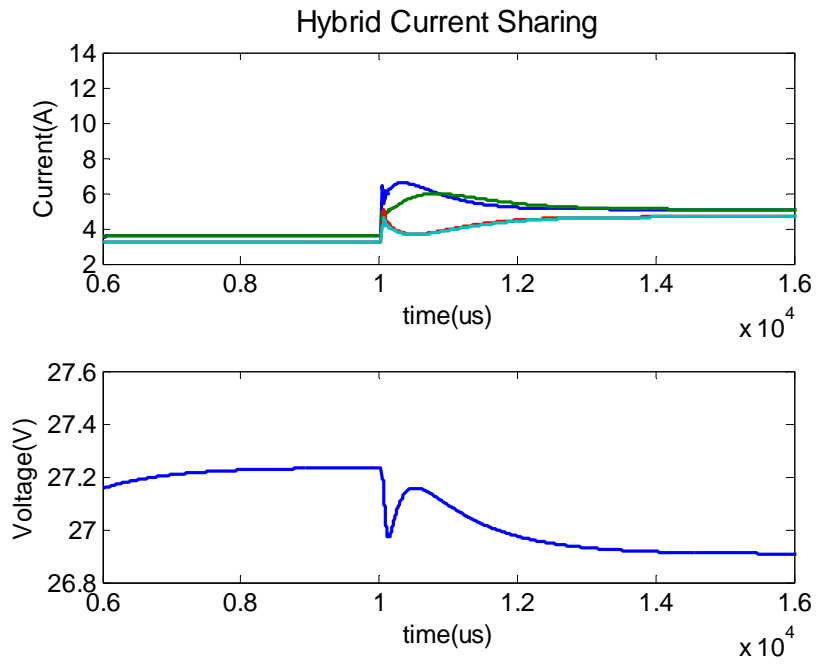
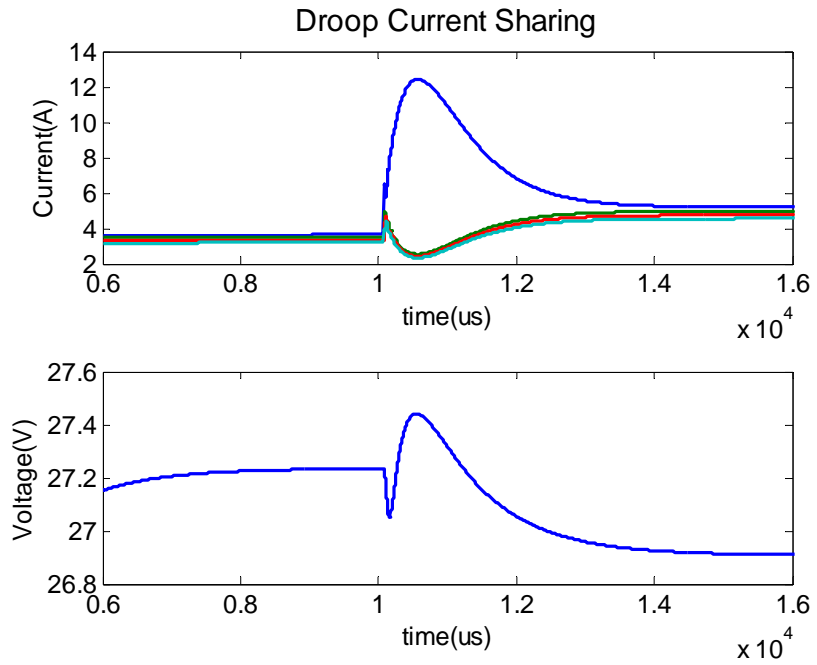


Fig.4. 31: Output impedance with (a) hybrid CS and (b) droop CS method.



(a)

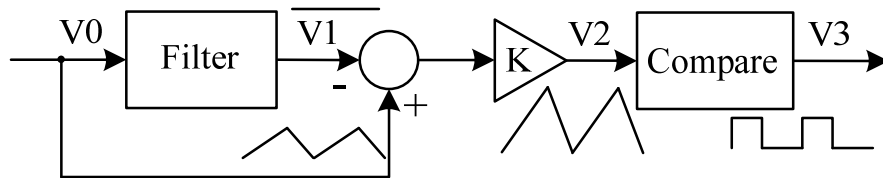


(b)

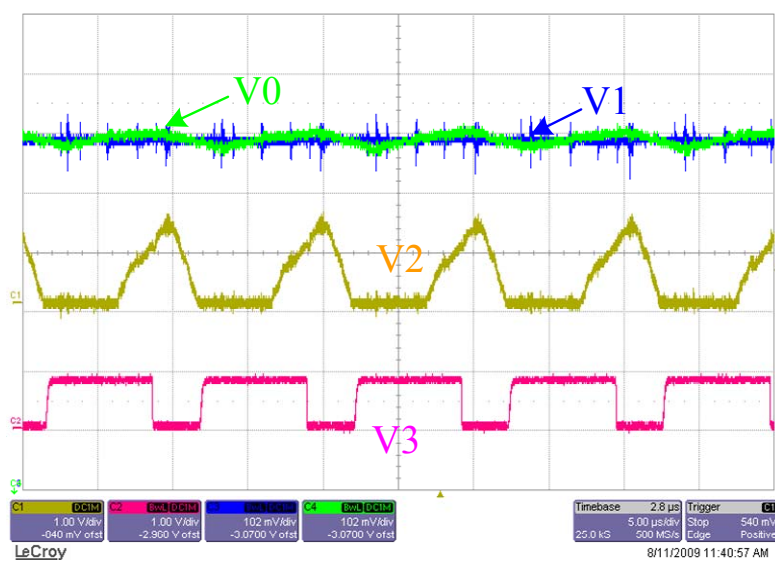
Fig.4. 32: CS simulation results; (a) hybrid CS method, (b) droop CS method.

4.4.2. Synchronization Among Different Channels

Since each channel has its own DSP controller and each DSP has its own timing circuitry, when multiple channels are paralleled, timing circuitry drifting can be observed. Furthermore, switching frequency at the level of 100 kHz is drifting. Due to small impedance among different channels' ports, even small voltage ripple can cause large current ripple, which is shown in Figure 4.34. Therefore synchronization is necessary and the “wireless” solution would be preferred due to the noise issue of wiring and the freedom to place the converter channels at different locations closer to users. The block diagram implementation method is illustrated in Figure 4.33(a). The output voltage has the ripple actually including the switching frequency and exact switching point information. By processing this signal, DSP synchronization could be achieved. The original output voltage signal V_0 will be first filtered to obtain an average value of V_1 , deducted by V_0 and then amplified by coefficient K to be V_2 , finally comparing with some preset value to generate a square waveform which feeds back into DSP to trigger the PWM counter. By this way, every DSP can be synchronized by the same signal, which is output voltage. In our design, the falling edge is used to trigger PWM counters.

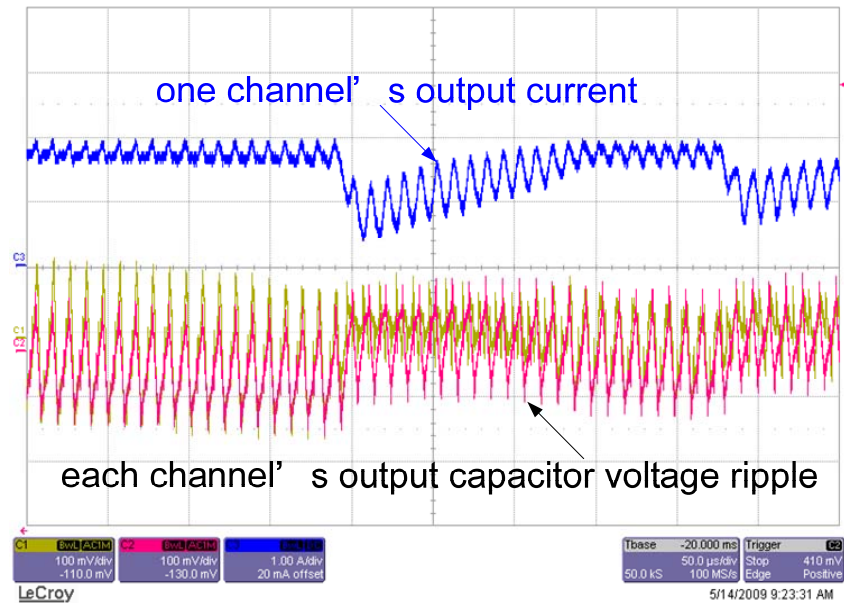


(a)

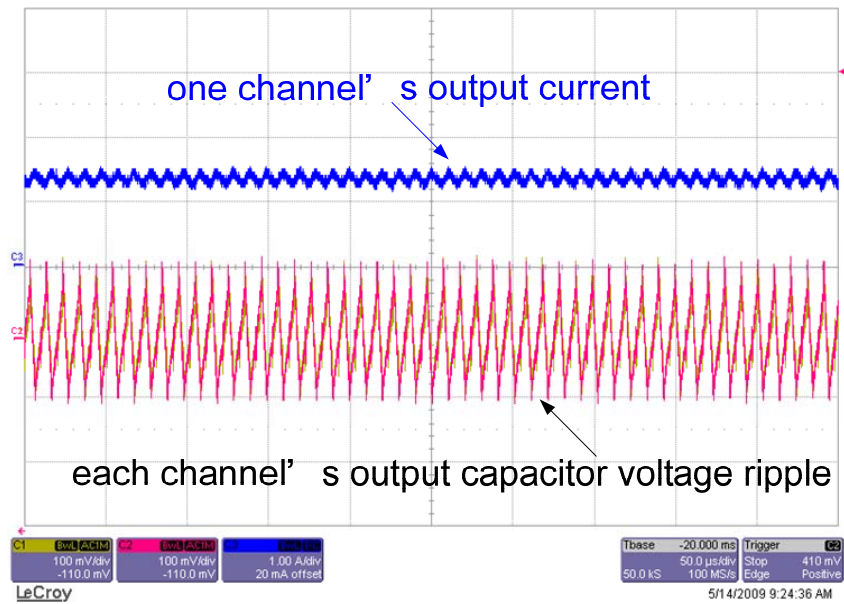


(b)

Fig.4. 33: Implementation of synchronization with no wires: (a) circuit block diagram; (b) waveforms



(a)



(b)

Fig.4. 34: Signal synchronization, (a) without synchronization; (b) with synchronization

4.5. Experiments for Multiple Three-port Converters

The three-port converter system is verified through a two-channel four-converter prototype rated at 800W as shown in Figure 4.35. Figure 4.36 gives the output port CS performance. Hybrid CS has better load transients than conventional droop method. It should be noted that the proposed hybrid CS does not affect steady state CS performance as the droop rate is the same for both methods. As in Figure 4.37, the output voltage has no spike when one channel fails, which implies the fault-tolerant feature of the multi-channel converters.

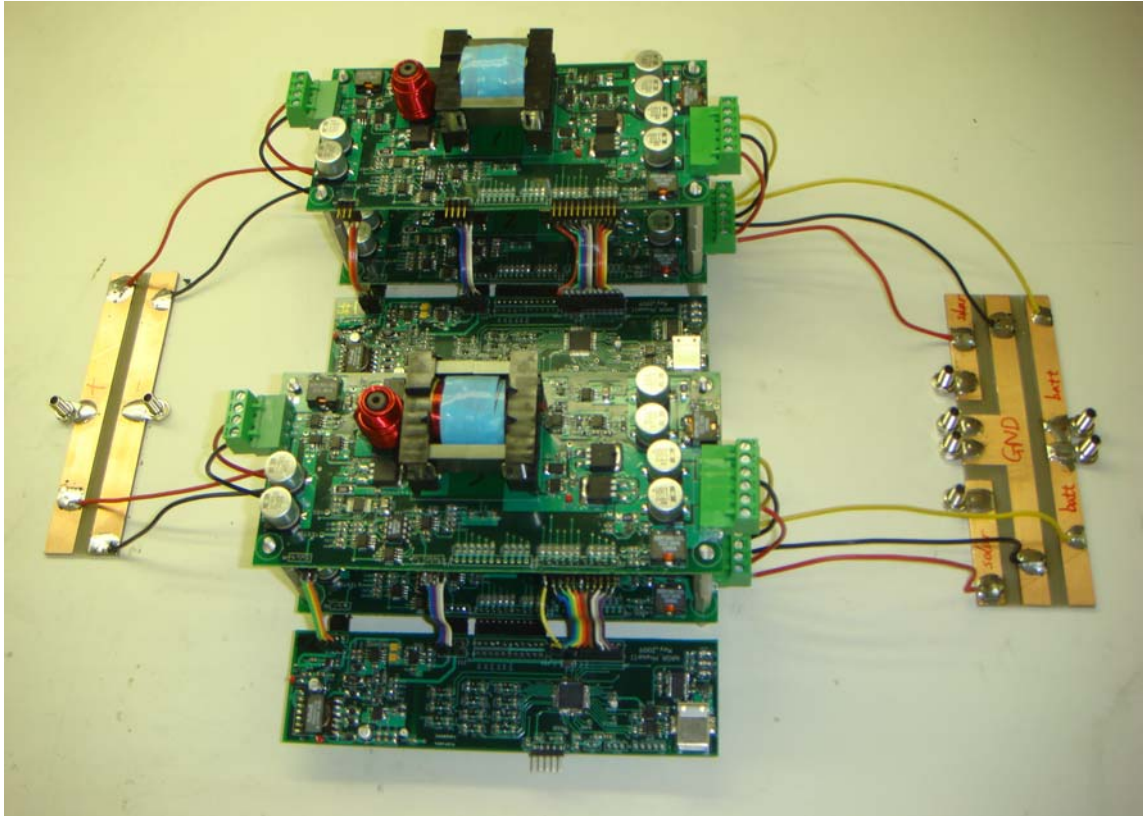
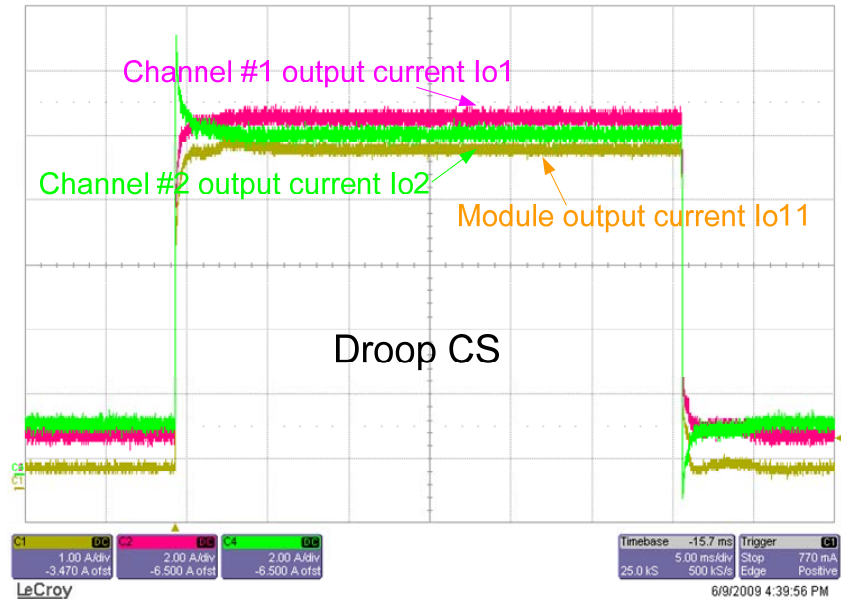
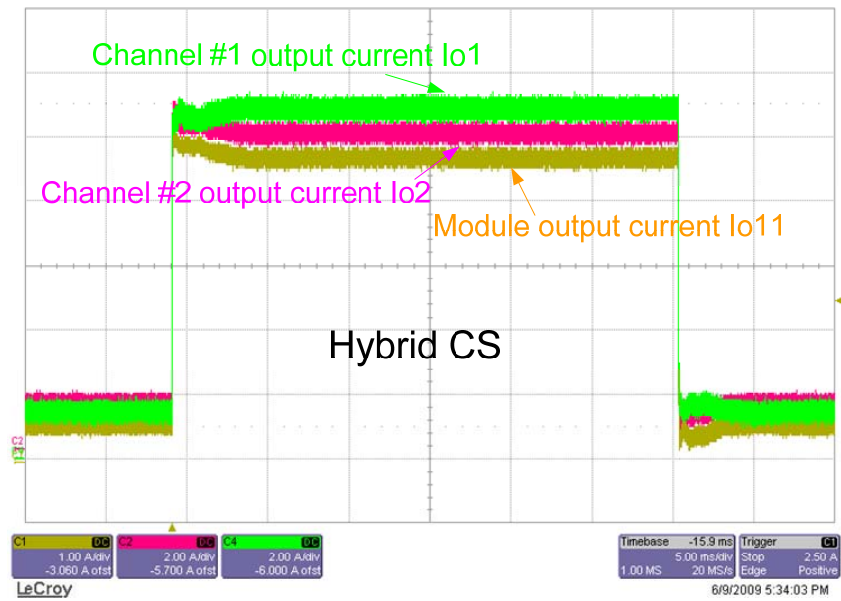


Fig.4. 35: Prototype photo of two converter channels



(a)



(b)

Fig.4. 36: Output port CS performance: (a) droop CS; (b) hybrid CS with better transients.

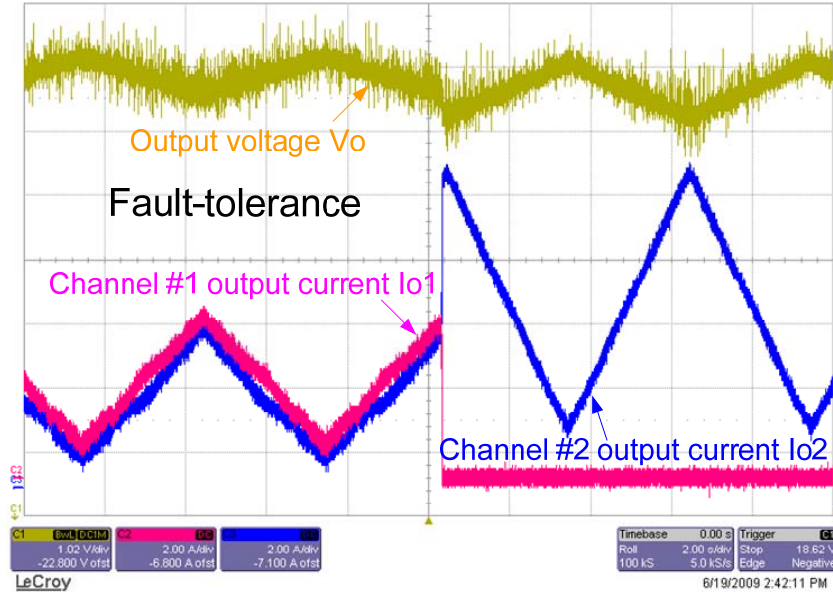


Fig.4. 37: One channel fails while the other channel is not affected.

Figure 4.38 shows that input CS compatible with MPPT algorithm, and even during solar irradiance level changes, input currents agree with each other. Figure 4.39(a) shows that both channels are working under MPPT to maximize solar power, while battery port provides the power balance for the system when the load power changes, and two PV panel have very different maximum power points. Figure 4.39(b) shows that one channel goes to regulate battery port first because its upper voltage limit has been reached, and then followed by the other channel when the other voltage limit is met. The reason is that although V_{bmax} and R_{droop} are the same, two channels have different I_b , as a result, their voltage settings are different. Therefore, from Figure 4.39, the proposed autonomous mode transition allows smooth transition for independent channels under different conditions.

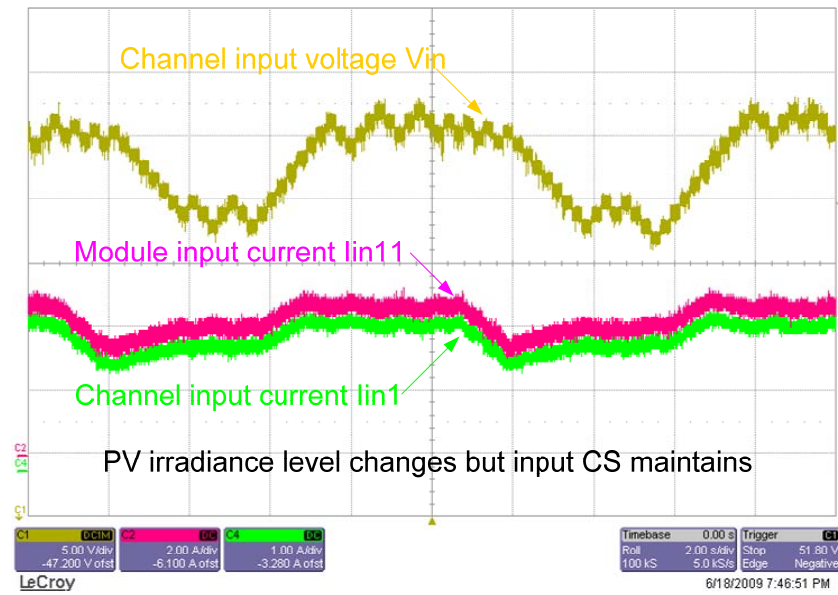
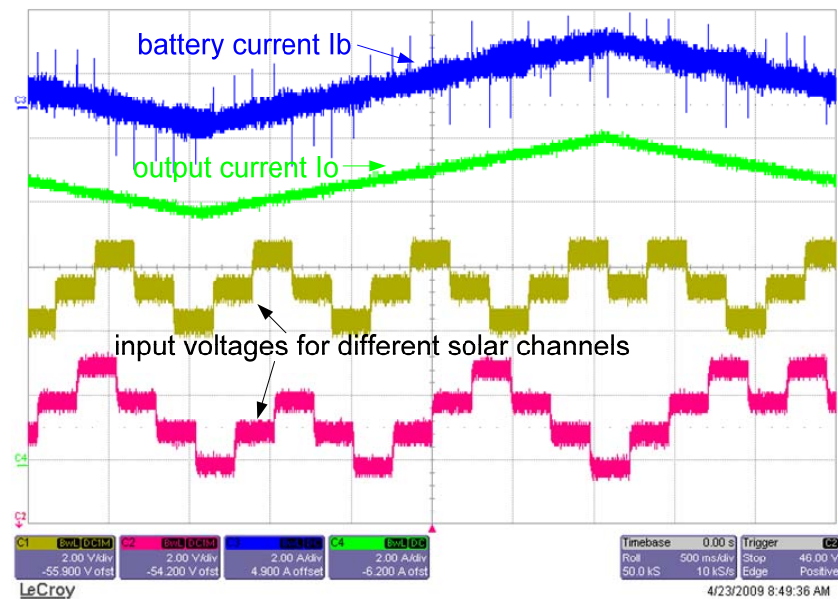
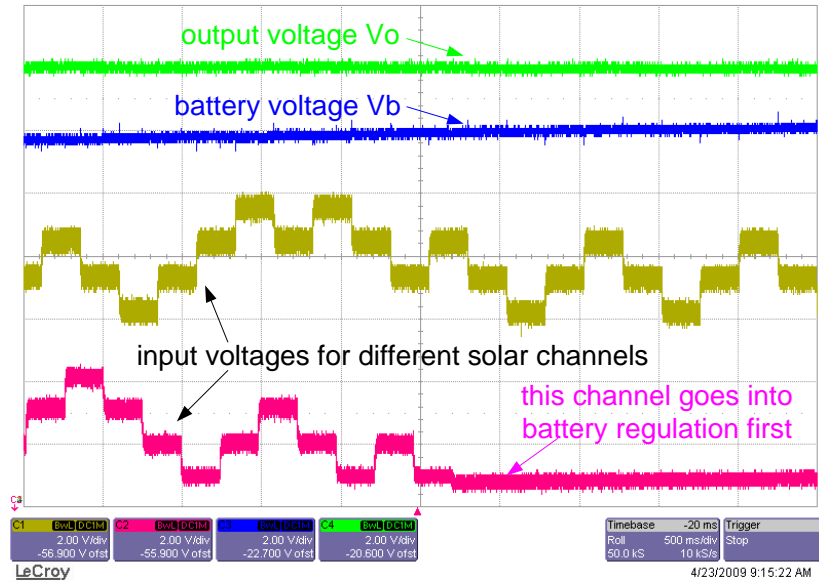


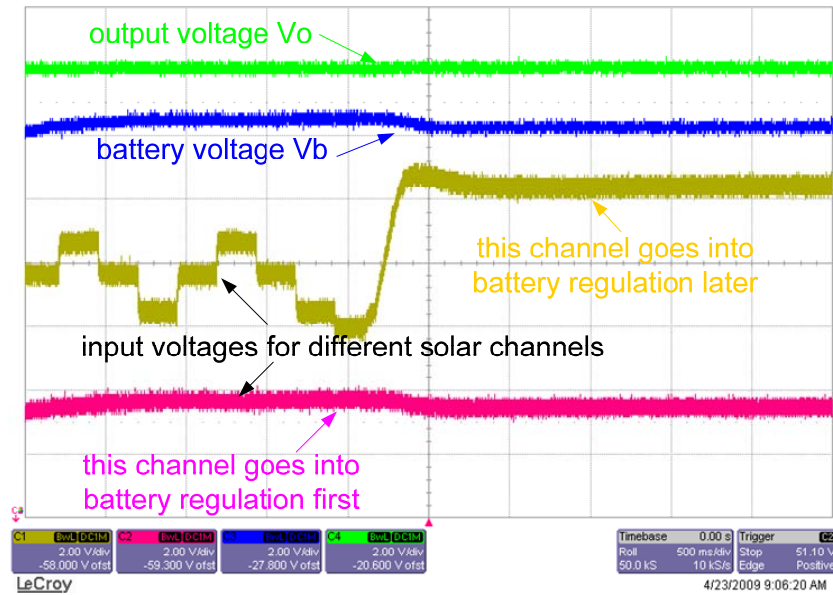
Fig.4. 38: Input Port CS with MPPT



(a)



(b)



(c)

Fig.4. 39: Autonomous mode transitions: (a) both with MPPT; (b) transit from both with MPPT to one with MPPT ; (c) transit from one with MPPT to both without MPPT.

CHAPTER 5: AN INTEGRATED FOUR-PORT DC/DC CONVERTER

5.1. General Description

As interest in renewable energy systems with various sources becomes greater than before, there is a supreme need for integrated power converters that are capable of interfacing and concurrently controlling several power terminals with low cost and compact structure. Meanwhile, due to the intermittent nature of renewable sources, a battery backup is normally required when the ac mains is not available.

This Chapter proposes a new four-port integrated DC/DC topology, which is suitable for various renewable energy harvesting applications. An application interfacing hybrid photovoltaic (PV) and wind sources, one bi-directional battery port and an isolated output port is given as a design example. It can achieve maximum power point tracking (MPPT) for both PV and wind power simultaneously or individually, while maintaining a regulated output voltage.

The proposed four-port DC/DC converter interface has bidirectional capability and also one isolated output. Its main components are only four main switches, two diodes, one transformer, and one inductor. Moreover, zero-voltage switching (ZVS) can be achieved for all main switches to allow higher efficiency at higher switching frequency, which will lead to more compact design of this multi-port converter. The control design is also investigated based on the modeling of this modified half-bridge topology. In addition, a decoupling network is introduced to allow the separate controller design for each power port. Finally, a prototype has been built to verify the

four-port converter's circuit operation and control capability. Figure 5.1 shows the four-port converter concept.

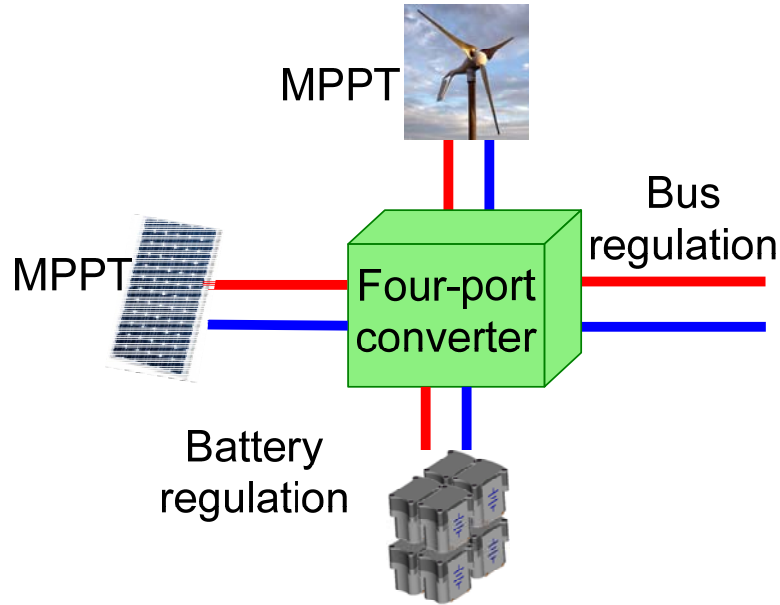


Fig. 5. 1: Four-port converter concept

5.2. Topology

The four-port topology is derived based on the traditional two-port half-bridge converter, which consists of two main switches, S1 and S2. As shown in Figure 5.2, one more input power port can be obtained by adding a diode D3 and an active switch S3. Another bidirectional power path can be formed by adding a freewheeling branch across the transformer primary side, consisting of a diode D4 and an active switch S4. As a result, the topology ends up with four active switches and two diodes, plus the transformer and the rectification circuit. The proposed converter topology is suitable for a number of power harvesting applications, and this dissertation will target the hybrid PV wind application. It should be noted that since the wind

turbine normally generates a three-phase AC power, an AC/DC rectifier needs to be installed before this four-port DC/DC interface and after the wind turbine output. The rectification stage can utilize either active Power Factor Correction (PFC) or passive PFC. However, it should be noted that the AC/DC solution is beyond the scope of this paper.

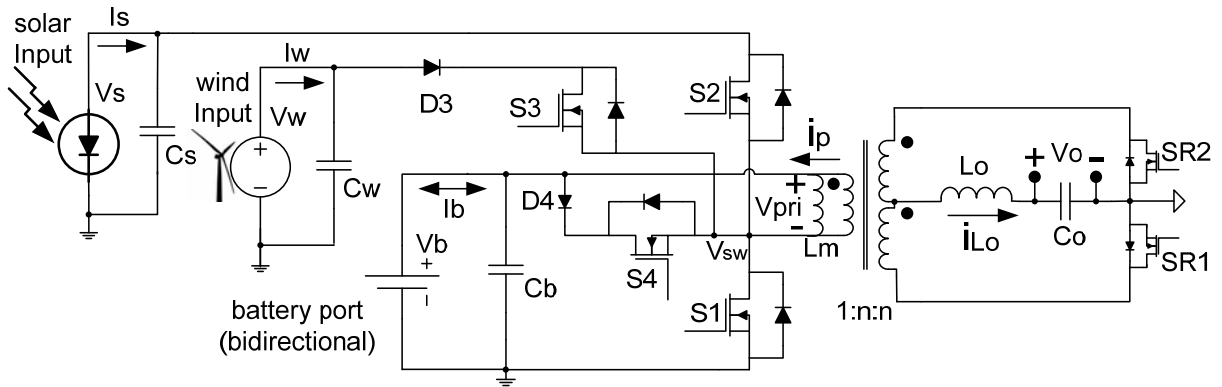


Fig. 5. 2: The four-port half-bridge converter topology, which can achieve ZVS for all four main switches ($S1$, $S2$, $S3$ and $S4$) and adopts synchronous rectification for the secondary side to minimize conduction loss.

As shown in Figure 5.2, the derived four-port modified half-bridge converter provides three independent control variables, namely duty-cycles d_1 , d_2 and d_3 to control $S1$, $S2$ and $S3$, respectively, while $S4$ will be controlled by $1-d_1-d_2-d_3$. This allows tight control over three of the converter ports, while the fourth port provides the power balance in the system. The switching sequence ensures a clamping path for the energy of the leakage inductance of the transformer. This energy is further utilized to achieve zero-voltage switching (ZVS) for all primary switches for a wide range of source and load conditions. The secondary side adopts a synchronous rectifier to minimize the conduction loss. This also simplifies the feedback controller design,

because the transition from continuous conduction mode (CCM) to discontinuous conduction mode (DCM) is avoided.

5.2.1. Driving Scheme

Figure 5.3 illustrates a possible modulation approach to realize the constant frequency pulse width modulation (PWM) control. Where V_{SAW} is the SAW carrier waveform for modulation, V_{C1} , V_{C2} and V_{C3} are control voltages derived from the voltage or current feedback controllers. By modulating these control voltages, driving signals for S1, S2 and S3 can be generated, respectively. Then by reversing S1 and S3 driving signals, S4 and two SR signals can be obtained. It should be noted that S2, S3 and S4 do not need to be gated on at the same time; instead, S3 is only required to turn on a little earlier before S2 turns off, and S4 is only required to turn on a little earlier before S3 turns off. No dead time is necessary between S2 and S3, nor between S3 and S4, because the existing of diodes can prevent shoot-through problems. But the dead time between S1 and S2 and between S1 and S4 is necessary to prevent shoot-through, and also to create ZVS conditions for S1 and S2.

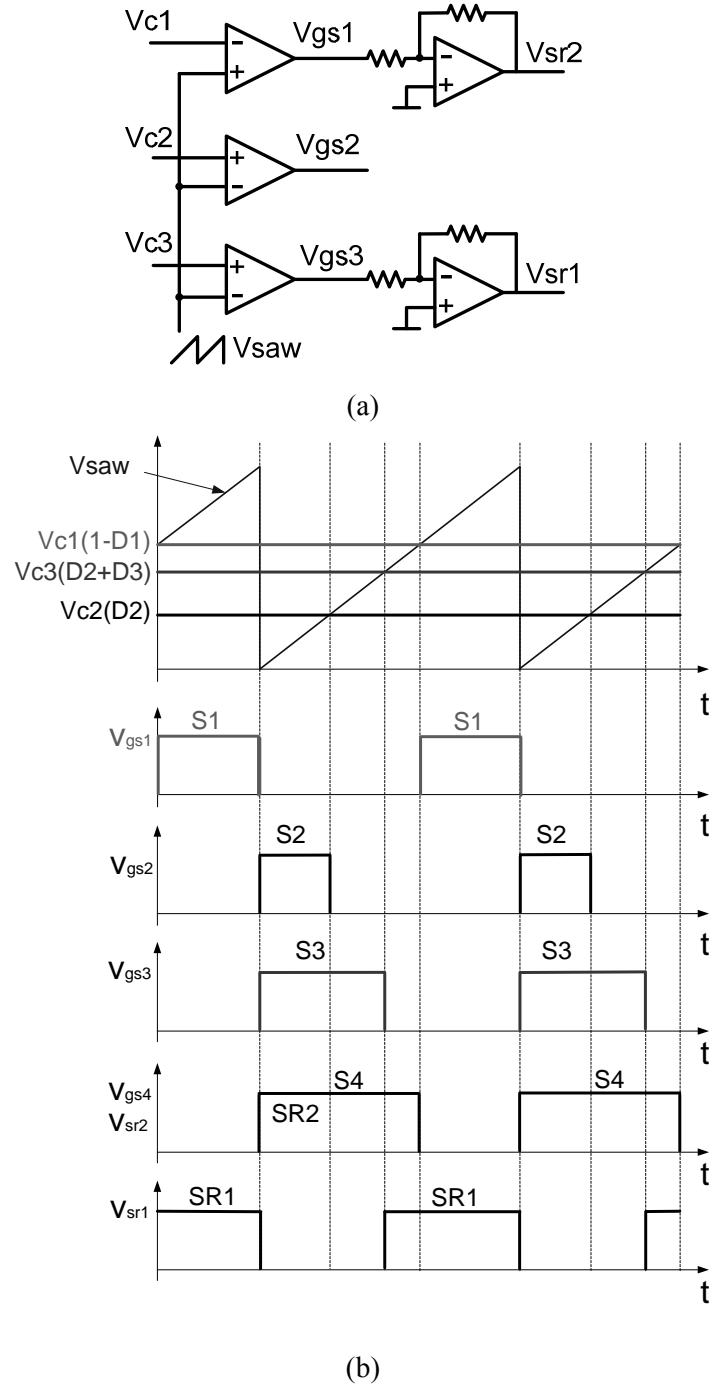


Fig. 5. 3: The proposed modulation scheme: (a) PWM modulation circuits; (b) driving signal key waveforms.

5.2.2. Circuit Operation Principles

The steady-state waveforms of the four-port converter are shown in Figure 5.4, and the various operation stages in one switching cycle are shown in Figure 5.5. To simplify the analysis of operation, components are considered ideal except otherwise indicated. The main operation stages are described as follows.

Stage 1 (t_0 - t_1): Before this stage begins, the body diode of S1 is forced on to recycle the energy stored in the transformer leakage inductor, and the output is freewheeling. At time t_0 , S1 is gated on with ZVS, and then the leakage inductor is reset to zero and reverse-charged.

Stage 2 (t_1 - t_2): At time t_1 , the transformer primary current increases to the reflected current of i_{Lo} , the body diode of SR2 becomes blocked, and the converter starts to deliver power to the output.

Stage 3 (t_2 - t_3): At time t_2 , S1 is gated off, causing the leakage current i_p to charge the S1 parasitic capacitor and discharge the S2, S3 and S4 parasitic capacitors.

Stage 4 (t_3 - t_4): At time t_3 , the voltage across the S2 parasitic capacitor is discharged to zero, and the S2 body diode conducts to carry the current, which provides the ZVS condition for S2. During this interval, the output is freewheeling through SR1 and SR2 body diodes.

Stage 5 (t_4 - t_5): At time t_4 , S2 is gated on with ZVS, and then the leakage inductor is reset to zero and reverse-charged. The output inductor current drop from t_2 to t_5 is due to the leakage inductor discharge/charge.

Stage 6 (t_5 - t_6): At time t_5 , the transformer primary current increases to the reflected current of i_{Lo} , the body diode of SR1 is blocked, and the converter starts to deliver power to the output.

Stage 7 (t_6 - t_7): At time t_6 , S2 is gated off, causing the leakage current i_p to charge the S2 parasitic capacitor and discharge the S1 and D3 parasitic capacitors.

Stage 8 (t_7 - t_8): At time t_7 , the voltage across D3 is discharged to zero, and then D3 conducts. S3 is gated on before this time, so S3 has natural ZVS. Output inductor current freewheels through SR2 during this period.

Stage 9 (t_8 - t_9): At time t_8 , S3 is gated off, causing the leakage current i_p to charge S2 and S3 parasitic capacitors and discharge S1 and D4 parasitic capacitors.

Stage 10 (t_9 - t_{10}): At time t_9 , the voltage across D4 is discharged to zero, and D4 conducts. Since S4 is gated on before this time, the leakage current freewheels through D4 and S4 so that the leakage energy is trapped. On the secondary side, output inductor current freewheels through SR1 and SR2.

Stage 11 (t_{10} - t_{11}): At time t_{10} , S4 is gated off, causing the trapped leakage energy to discharge the S1 parasitic capacitor and charge the S2, S3 and S4 parasitic capacitors.

Stage 12 (t_{11} - t_{12}): At time t_{11} , the voltage across S1 is discharged to zero, and the S1 body diode conducts to carry the current, which provides ZVS condition for S1. During this interval, the output is freewheeling. This is the end of the switching cycle.

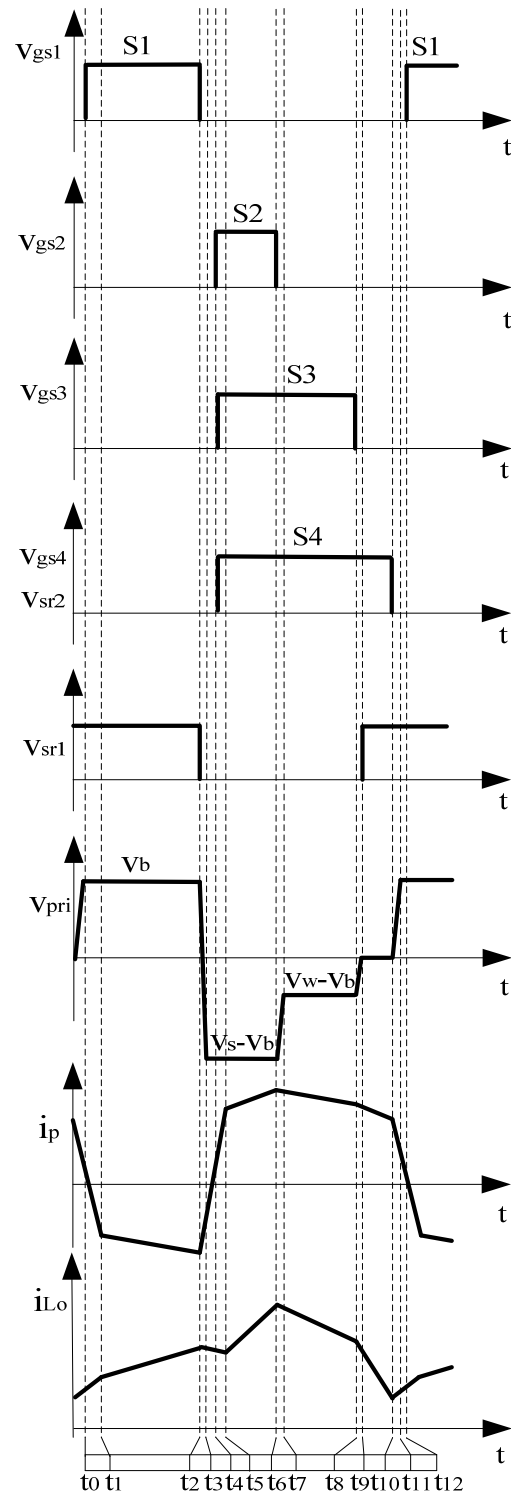
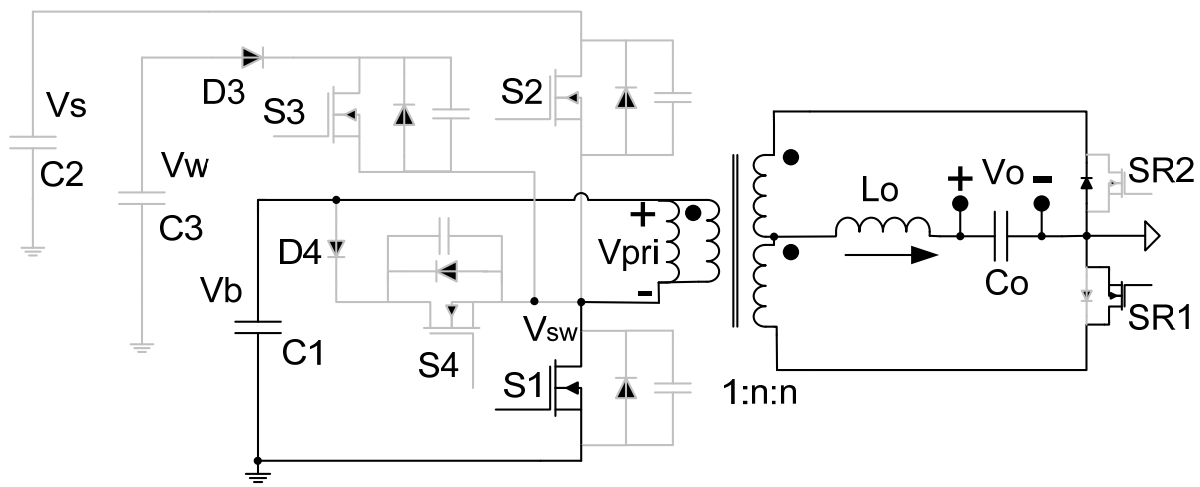
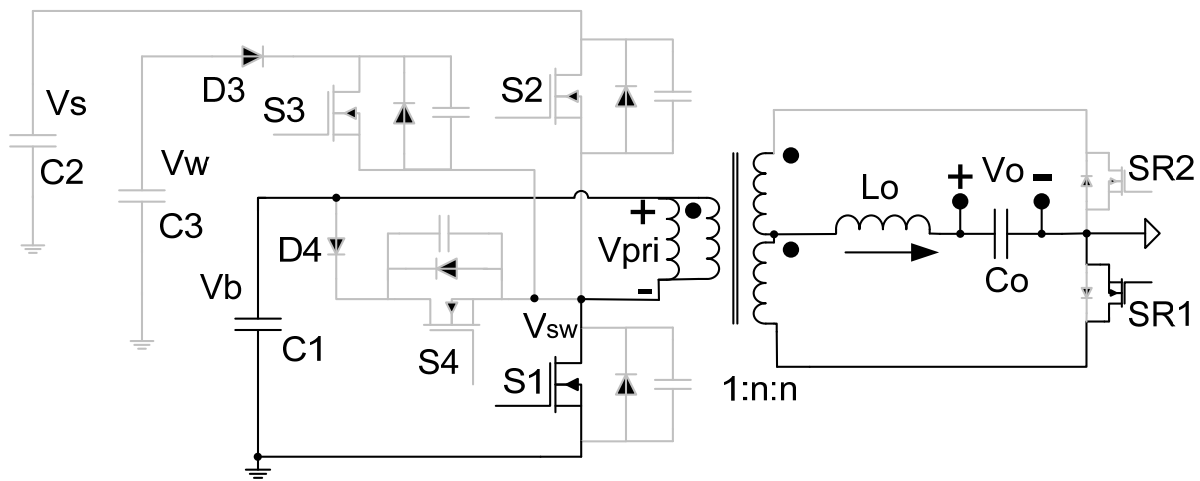


Fig. 5. 4: Steady state waveforms of the four-port half-bridge converter.



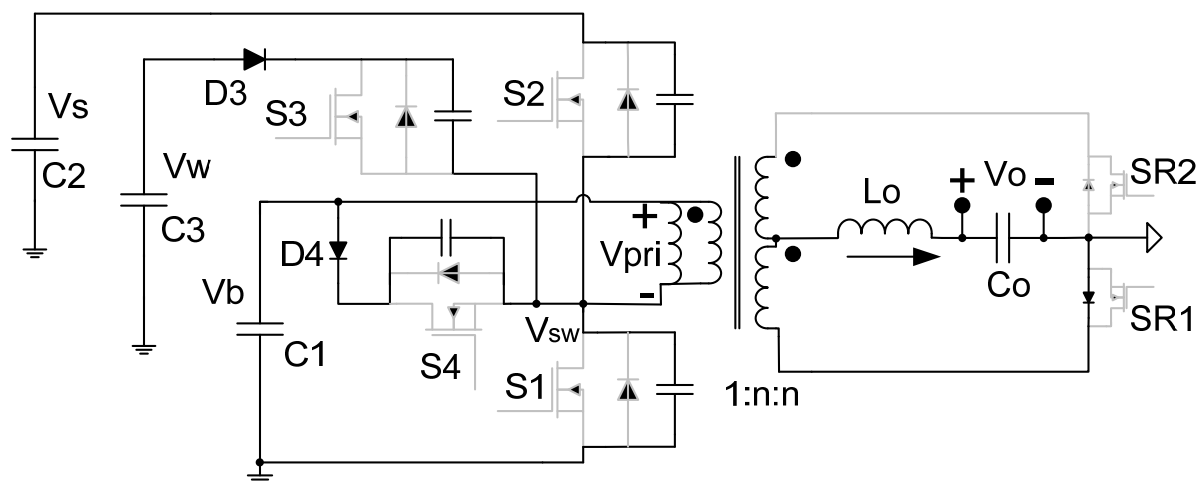
Stage I (t_0-t_1)

(a) Stage 1 operation



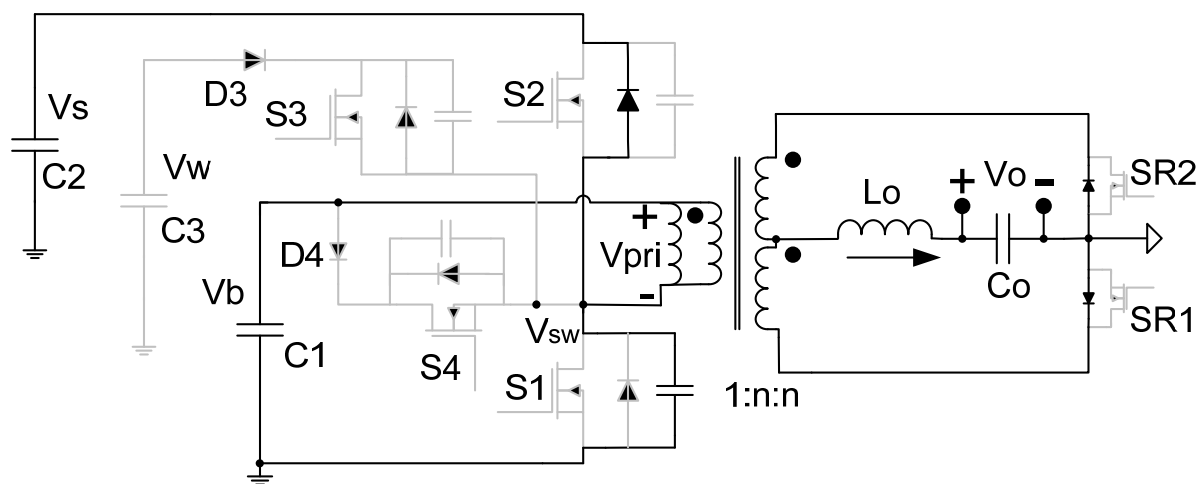
Stage 2 (t_1-t_2)

(b) Stage 2 operation



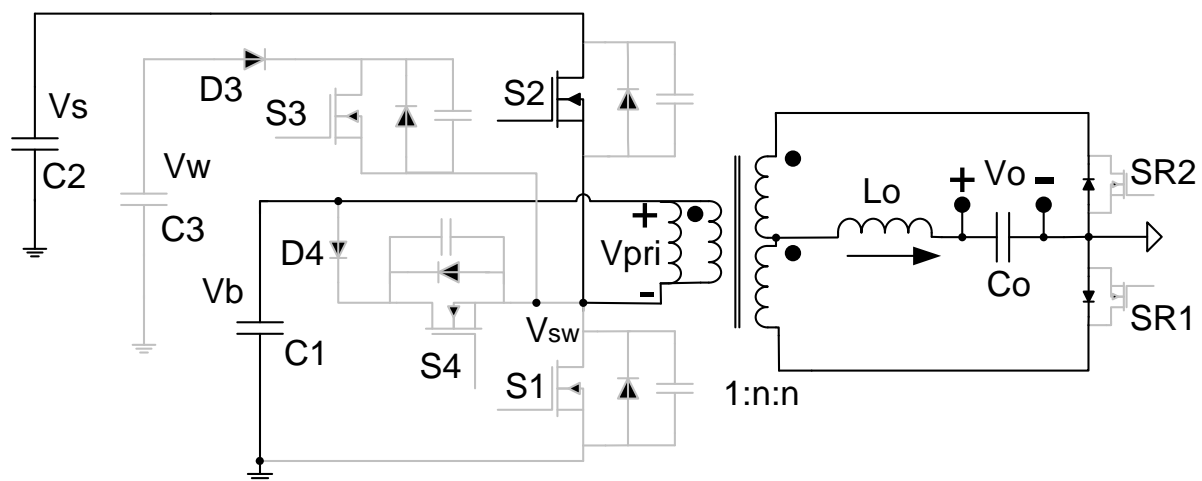
Stage 3 (t_2 - t_3)

(c) Stage 3 operation



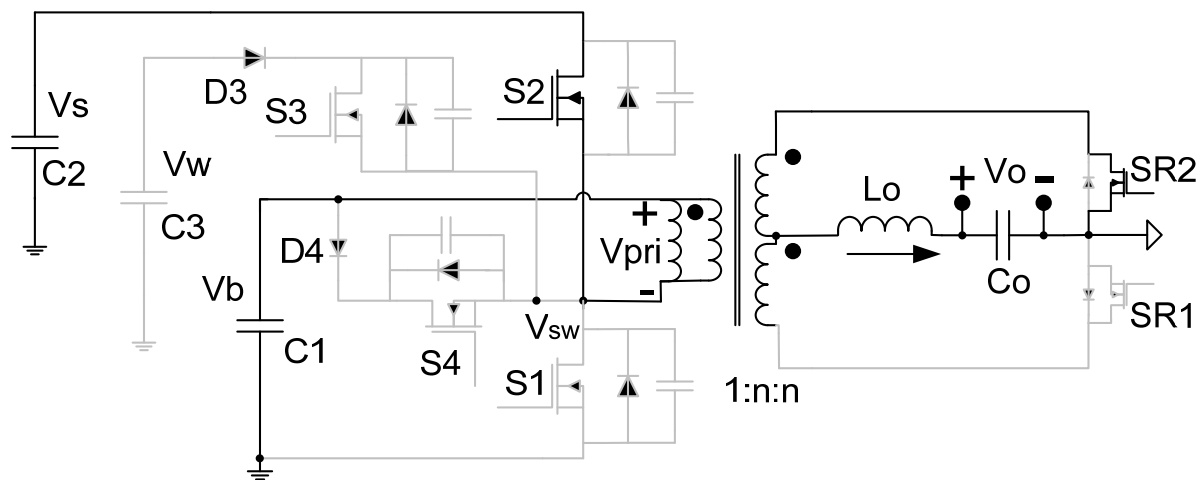
Stage 4 (t_3 - t_4)

(d) Stage 4 operation



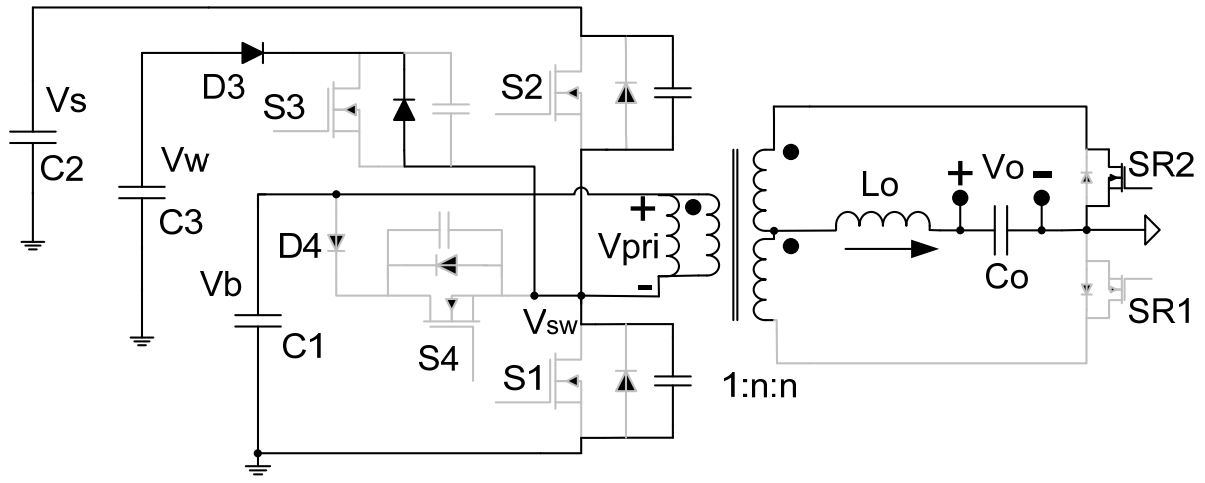
Stage 5 (t_4 - t_5)

(e) Stage 5 operation



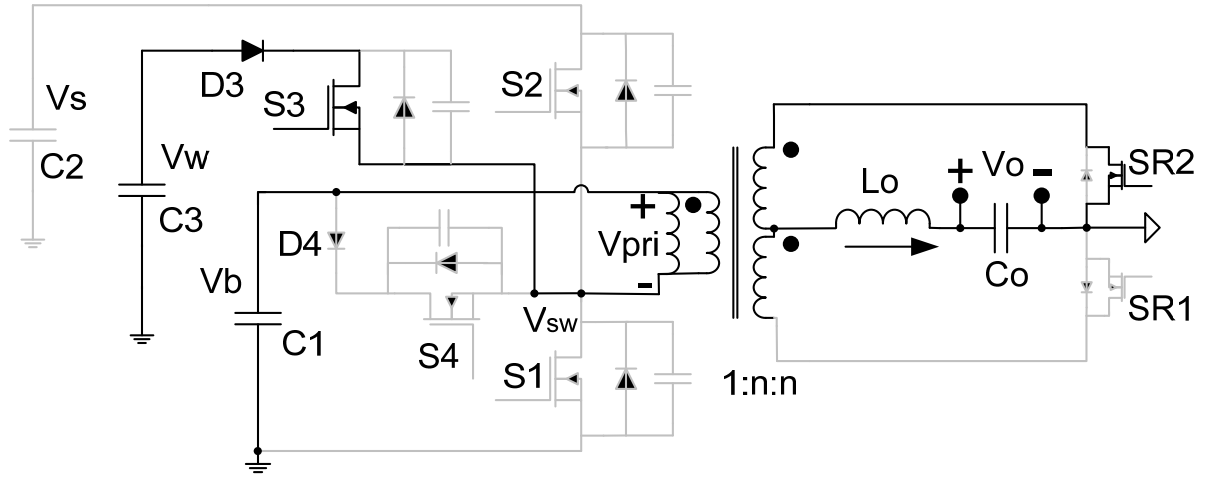
Stage 6 (t_5 - t_6)

(f) Stage 6 operation



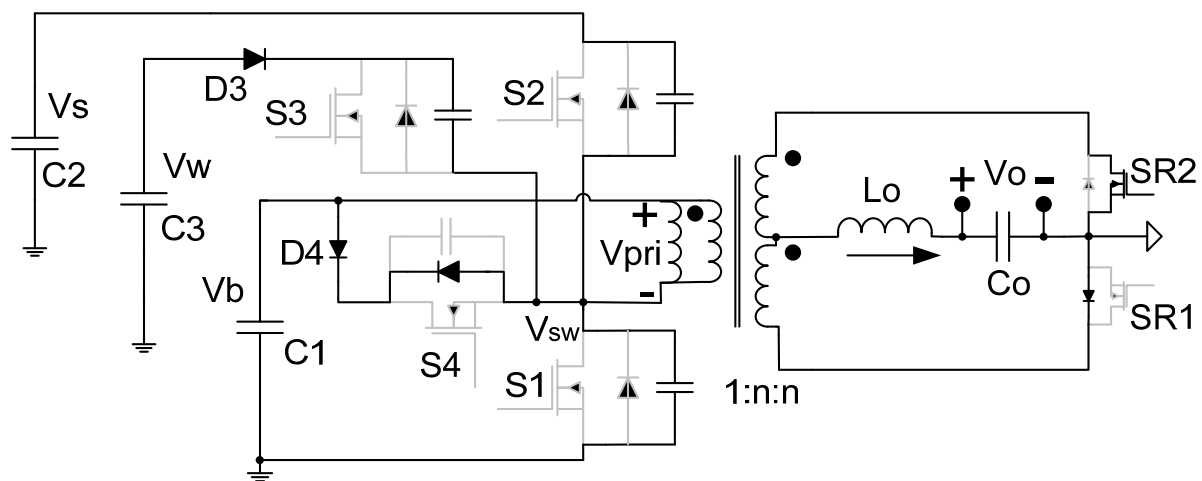
Stage 7 (t_6 - t_7)

(g) Stage 7 operation



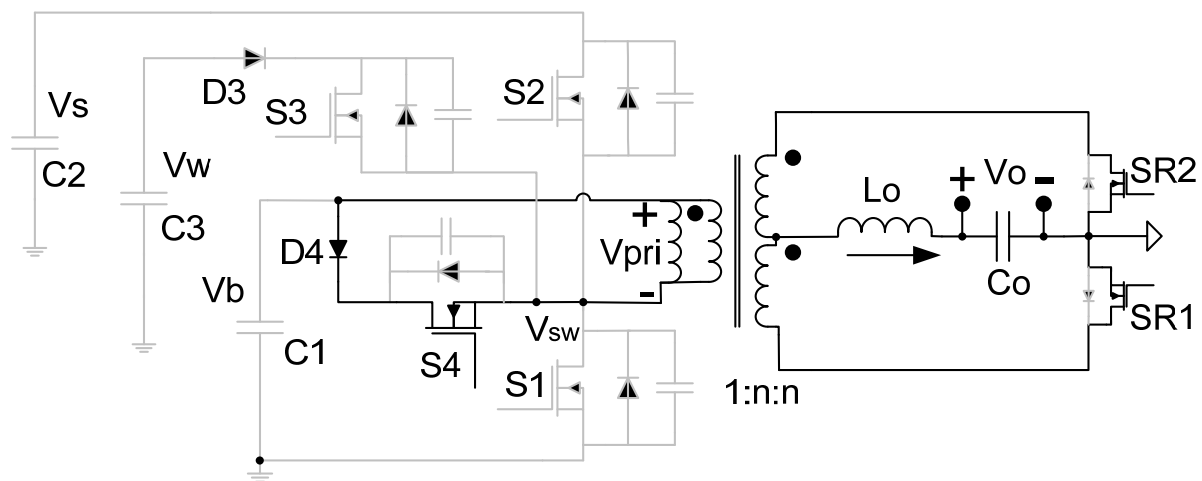
Stage 8 (t_7 - t_8)

(h) Stage 8 operation



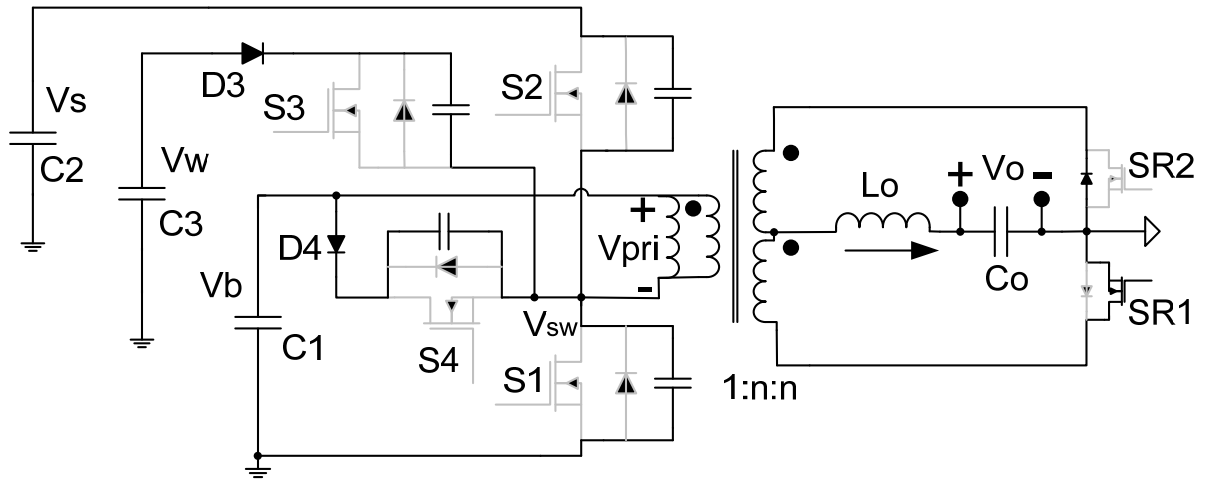
Stage 9 (t_8 - t_9)

(i) Stage 9 operation



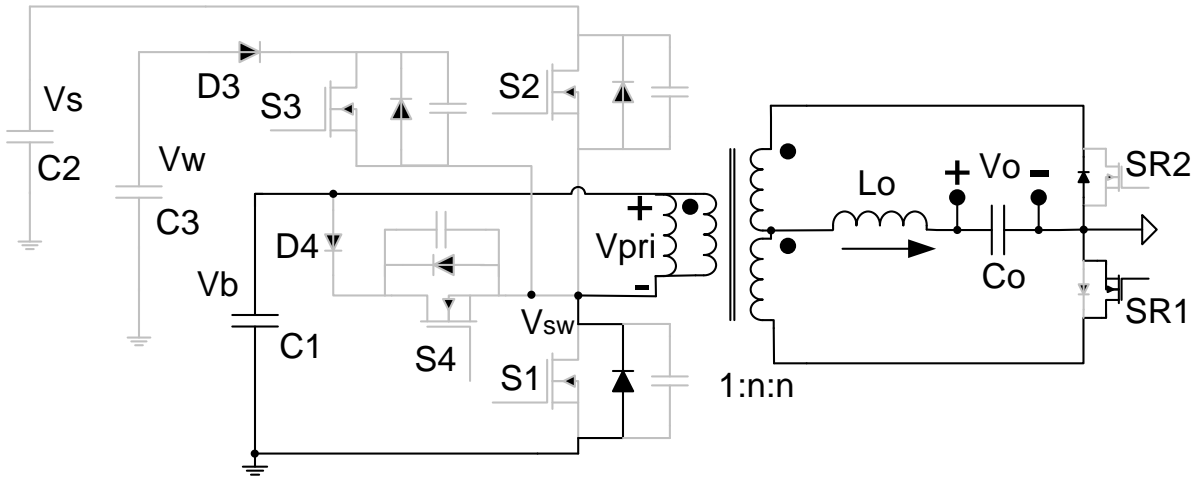
Stage 10 (t_9 - t_{10})

(j) Stage 10 operation



Stage 11 (t_{10} - t_{11})

(k) Stage 11 operation



Stage 12 (t_{11} - t_{12})

(l) Stage 12 operation

Fig. 5. 5: Operation stages of the four-port half-bridge converter

5.2.3. Steady State Analysis

Assuming an ideal converter, the steady-state voltage governing relations between different port voltages can be determined by equating the voltage-second product across the converter's two main inductors to zero. First, using volt-second balance across the primary transformer magnetizing inductance L_M , in CCM, we have:

$$V_b \cdot D_1 = (V_s - V_b) \cdot D_2 + (V_w - V_b) \cdot D_3 \quad \text{Eq. 5.1}$$

Assuming CCM operation, the voltage-second balance across the load filter inductor L_o then yields:

$$V_b \cdot D_1 + (V_s - V_b) \cdot D_2 + (V_w - V_b) \cdot D_3 = V_o / n \quad \text{Eq. 5.2}$$

Where n is the turns ratio of the transformer, V_s , V_w , V_b , V_o are the solar input, wind input, battery and output voltages, respectively.

The following equation is based on the power balance principle, by assuming a lossless converter, steady-state port currents can be related as follows:

$$V_s \cdot I_s + V_w \cdot I_w = V_b \cdot I_b + V_o \cdot I_o \quad \text{Eq. 5.3}$$

Where I_s , I_w , I_b , I_o are the average solar input, wind input, battery bidirectional, and load currents, respectively. The battery current I_b is positive during charging, and negative during discharging.

5.2.4. ZVS Analysis

ZVS of the switches S1 and S2 can be realized through the energy stored in the transformer leakage inductor, while ZVS of S3 and S4 is always maintained, because the proposed driving

scheme ensures that paralleling diodes of S3 and S4 will be forced on before the two switches turn on.

After S4 is turned off, the leakage energy is released to discharge the S1 parasitic capacitor and charge S2, S3 and S4's parasitic capacitors, to create the ZVS condition of S1. And the following condition should be satisfied:

$$\frac{1}{2} \cdot L_k \cdot (I_M + n \cdot I_o)^2 > 2 \cdot C_{oss} \cdot V_b^2 + C_{oss} \cdot V_s \cdot V_b + C_{oss} \cdot V_w \cdot V_b, \quad I_M + n \cdot I_o > 0 \quad \text{Eq. 5.4}$$

Where L_k is the transformer leakage inductance, MOSFET parasitic capacitances of S1, S2, S3 and S4 are assumed to be equal as C_{oss} , and I_M is the average transformer magnetizing current which satisfies:

$$I_b = D_1 \cdot (I_M - n \cdot I_o) + D_2 \cdot (I_M + n \cdot I_o) + D_3 \cdot (I_M + n \cdot I_o) \quad \text{Eq. 5.5}$$

Rearranging (5), we can obtain I_M as follows:

$$I_M = \frac{I_b + (D_1 - D_2 - D_3) \cdot n \cdot I_o}{D_1 + D_2 + D_3} \quad \text{Eq. 5.6}$$

After S1 is turned off, the leakage energy will charge the S1 parasitic capacitor and discharge S2, S3 and S4's parasitic capacitors to achieve ZVS for S2:

$$\frac{1}{2} \cdot L_k \cdot (I_M - n \cdot I_o)^2 > C_{oss} \cdot V_s^2 + \frac{1}{2} \cdot C_{oss} \cdot V_w^2 + \frac{1}{2} \cdot C_{oss} \cdot V_b^2, \quad I_M - n \cdot I_o < 0 \quad \text{Eq. 5.7}$$

According to equation 5.7, when the load current I_o is small and the transformer magnetizing current I_M is large, $I_M - n \cdot I_o < 0$ can not be met. In other words, ZVS of S2 will be lost. However, in most load/source conditions, ZVS of S2 is achievable.

It should be noted that ZVS of S3 and S4 can be naturally achieved if the voltage relation $V_b < V_w < V_s$ is satisfied to ensure that the paralleling diodes will always be forced on before these switches turn on. On one hand, $V_w < V_s$ is not difficult to meet since the solar port and wind port can be reversed if the wind port voltage V_w is larger than the solar port voltage V_s . Even if V_w is not always lower than V_s in the whole voltage ranges, the converter itself still works, but may lose some conduction period for the S2 branch depending on the driving overlap of S2 and S3. The solution is to change the driving scheme to avoid the S2 and S3 overlap. On the other hand, it is a step-down conversion from PV or wind port to battery port, therefore the battery voltage V_b will be always lower than the PV voltage V_s and the wind source voltage V_w .

To sum up, ZVS of all main switches can be achieved to maintain higher efficiency when the converter is operated at higher switching frequency, because of the potential savings in switching losses.

5.2.5. Circuit Design Considerations

When considering the semiconductor stresses, this modified half-bridge topology shows striking similarity to its traditional half-bridge counterpart. The major difference is that the transformer design of this four-port converter needs to allow for a dc current flow and therefore becomes similar to an inductor or a flyback transformer design. The dc biasing current rating is dictated by equation 5.6, which determines the amount of the air gap to be inserted. Other than the transformer, the circuit design and optimization technique used for the traditional half-bridge

topology can be used here for this four-port topology, which provides great convenience for the practicing engineers to implement the power stage design.

5.2.6. Semiconductor Stresses

The ideal reverse voltages seen by the switches on the primary side are:

$$\begin{aligned} V_{S1} &= V_{S2} = V_s \\ V_{S3} &= V_w \\ V_{S4} &= V_{bi} \end{aligned} \tag{Eq. 5.8}$$

Because at the starting point the wind port and battery port may not be able to build the voltage if the solar port is connected first, the voltage stresses seen by the diodes D3 and D4 are the same.

$$\begin{aligned} V_{D3} &= V_s \\ V_{D4} &= V_s \end{aligned} \tag{Eq. 5.9}$$

Assuming CCM operation, and neglecting inductor ripple currents, the rms current in the primary switches are given by:

$$\begin{aligned} I_{S1}^{rms} &= \sqrt{D_1} \cdot |nI_o - I_M| \\ I_{S2}^{rms} &= \sqrt{D_2} \cdot |nI_o + I_M| \\ I_{S3}^{rms} &= \sqrt{D_3} \cdot |nI_o + I_M| \\ I_{S3}^{rms} &= \sqrt{1 - D_1 - D_2 - D_3} \cdot |nI_o + I_M| \end{aligned} \tag{Eq. 5.10}$$

The average current of carried by D3 and D4 are:

$$I_{D3}^{avg} = D_3 \cdot (nI_o + I_M)$$

$$I_{D4}^{avg} = (1 - D_1 - D_2 - D_3) \cdot (nI_o + I_M) \quad \text{Eq. 5.11}$$

Note that it is assumed that the primary leakage inductance carries the reflected load current.

The average currents through the secondary side rectifiers are:

$$I_{SR1}^{avg} = (1 - D_2 - D_3) \cdot I_o$$

$$I_{SR2}^{avg} = (1 - D_1) \cdot I_o \quad \text{Eq. 5.12}$$

Assuming perfect snubbing (no ringing), the ideal voltage stresses seen by the rectifier diodes or synchronous switches of a center-tapped rectifier are:

$$V_{SR1} = 2n \cdot (V_s - V_{bi})$$

$$V_{SR2} = 2n \cdot V_{bi} \quad \text{Eq. 5.13}$$

5.2.7. Transformer Turns Ratio

Stress analysis clearly shows that the turns' ratio of the transformer has a major effect on circuit components stresses. A higher turns' ratio increases the circulating currents on the primary side, translating to higher switch currents and a higher dc magnetizing current. It also increases the voltage at the secondary side, applying higher reverse voltages to the rectifier devices. A minimum turns' ratio, however, is necessary to maintain the ability to achieve the targeted output voltage level with an acceptable head-room for regulation. The proper choice of turns' ratio is strongly dependent on the voltage specifications at the different ports.

5.3. Modeling and Control

This section introduces the modeling and control for the four-port converter. The modeling follows the same procedure presented in Chapter 3. There are various modes of operation for the four-port converter. Therefore, only the model under one operation mode is given in this section to provide a design example. Experiments verify the controller design and further confirm its ability to achieve tight independent control over three power processing paths.

5.3.1. Various Modes of Operation

According to whether energy sources (PV panels and Wind turbines) provide power for the load or/and battery, whether the battery supplies or absorbs power and whether the battery connects to the system, operation states of proposed four-directional converter can be classified into thirteen possible stages which are listed in Table 5.1. For the PV panels and the wind turbine, supplying power for the load or the power grid is denoted by the “1”, or by the “0”. For the battery, the “1” indicates supplying power; whereas, the “-1” indicates absorbing power and the “0” expresses disconnection. Moreover, for the load connection in the converter is expressed by the “1”, or by the “0”. Power sources of the four-port converters are various for different operation stages. In operation stage 2 and 6, power is transferred from the first input source, the second input source to the output; while the battery sinks or sources according the source condition and load profile. In the rest of stages, at least one port is left open. Therefore, the four-port converter can be treated as a three-port or a traditional two-port converter. Since mode definition for the three-port

converter has been discussed in chapter three, in this chapter, only the four-port converter operation including stage 2 and 6 will be focused.

Table 5.14 Operational Stages of the Four-port Converter

Operation Stages	PV source	Wind source	battery	load
Stage 0	0	0	1	1
Stage 1	0	1	1	1
Stage 2	1	1	1	1
Stage 3	0	1	0	1
Stage 4	1	0	0	1
Stage 5	0	1	-1	1
Stage 6	1	1	-1	1
Stage 7	1	1	0	1
Stage 8	1	0	1	1
Stage 9	1	0	-1	1
Stage 10	1	0	-1	0
Stage 11	1	1	-1	0
Stage 12	0	1	-1	0

Generally speaking, stable system operation requires the maintenance of power balance in the system. That is, in steady-state, the sum of average input power to the converter is required to equal the sum of average output power plus any power losses. This implies that, for a four-port system, the operating point of up to three ports can be tightly regulated, while the fourth port should be kept “flexible” and would operate at any point that satisfies the power balance constraints.

The choice of the flexible power port dictates the feedback control layout. It can be either of the following: the solar port, the wind port, the battery port or the output port. But normally, the output port connecting to the load is preferred to be regulated. So there are three modes to be defined.

In Battery-balanced Mode, the load voltage is tightly regulated; both the PV panel and the wind turbine operate under MPPT control to provide maximum power. The battery preserves the power balance for the system by storing unconsumed solar power or by providing the deficit during high load intervals. This mode is desirable since it can harvest the maximal power from both PV array and the wind turbine.

In Excess-insolation Mode, the load is regulated and sinks less power than is available, while the battery charge rate is limited. In this case, the battery current or voltage is regulated, while the solar array is forced to operate in its voltage-source region where it provides less power than it has available. The wind turbine is operating under MPPT to maximize the wind power harvesting.

In Excess-wind Mode, the load is regulated and sinks less power than is available, while the battery charge rate is limited. In this case, the battery current or voltage is regulated, while the wind turbine output is forced to operate in its left side I-V curve to limit the power. The PV array is operating under MPPT to maximize the solar power harvesting.

In the next section, the battery-balanced mode will be focused since it is the preferred mode of operation.

5.3.2. Control Structure

Figure 5.6 shows the control structure for the hybrid PV wind system of the battery-balanced mode. Three feedback controllers are as follows: a solar voltage regulator (SVR), a wind voltage regulator (WVR), and an output voltage regulator (OVR).

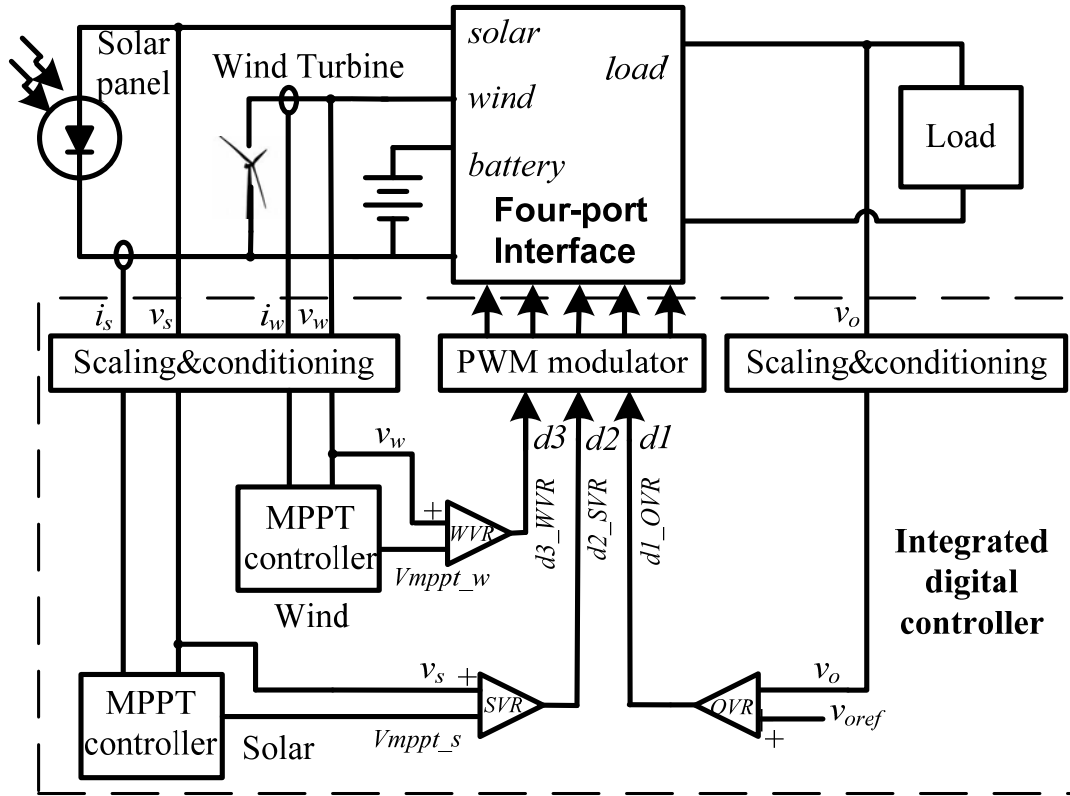


Fig. 5. 6: A possible control structure to achieve MPPT for the PV panel and the wind turbine, meanwhile maintaining output voltage regulation. OVR, SVR and WVR loops are to control d_1 , d_2 and d_3 , respectively.

The OVR loop is simply a voltage feedback loop closed around the load port and duty cycle d_1 is used as its control input. The SVR loop is used to regulate the PV panel voltage to its reference

value, which is provided by an MPPT controller. The reference value represents an estimate of the optimal operating PV voltage with duty cycle d_2 is used as its control input. The WVR loop is taking a very similar structure to SVR, except that its voltage reference represents the optimal operating voltage of the rectified wind turbine output voltage. The WVR loop is made to control d_3 . This control strategy allows the load voltage to be tightly regulated while maximizing the PV and wind power harvesting. In this system, the battery storage plays the significant role of balancing the system energy by injecting power at heavy loads and absorbing excess power when available PV and wind power exceeds the load demand.

5.3.3. Converter Modeling

In order to design the SVR, WVR and OVR controllers, a small signal model of the four port converter is desired. The detailed modeling procedure can refer to [19], which is proposed for a three-port converter. For this four-port converter, the general modeling procedure is very similar to [19]. Therefore, to avoid unnecessary repetition, only a brief introduction is given here. First, state-space equations for five energy storage element during the four main circuit stages are developed. For the above-mentioned mode of operation, these include the solar side capacitor C_s , the wind side capacitor C_w , the transformer magnetizing inductor L_m , the output inductor L_o , and the output capacitor C_o . In the next step, state-space equations in the four main circuit stages (corresponding to the turn-on of four main switches) will be averaged, and then applied with the small signal perturbation. Finally, the first order small signal perturbation components will be collected to form the matrices A and B , which actually represent the converter power stage

model. It should be noted that the symbolic derivation of these transfer functions is fairly tedious. Alternatively, the dynamics of the plant can be calculated by computer software like MATLAB[®]. The resultant state-space averaging model takes the following form:

$$dX / dt = A \cdot X + B \cdot U, Y = I \cdot X \quad \text{Eq. 5.15}$$

$$A = \begin{bmatrix} -\frac{1}{R_s \cdot C_s} & 0 & \frac{-D_2}{C_s} & \frac{-n \cdot D_2}{C_s} & 0 \\ 0 & -\frac{1}{R_w \cdot C_w} & \frac{-D_3}{C_w} & \frac{-n \cdot D_3}{C_w} & 0 \\ \frac{D_2}{L_M} & \frac{D_3}{L_M} & 0 & 0 & 0 \\ \frac{n \cdot D_2}{L_o} & \frac{n \cdot D_3}{L_o} & 0 & 0 & \frac{-1}{L_o} \\ 0 & 0 & 0 & \frac{1}{C_o} & -\frac{1}{R \cdot C_o} \end{bmatrix}, \quad X = \begin{bmatrix} \hat{v}_s \\ \hat{v}_w \\ \hat{i}_{Lm} \\ \hat{i}_{Lo} \\ \hat{v}_o \end{bmatrix}$$

$$B = \begin{bmatrix} 0 & \frac{-I_{Lm} - n \cdot V_o / R}{C_s} & 0 \\ 0 & 0 & \frac{-I_{Lm} - n \cdot V_o / R}{C_w} \\ -\frac{V_b}{L_M} & \frac{V_s - V_b}{L_M} & \frac{V_w - V_b}{L_M} \\ \frac{n \cdot V_b}{L_o} & \frac{n \cdot (V_s - V_b)}{L_o} & \frac{n \cdot (V_w - V_b)}{L_o} \\ 0 & 0 & 0 \end{bmatrix}, \quad U = \begin{bmatrix} d1 \\ d2 \\ d3 \end{bmatrix}$$

$$\text{Eq. 5.16}$$

Where X is a matrix containing the state variables V_s , V_w , i_{Lm} , i_{Lo} , and V_o , U is a matrix containing the control inputs d_1 , d_2 and d_3 , Y is a matrix containing the system outputs, and I is the identity matrix.

With matrices A and B , transfer functions for PV, wind and output voltages to different duty-cycle values can be extracted according to equation 5.16. For example, $G(s)(5,1)$ represents the 5th state variable V_o and the 1st control variable d_1 , thus equals to open loop transfer function of

$V_o(s)/d_I(s)$. So the row number denotes the sequence of state variable, and the column number denotes that of control input.

$$G = (s \cdot I - A)^{-1} \cdot B,$$

$$g_{11} = G(s)(5,1), \quad g_{21} = G(s)(1,1), \quad g_{31} = G(s)(2,1)$$

$$g_{12} = G(s)(5,2), \quad g_{22} = G(s)(1,2), \quad g_{32} = G(s)(2,2)$$

$$g_{13} = G(s)(5,3), \quad g_{23} = G(s)(1,3), \quad g_{33} = G(s)(2,3)$$

Eq. 5.17

Figure 5.7 illustrates the small signal model diagram when closing SVR, WVR and OVR loops, which consists of the converter model and the feedback controllers. F_M represents the PWM modulator gain and different K_V values represent different voltage signal sensing gains, which can be treated as the fixed proportional values.

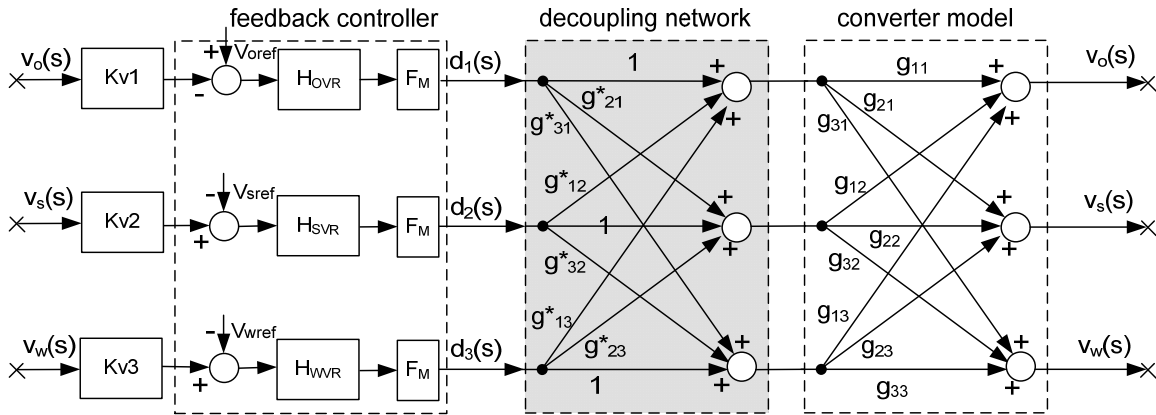


Fig. 5. 7: Small signal model diagram, control inputs and outputs are decoupled to enable separate controller design. The far right signals are routed to the far left ones in this diagram.

V_{sref} , V_{wref} and V_{oref} are the references for solar, wind and output voltages, respectively. H_{SVR} ,

H_{WVR} and H_{OVR} are the compensators need to be designed.

5.3.4. Decoupling Method

As can be seen from Figure 5.7, the three control loops are coupled with each other, which make it difficult to design close loop compensators for each control loop. Therefore a decoupling network as shadowed in Figure 5.7 is introduced so that the control loops can be designed independently with different control loop bandwidth requirement. Since output port voltage regulation requirement is the most stringent of the three and the PV panel and wind turbine characteristics are relatively slower, the SVR loop is designed to have a one decade lower bandwidth than that of OVR. Moreover, WVR bandwidth can be set to be lower than that of SVR to further reduce SVR and WVR loop interactions, since the mechanical behavior of wind blades is slower than the photovoltaic behavior of PV panels.

The derivation of decoupling network G^* is described as follows: the state vector matrix X can be written as $X = G \cdot U^*$, where U^* is the modified input vector made up of duty cycles U , $U^* = G^* \cdot U$. Therefore, $X = G \cdot G^* \cdot U$. According to modern control theory, our goal is to make $G \cdot G^*$ a diagonal matrix to allow one control input to determine one output independently. So based on $G^* = G^{-1} \cdot X \cdot U^{-1}$, the decoupling matrix G^* can be derived and simplified as:

$$G^* = \begin{bmatrix} g_{11}^* & g_{12}^* & g_{13}^* \\ g_{21}^* & g_{22}^* & g_{23}^* \\ g_{31}^* & g_{32}^* & g_{33}^* \end{bmatrix} = \begin{bmatrix} 1 & \frac{g_{13} \cdot g_{32} - g_{12} \cdot g_{33}}{g_{11} \cdot g_{33} - g_{13} \cdot g_{31}} & \frac{g_{12} \cdot g_{23} - g_{13} \cdot g_{22}}{g_{11} \cdot g_{22} - g_{12} \cdot g_{21}} \\ \frac{g_{23} \cdot g_{31} - g_{21} \cdot g_{33}}{g_{22} \cdot g_{33} - g_{23} \cdot g_{32}} & 1 & \frac{g_{13} \cdot g_{21} - g_{11} \cdot g_{23}}{g_{11} \cdot g_{22} - g_{12} \cdot g_{21}} \\ \frac{g_{21} \cdot g_{32} - g_{22} \cdot g_{31}}{g_{22} \cdot g_{33} - g_{23} \cdot g_{32}} & \frac{g_{12} \cdot g_{31} - g_{11} \cdot g_{32}}{g_{11} \cdot g_{33} - g_{13} \cdot g_{31}} & 1 \end{bmatrix} \quad Eq. 5.18$$

Now the cross-coupled three-loop control system is decoupled into three independent single-loop subsystems. The system can then be controlled using independent loop controllers and each compensator can be designed separately as well. For example, the OVR controller can then be designed based on the following plant transfer function:

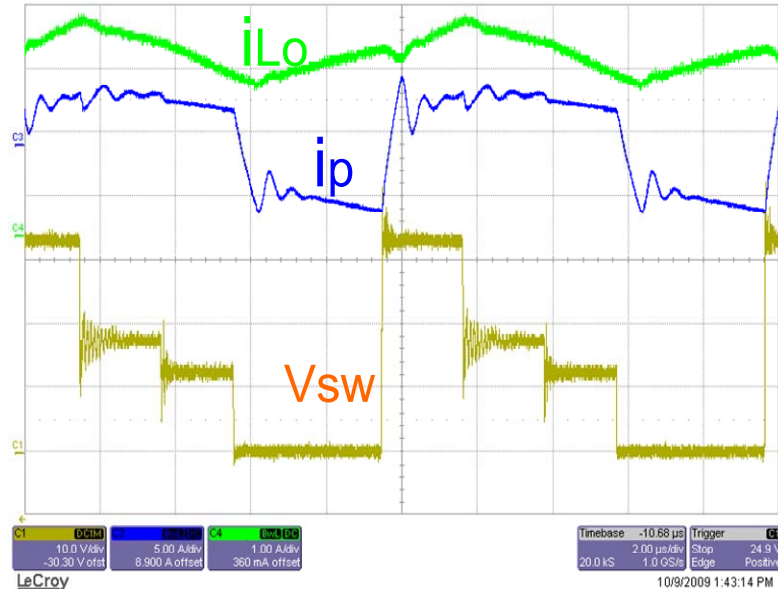
$$v_o(s)/d_1(s) = g_{11} + g_{12} \cdot \frac{g_{23} \cdot g_{31} - g_{21} \cdot g_{33}}{g_{22} \cdot g_{33} - g_{23} \cdot g_{32}} + g_{13} \cdot \frac{g_{21} \cdot g_{32} - g_{22} \cdot g_{31}}{g_{22} \cdot g_{33} - g_{23} \cdot g_{32}} \quad Eq. 5.19$$

Similarly, SVR and WVR controllers can also be designed once their decoupled plant transfer functions are derived. The controller design follows the traditional control law, and is suggested to meet the bandwidth limitation requirement mentioned above, while having enough phase margins to prevent potential instability. The controller normally uses the PI or PID compensation, the design methodology has been well known to practicing engineers, therefore is beyond the scope of this dissertation.

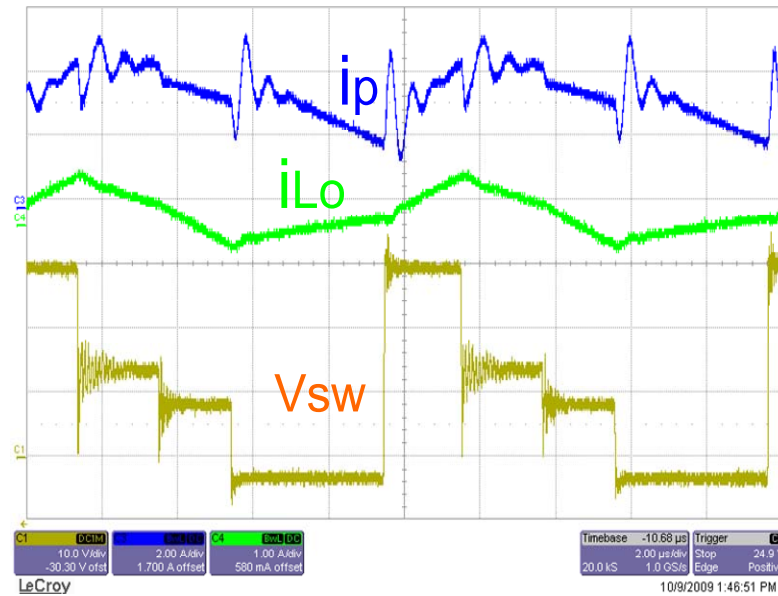
5.4. Experimental Results

A four-port DC/DC converter prototype is built to verify the circuit operation. The circuit parameters are: solar port, 30-40V/1.5A; wind port, 20-30V/1.5A; battery port, 12-18V/3A; output port, 12V/3.3A. The switching frequency is 100 kHz, and it is implemented by the digital control to achieve the close loop regulation.

Figure 5.8 gives the steady state waveforms when loading the output port (a) and loading the battery port (b). The switch node voltage V_{sw} shows a four-stage wave shape, corresponding to the turn-on of four main switches with four different voltage levels. In addition, there is no CCM and DCM transition for the output inductor current i_{Lo} , which avoids the sharp change of plant dynamic characteristics and simplifies the output voltage feedback controller design. The transformer magnetizing current i_p is determined by both the reflected output current and the battery current.



(a)



(b)

Fig. 5. 8: Steady state waveforms: (a) Loading the output port when the battery current is zero;

(b) Loading the battery port when the output current is zero.

Figure 5.9 and Figure 5.10 show the gating signal V_{gs} and switching node V_{sw} waveforms of the switches S1 and S2. Since S3 and S4 have ZVS under all conditions as mentioned earlier, only S1 and S2 waveforms are presented here. The conclusion is that all four main switches can achieve ZVS, because they all turn on after their V_{ds} goes to zero.

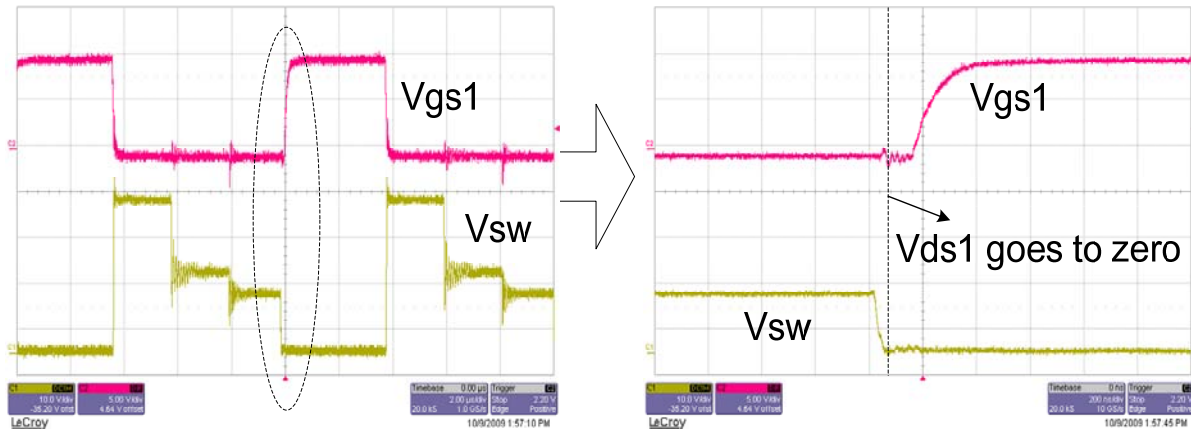


Fig. 5. 9: V_{gs} and V_{sw} of the switch S1

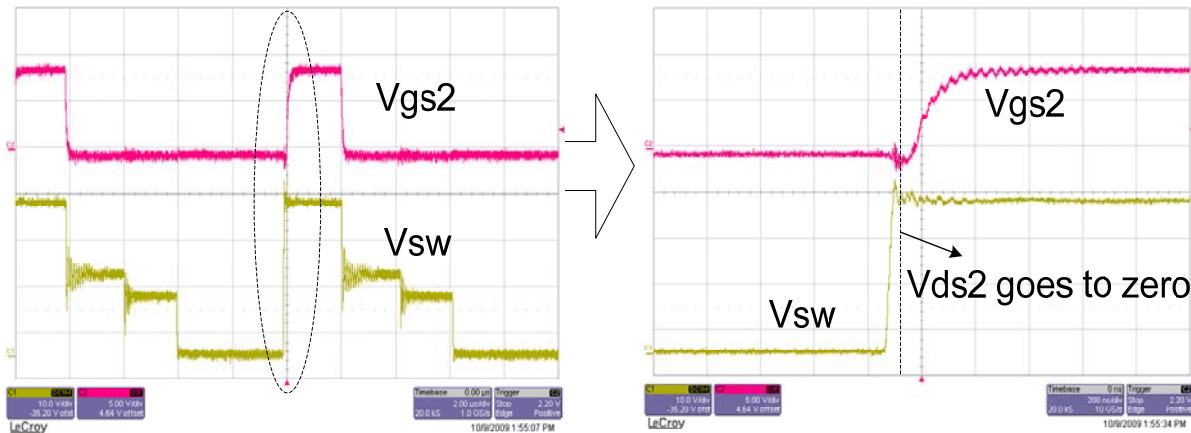


Fig. 5. 10: V_{gs} and V_{sw} of the switch S2

Table 5.2 shows eight different load and source combinations with each one of them to be either 10% or 90% load/source condition, while the battery port provides the power balance. The test setup is realized by connecting the solar port and wind port of the converter to two independent PV array simulators instead of the solar panel and the wind turbine. Then two different I-V curves are assigned for the solar and wind port, and the DSP code is tuned so that the SVR and WVR voltage references are at 10% or 90% rated current point. As a result, two sources will have four different combinations. A battery is connected to sink the excess power or source the deficit power, and the load is set to sink either 10% or 90% rated output current. So all together, there are eight different conditions for one load and two sources as described in Table 5.2.

Table 5.20 Different Load/Source Current Level Conditions

	Load/Source Current Level Conditions (%)		
	$V_s=35.6V$	$V_w=28.2V$	$V_o=12V$
Case1	10	10	90
Case2	90	10	90
Case3	10	90	90
Case4	90	90	90
Case5	90	10	10
Case6	10	90	10
Case7	90	90	10
Case8	10	10	10

Figure 5.11 depicts all three port voltages under different load/source conditions. The cross regulation of V_s , V_w and V_o are 0.5%, 0.6% and 1.1%, respectively. Figure 5.12 shows the efficiency curve under different load/source conditions as in Table 5.2. The highest efficiency is

93.9% when most of the power is exchanged within the primary side from the solar and wind port to the battery port, the reason is that this operation has minimal transformer losses.

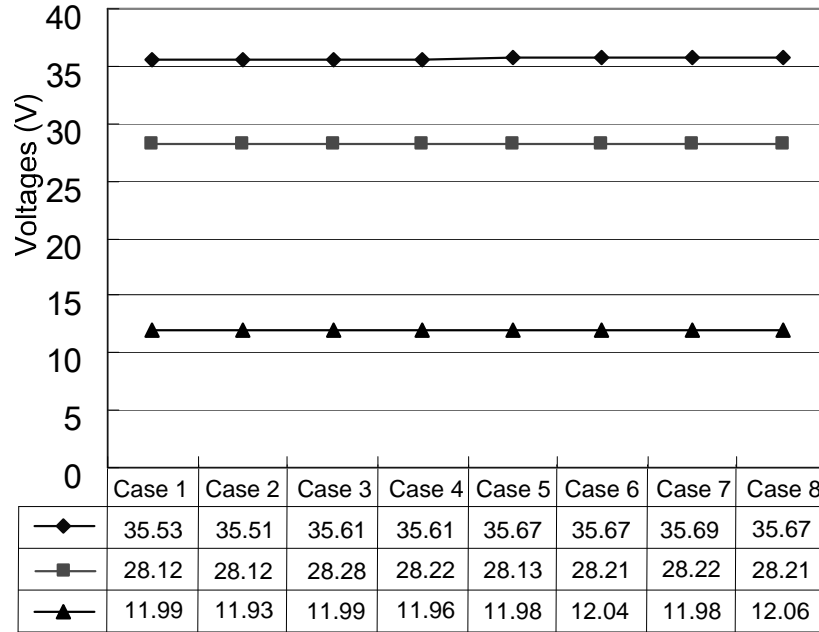


Fig. 5. 11: Solar port, wind port, output port voltages under different load/source conditions.

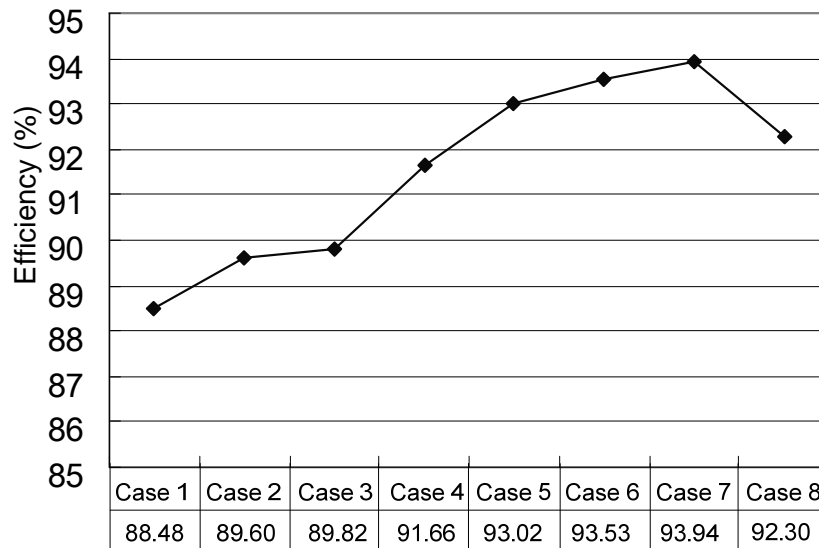


Fig. 5. 12: Efficiency under different load/source conditions

Figure 5.13 shows the transient response of the PV voltage, wind voltage and output voltage to a load transient between 0.33A and 3A, when SVR, WVR and OVR loops are closed. In terms of the settling time, the output voltage transient response is much faster than that of the solar or the wind port, while the transient of the solar port is slightly faster than that of the wind port. Because OVR bandwidth is ten times larger than that of SVR, and SVR bandwidth is four times larger than that of WVR. As shown in Figure 5.14, Figure 5.15 and Figure 5.16, the bandwidth designed for OVR, SVR and WVR are 2 kHz, 200 Hz and 50 Hz, respectively. The reason for this bandwidth limitation is that the output dynamics is the most stringent of the three, while PV panel and wind turbine dynamics are relatively slow. The above-mentioned control loop bandwidth limitation is helpful to reduce the loop interactions.

Although the reference values of V_{sref} and V_{wref} are given as the fixed values rather than being constantly updated by the MPPT controllers, these experiments provide a quick approximation that MPPT of the PV panel and the wind turbine SVR can be achieved at the same time, while maintaining a regulated output voltage.

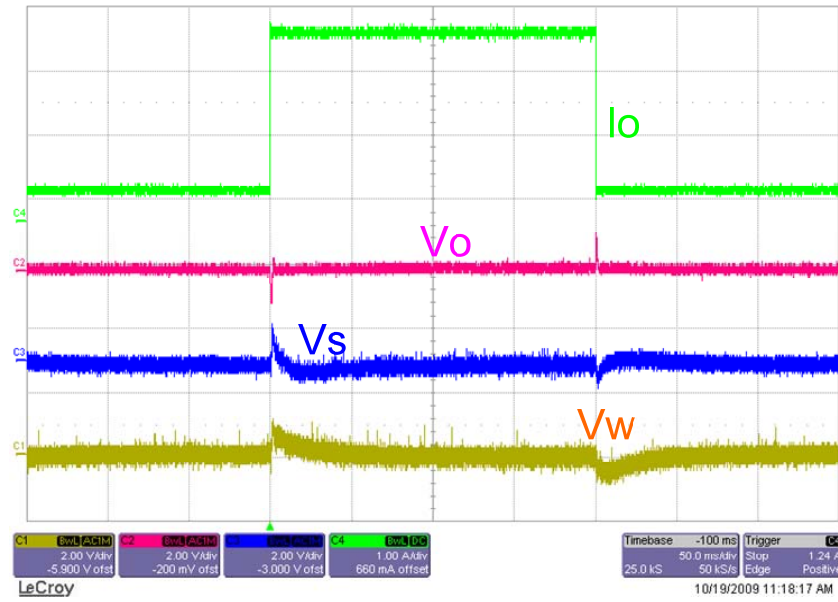


Fig. 5. 13: Transient response of solar, wind and output voltages when the load is perturbed by a step change between 10% and 90% rated output current.

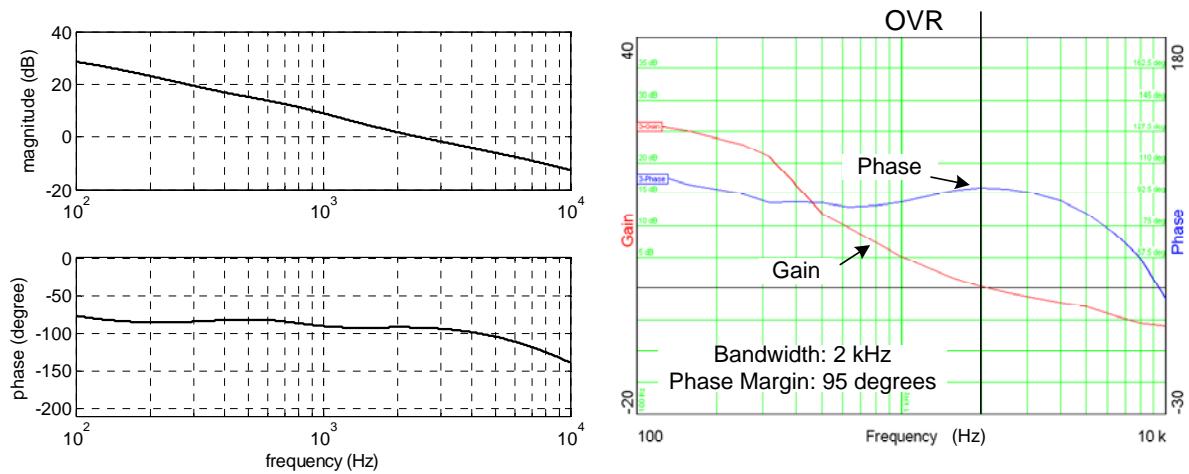


Fig. 5. 14: OVR loop bode plots: (a) prediction; (b) experiment.

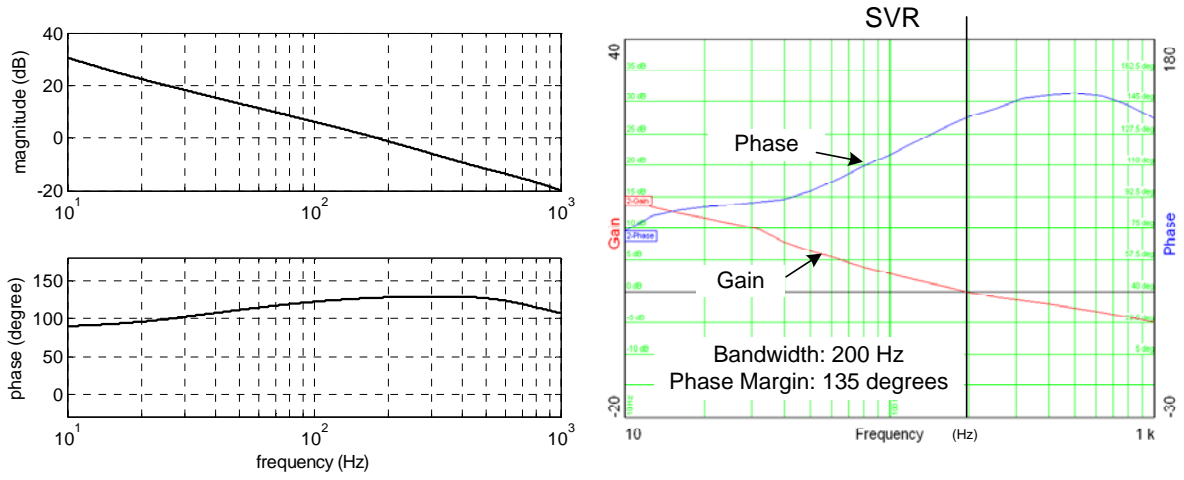


Fig. 5. 15: SVR loop bode plots: (a) prediction; (b) experiment.

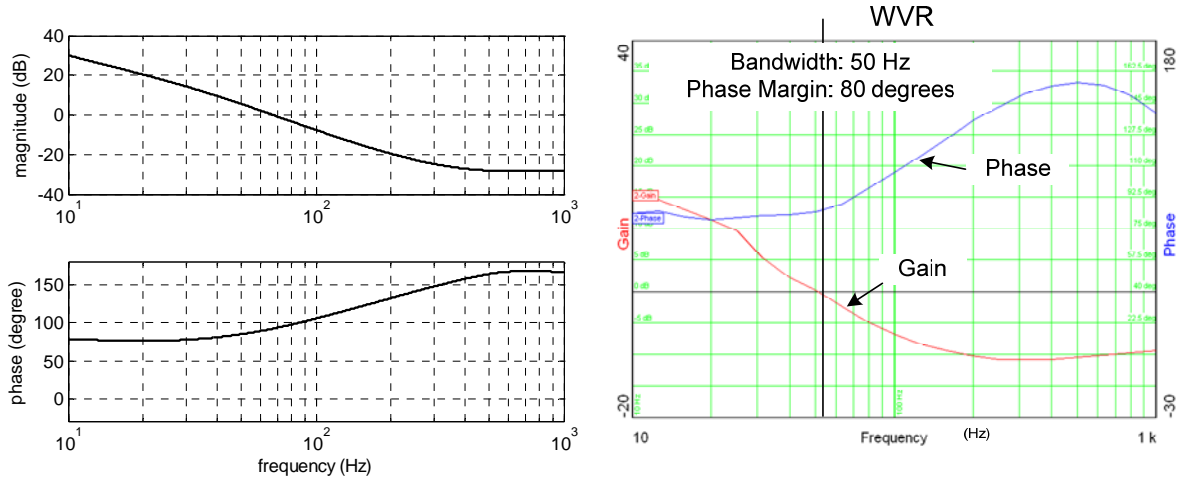


Fig. 5. 16: WVR loop bode plots: (a) prediction; (b) experiment.

5.5. Extension into Multi-port Converter

In the proposed four-port DC/DC converter, there are two input switch branches, which enable two sources. However, the number of the unidirectional switch branches is not limited. Addition

of a half-bridge upper switch plus a diode will provide one more input port to interface another renewable energy source. Figure 5.17 is a generalized multi-port DC/DC converter with n input ports, one bidirectional port and one isolated output port.

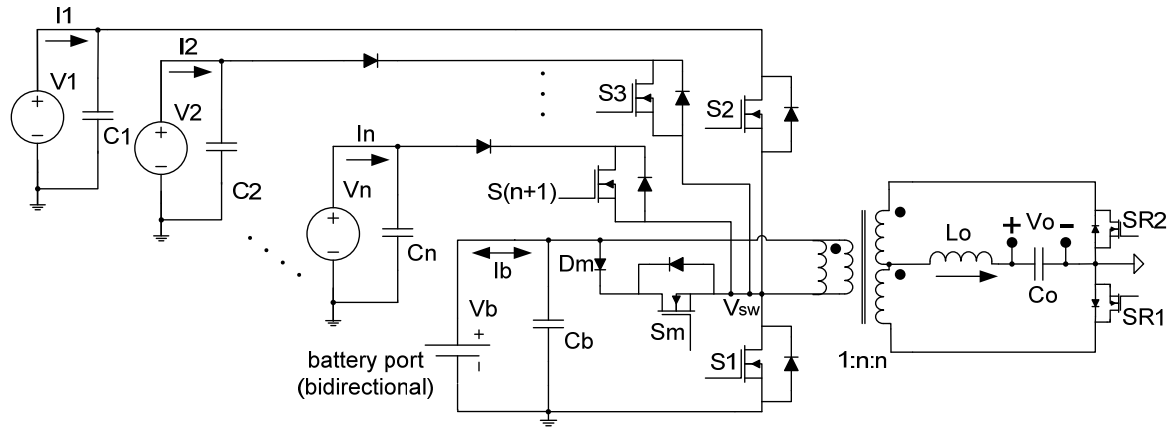


Fig. 5. 17: Extension of the proposed multi-port DC/DC converter

CHAPTER 6: CONCLUSIONS AND FUTURE WORK

This dissertation discusses the design and implementation of an integrated multi-port converter solution for the satellite platform power system and the hybrid sources renewable system. A general modeling procedure is proposed to derive the multi-port converter model. Various control aspects like system control structure, MPPT, battery charging, etc, are discussed to achieve the power management control. The interesting topic of current sharing for multi-port converters is also introduced. Finally, a multi-port converter topology based on traditional half-bridge converter is proposed to interface various renewable sources while maintaining a regulated output voltage.

6.1. *Major Contributions*

The major contributions in this dissertation are summarized as follows.

1. A modeling procedure is proposed to derive the small signal model of the multi-port converter. The modeling is based on state-space averaging method. Various modes of operation have to be defined first, and then the state variables should be carefully chosen to reveal the different ports' dynamic characteristics. Control loops are cross coupled with each other due to the power stage integration issue, therefore proper decoupling method is proposed to allow a separate controller for each power port. Close loop controller design guidance is provided based on the requirement of each power port's characteristics.
2. The modular structure and the current sharing control strategy is proposed to achieve operation of paralleled three-port converters, with MPPT for the solar port, battery charging

control for the battery port and bus regulation for the output port. A dual loop current sharing control structure is identified to be suitable for multi-port converters, because of the convenient decoupling feature of its current sharing loop and voltage regulation loop. Then, a hybrid current sharing control structure which takes advantage of both active and passive current sharing methods is proposed to avoid the drawback of current sharing bus in the active current sharing method while achieving better dynamics than the passive method.

3. The system level control strategy is proposed to achieve the multi-objective power management control goals. For this control strategy, the maximum power harvesting of the renewable sources like solar array or wind turbine will be guaranteed under different conditions of battery state of charge and load profiles. The control strategy is not only suitable for single three-port converters, but also can be extended to be applying for multiple three-port channels, with each channel one of the distributed units.

4. A four-port half-bridge topology is proposed for hybrid renewable sources with a battery backup. The topology features low component count and ZVS for all main switches. One isolation port is naturally available due to the half-bridge transformer. Modification based on the traditional half-bridge topology makes it convenient for the practicing engineers to follow the power stage design. The circuit operation of this converter and its control system is experimentally verified. For the hybrid PV wind system, the proposed control structure is able to achieve maximum power harvesting for PV and/or wind power sources, meanwhile maintaining a regulated output voltage. Although the proposed four-port converter only has two input ports, it can be extended to have n input ports.

6.2. Future Work

The promising results presented here warrant future investigation. Suggested future work is as follows:

1. Derivation of more topologies for different applications. This half-bridge based topology is suitable for low to medium power applications, while full-bridge based multi-port converters will be more suitable for relatively high power applications.
2. For this half-bridge based multi-port converter, the soft switching range can still be improved to allow higher frequency designs to further reduce the converter size. The high side switch may lose ZVS when the battery is charging. Introducing some soft-switching cells to the topology may solve this problem.
3. The modular design of the multi-port converter is an interesting topic. When multi-port converters are paralleled together, it is very challenging to design the active current sharing controllers since there are so many control loops coupled with each other. It is very difficult to analyze and decouple the control loops, especially considering the power stage non-identities. Therefore, a clear and easy to follow design procedure is required to guide the design of paralleled multi-port converters.
4. The standard power interface or Power Electronics Building Blocks (PEBB) is a promising concept, because a configurable “on-the-fly” converter can be told its operating parameters and its function via software, can be useful in many applications and offers the potential for a standardized interface. Based on PEBB concept, two three-port converters can form a four-port or five-port converter depending on how many ports of the three-port converter are connected together. Therefore, the

standardization and miniaturization of the multi-port converter is much desired. At least for the proposed half-bridge converter prototype, a planar transformer can be used to lower the board height since the transformer is the highest component. And light load efficiency can be significantly improved by using some advanced techniques like mode hopping and pulse skipping.

5. The control strategy still can be enhanced in many aspects. Proposed battery charging algorithm includes two controllers, the constant current controller and the constant voltage controller. Pre-charging and float-charging stages may also be included to better condition the battery and extend its service lifespan. Additionally, an algorithm suitable for various types of battery chemistries is desired. For the four-port converter, only one mode of operation is discussed, while the other modes of operation still needs specific consideration in various conditions like when only one of the renewable sources is available or one MPPT function has to be disabled because of limited load demanding.

REFERENCES

- [1] A. Capel, "The power system of the multimedia constellation satellite for the Skybridge Missions," in Proc. IEEE Power Electronics Specialists Conf., 1998, pp. 1913-1930.
- [2] H.W. Brandhorst, M.J. O'Neill, M. Eskenazi, "Photovoltaic options for increased satellite power at lower cost," in Proc. IEEE Photovoltaic Energy Conversion, 2003, pp. 849 - 852.
- [3] S. Jang, J. Choi, "Energy balance analysis of small satellite in Low Earth Orbit (LEO)," in Proc. IEEE Power and Energy Conference, 2008, pp. 967 - 971.
- [4] R. D. Middlebrook and S. Cuk, "A General Unified Approach to Modeling Switching-Converter Power Stages," International Journal of Electronics, vol. 42, pp.521 - 550, June 1977.
- [5] S. Cuk, "Modeling, Analysis, and Design of Switching Converters," Ph.D. thesis, California Institute of Technology, November 1976.
- [6] A. Di Napoli, F. Crescimbeni, L. Solero, F. Caricchi and F.G. Capponi, "Multiple-input DC-DC Power Converter for Power-flow Management in Hybrid Vehicles," in Proc. IEEE Industry Application Conf., 2002, pp. 1578 - 1585.
- [7] W. Jiang, B. Fahimi, "Multi-port Power Electric Interface for Renewable Energy Sources," in IEEE 2009 Applied Power Electronics Conference, 2009, pp.347-352.
- [8] W. G. Imes, and F. D. Rodriguez, "A Two-Input Tri-State Converter for Spacecraft Power Conditioning," in Proc. AIAA International Energy Conversion Engineering Conf., 1994, pp. 163 - 168.

- [9] F. D. Rodriguez, and W. G. Imes, "Analysis and Modeling of A Two-Input DC/DC Converter with Two Controlled Variables and Four Switched Networks," in Proc. AIAA International Energy Conversion Engineering Conf., 1994, pp. 322 - 327.
- [10] B. G. Dobbs, and P. L. Chapman, "A Multiple-Input DC-DC Converter Topology, " in IEEE Power Electronics Letters, vol. 1, pp. 6-9, March 2003.
- [11] N. D. Benavides, and P. L. Chapman, "Power Budgeting of a Multiple-Input Buck-Boost Converter, " IEEE Trans. Power Electronics, vol. 20, pp. 1303-1309, November 2005.
- [12] H. Matsuo, W. Lin, F. Kurokawa, T. Shigemizu and N. Watanabe, "Characteristics of the Multiple-Input DC-DC Converter, " IEEE Trans. Industrial Applications, vol. 51, pp. 625 - 631, June 2004.
- [13] L. Solero, F. Caricchi, F. Crescimbeni, O. Honorati, and F. Mezzetti, "Performance of A 10 kW Power Electronic Interface for Combined Wind/PV Isolated Generating Systems," in Proc. IEEE Power Electronics Specialists Conf., 1996, pp. 1027-1032.
- [14] L. Solero, A. Lidozzi, and J.A. Pomilio, "Design of Multiple-Input Power Converter for Hybrid Vehicles," in Proc. IEEE Applied Power Electronics Conf., 2004, pp. 1145 - 1151.
- [15] Gui-jia Su, and F.Z. Peng, "A Low Cost, Triple-Voltage Bus DC-DC Converter for Automotive Applications," in Proc. IEEE Applied Power Electronics Conf., 2005, pp.1015 - 1021.
- [16] F. Z. Peng, H. Li, G. J. Su and J. S. Lawler, "A New ZVS Bidirectional dc-dc Converter for Fuel Cell and Battery Applications, " IEEE Trans. Power Electronics, vol. 19, pp. 54-65, January 2004.

- [17] H. Tao, A. Kotsopoulos, J.L. Duarte, M.A.M Hendrix, "Multi-Input Bidirectional DC-DC Converter Combining DC-link and Magnetic-coupling for Fuel Cell Systems," in Proc. IEEE Industry Applications Conf., 2005, pp. 2021- 2028.
- [18] Y. M. Chen, Y. C. Liu, and F. Y. Wu, "Multi-input DC/DC Converter Based On the Multiwinding Transformer for Renewable Energy Applications, " IEEE Trans. Industrial Applications, vol. 38, pp. 1096 - 1104, August 2002.
- [19] M. Michon, J.L. Duarte, M. Hendrix, and M.G. Simoes, "A Three-Port Bi-directional Converter for Hybrid Fuel Cell Systems," Proc. IEEE Power Electronics Specialists Conf., 2004, pp. 4736 - 4742.
- [20] H. Matsuo, W. Lin, F. Kurokawa, T. Shigemizu, and N. Watanabe, "Characteristic of the Multiple-Input DC-DC Converter," IEEE Trans. Industrial Electronics, 2004, vol. 51, pp. 625 - 631.
- [21] H. Al-Atrash, F. Tian, I. Batarseh, "Tri-Modal Half-Bridge Converter Topology for Three-Port Interface," IEEE Trans. Power Electronics, vol. 22, pp. 341 - 345, January 2007.
- [22] Z. Qian, O. Abdel-Rahman, J. Reese, H. Al-Atrash, I. Batarseh, "Dynamic Analysis of Three-Port DC/DC Converter for Space Applications," in Proc. IEEE Applied Power Electronics Conf., 2009, pp.28 - 34.
- [23] D. Liu, H. Li, "A ZVS Bi-Directional DC-DC Converter for Multiple Energy Storage Elements," IEEE Trans. Power Electronics, vol. 21, pp. 1513 - 1517, September 2006.

- [24] C. Zhao, S.D. Round and J.W. Kolar, "An Isolated Three-Port Bidirectional DC-DC Converter with Decoupled Power Flow Management," IEEE Trans. Power Electronics, vol. 21, pp. 2443 - 2453, September 2008.
- [25] H. Tao, A. Kotsopoulos, J. L. Duarte and M. A. M. Hendrix, "Transformer-Coupled Multiport ZVS Bidirectional DC-DC Converter With Wide Input Range, " IEEE Trans. Power Electronics, vol. 23, pp.771 - 781, March 2008.
- [26] J. L. Duarte, M. Hendrix, and M. G. Simoes, "Three-Port Bidirectional Converter for Hybrid Fuel Cell Systems, " IEEE Trans. Power Electronics, vol. 22, pp.480 - 487, March 2007.
- [27] H. Al-Atrash, and I. Batarseh, "Boost-Integrated Phase-Shift Full-Bridge Converters for Three-Port Interface," in Proc. IEEE Power Electronics Specialists Conf., 2007, pp. 2313 - 2321.
- [28] H. Al-Atrash, M. Pepper, and I. Batarseh, "A Zero-Voltage Switching Three-Port Isolated Full-Bridge Converter," in Proc. IEEE International Telecommunications Energy Conf., 2006, pp. 411- 418.
- [29] H. Tao; A. Kotsopoulos; J.L. Duarte; M.A.M., Hendrix, "Family of Multiport Bidirectional DC-DC Converters," in Proc. IEEE Power Electronics Specialists Conf., 2008, pp. 796 - 801.
- [30] J. A. Abu-qahouq; H. Mao; H. J. Al-atrash; I. Batarseh, "Maximum Efficiency Point Tracking (MEPT) Method and Digital Dead Time Control Implementation," IEEE Trans. Power Electronics, vol. 21, pp. 1273 - 1281, September 2006.

- [31] H. Li; D. Liu; F. Peng; G. Su, "Small Signal Analysis of A Dual Half Bridge Isolated ZVS Bi-directional DC-DC converter for Electrical Vehicle Applications," in Proc. IEEE Power Electronics Specialists Conf., 2005, pp. 2777 - 2782.
- [32] H. Al-Atrash; I. Batarseh, "Digital Controller Design for A Practicing Power Electronics Engineer," in Proc. IEEE Applied Power Electronics Conf., 2007, pp. 34 - 41.
- [33] H. Mao; J. Abu-Qahouq; S. Luo; I. Batarseh, "Zero-Voltage-Switching Half-bridge DC-DC Converter with Modified PWM Control Method," IEEE Trans. Power Electronics, vol. 19, pp.947 - 958, July 2004.
- [34] D. P. Hohm; M. E. Ropp, "Comparative Study of Maximum Power Point Tracking Algorithms Using An Experimental, Programmable, Maximum Power Point Tracking Test Bed," in Proc. IEEE Photovoltaic Specialists Conf., 2000, pp. 1699 - 1702.
- [35] W. Wu, N. Pongratananukul, W. Qiu, K. Rustom, T. Kasparis, and I. Batarseh, "DSP-based Multiple Peak Power Tracking for Expandable Power System," in Proc. IEEE Applied Power Electronics Conf., 2003, pp.525 - 530.
- [36] R. W. Erickson and D. Maksimovic, Fundamentals of Power Electronics, 2nd edition. Boston, MA: Kluwer, 2000, Chap. 7.
- [37] D. C. Hamill, "Generalized Small-signal Dynamical Modeling of Multi-Port DC-DC Converters," in Proc. IEEE Power Electronics Specialists Conf., 1997, pp. 421 - 427.
- [38] H. Al-Atrash, I. Batarseh, K. Rustom, "Statistical Modeling of DSP-based Hill-climbing MPPT Algorithms in Noisy Environments," in Proc. IEEE Applied Power Electronics Conf., 2005, pp.1773 - 1777.

- [39] Y. Liu, and Y. M. Chen, "A Systematic Approach to Synthesizing Multi-Input DC–DC Converters," IEEE Trans. Power Electronics, vol. 24, pp. 116 - 127, January 2009.
- [40] A. Khaligh, J. Cao and Y. Lee, "A Multiple-Input DC–DC Converter Topology," IEEE Trans. Power Electronics, vol. 24, pp. 862 - 868, March 2009.
- [41] A. Kwasinski, "Identification of Feasible Topologies for Multiple-Input DC-DC Converters," IEEE Trans. Power Electronics, vol. 24, pp. 856 - 861, March 2009.
- [42] G. Su, and L. Tang, "A Reduced-Part, Triple-Voltage DC-DC Converter for EV/HEV Power Management," IEEE Trans. Power Electronics, vol. 24, pp. 2406 - 2410, October 2009.
- [43] H. Tao, J.L. Duarte, M.A.M Hendrix, "Three-Port Triple-Half-Bridge Bidirectional Converter With Zero-Voltage Switching," IEEE Trans. Power Electronics, vol. 23, pp. 782 - 792, March 2008.
- [44] Z. Qian, O. Abdel-Rahman, M. Pepper, I. Batarseh, "Analysis and Design for Paralleled Three-port DC/DC Converters with Democratic Current Sharing Control," in Proc. IEEE Energy Conversion Congress and Exposition, 2009, pp. 1375-1382.
- [45] R. W. Erickson and D. Maksimovic, Fundamentals of Power Electronics, 2nd edition. Boston, MA: Kluwer, 2000, Chap. 7.
- [46] H. Mao; J. Abu-Qahouq; S. Luo; I. Batarseh, "Zero-Voltage-Switching Half-bridge DC-DC Converter with Modified PWM Control Method," IEEE Trans. Power Electronics, vol. 19, pp. 947 - 958, July 2004.

- [47] Y. Panov, J. Rajagopalan and F.C. Lee, "Analysis and Design of N Parallel DC-DC Converters with Master-Slave Current-Sharing Control," in Proc. IEEE Applied Power Electronics Conf., 1997, pp. 436-442.
- [48] J. Sun, Y. Qiu, B. Lu, M. Xu, F.C. Lee, W.C. Tipton, "Dynamic Performance Analysis of Outer-loop Current Sharing Control for Paralleled DC-DC Converters," in Proc. IEEE Applied Power Electronics Conf., 2005, pp. 1346 - 1352.
- [49] W. Wu, N. Pongratananukul, W. Qiu, K. Rustom, T. Kasparis, I. Batarseh, "DSP-based multiple peak power tracking for expandable power system," in Proc. IEEE Applied Power Electronics Conf., 2003, pp. 525-530.
- [50] Y. Panov and M.M. Jovanovic, "Stability and Dynamic Performance of Current-Sharing Control for Paralleled Voltage Regulator Modules," IEEE Trans. Power Electronics, vol. 17, pp. 172-179, March 2002.
- [51] Y. Zhang, R. Zane and D. Maksimovic, "System Modeling and Digital Control in Modular Masterless Multi-phase DC-DC Converters," in Proc. IEEE Power Electronics Specialists Conf., 2006, pp.1-7.
- [52] Y. Zhang, R. Zane, D. Maksimovic, "Current Sharing in Digitally Controlled Masterless Multi-phase DC-DC Converters," in Proc. IEEE Power Electronics Specialists Conf., 2005, pp. 2722-2728.
- [53] S. Luo, Z. Ye, R. Lin and F.C Lee, "A Classification and Evaluation of Paralleling Methods for Power Supply Modules," in Proc. IEEE Power Electronics Specialists Conf., 1999, pp.901-908.

- [54] K. Yao, M. Xu, Y. Meng, F.C. Lee, "Design Considerations for VRM Transient Response Based on the Output Impedance," IEEE Trans. Power Electronics, vol.18, pp. 1270-1277, November 2003.
- [55] B.T. Irving and M.M. Jovanovic, "Analysis, Design, and Performance Evaluation of Droop Current-Sharing Method," in Proc. IEEE Applied Power Electronics Conf., 2000, pp.235-241.
- [56] I. Batarseh, K. Siri, H. Lee, "Investigation of the Output Droop Characteristics of Parallel-connected DC-DC Converters," in Proc. IEEE Power Electronics Specialists Conf., 1994, pp. 1342-1351.
- [57] R.B. Ridley, B.H. Cho, F.C. Lee, "Analysis and Interpretation of Loop Gains of Multiloop-Controlled Switching Regulators," IEEE Trans. Power Electronics, vol. 3, pp. 489-498, October 1988.
- [58] Z. Qian, O. Abdel-Rahman, I. Batarseh, "An Integrated Four-Port DC/DC Converter for Renewable Energy Applications," accepted by IEEE Transactions on Power Electronics.
- [59] Z. Qian, O. Abdel-Rahman, H. Al-Atrash, I. Batarseh, "Modeling and Control of Three-Port DC/DC Converter Interface for Satellite Applications," accepted by IEEE Transactions on Power Electronics.
- [60] Z. Qian, O. Abdel-Rahman, H. Hu, I. Batarseh, "Multi-channel Three-port DC/DC Converters as Maximal Power Tracker, Battery Charger and Bus Regulator," in Proc. IEEE Applied Power Electronics Conference, 2010, pp. 2073-2079 .